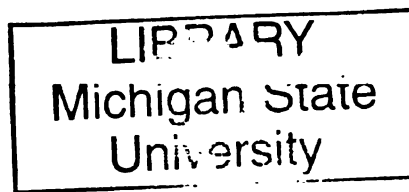




2  
2009



This is to certify that the  
dissertation entitled

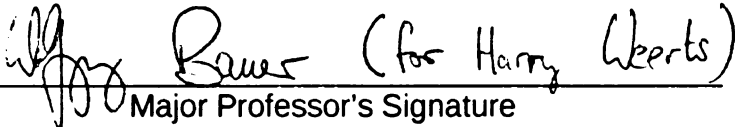
MEASUREMENTS OF THE WZ DI-BOSON  
PRODUCTION CROSS SECTION AT  $\sqrt{s} = 1.96$  TeV  
IN THE DIELECTRON AND DIMUON CHANNELS

presented by

Rahmi ÜNALAN

has been accepted towards fulfillment  
of the requirements for the

Ph.D. degree in Physics

  
Major Professor's Signature

June 15, 2009  
Date



**PLACE IN RETURN BOX** to remove this checkout from your record.  
**TO AVOID FINES** return on or before date due.  
**MAY BE RECALLED** with earlier due date if requested.

DATE DUE	DATE DUE	DATE DUE

MEASUREMENTS OF THE WZ DI-BOSON PRODUCTION CROSS  
SECTION AT  $\sqrt{s} = 1.96$  TeV IN THE DIELECTRON AND DIMUON  
CHANNELS

By

Rahmi Ünal

A DISSERTATION

Submitted to  
Michigan State University  
in partial fulfillment of the requirements  
for the degree of

DOCTOR OF PHILOSOPHY

Physics

2009

## ABSTRACT

# MEASUREMENTS OF THE WZ/ZZ DI-BOSON PRODUCTION CROSS SECTION AT $\sqrt{s} = 1.96$ TeV IN THE DIELECTRON AND DIMUON CHANNELS

By

Rahmi Ünal

The cross section measurements of WZ and ZZ di-boson productions using proton-antiproton collisions at  $\sqrt{s} = 1.96$  TeV using the data collected with the DØ detector at Fermilab is presented. Both the  $ee + jets$  and  $\mu\mu + jets$  final states are considered. with total luminosities  $1044 \text{ pb}^{-1}$  and  $948 \text{ pb}^{-1}$  respectively in each channel. Both of the leptons are decay products of a Z boson. This study uses a different approach to simple likelihood method. The measured cross sections for the two processes are :

$$\sigma_{WZ/ZZ \rightarrow eejj} = 2.67 \pm 1.90 \text{ pb}$$

and

$$\sigma_{WZ/ZZ \rightarrow \mu\mu jj} = 3.45 \pm 3.51 \text{ pb}$$

*To my parents*  
*Nurcan and Nafiz ÜNALAN*  
*with all my gratitude ...*

## ACKNOWLEDGEMENTS

Even a small size project usually is accomplished better with several people working on different aspects of it. This work is no exception with all the weaknesses and short comings which are all due to myself. There are a lot of people who helped me reach this point. I cannot possibly name all of them lest there won't be any space for the actual work.

However I'd like to share with the reader some of the names who deserves at least a hint.

First and foremost my respects and gratitudes go to my parents, Nurcan and Nafiz Ünalán, who never doubted me and always encouraged me not only in this work but everything in my life, and for my life in general. I'd like to thank to my wife Zeynep whose help was mostly behind the curtains. I appreciated my son Tarık's effort to keep me on track.

Reaching to the safest shore never easy and requires one to place one's faith in one's guide. I thank to my adviser Harry Weerts for being so patient with me.

People in MSU experimental high energy group were extremely helpful, I'd like to acknowledge especially Reiner Hauser, and James Kraus for their help whenever I needed.

I wish to express my thanks to DiBoson Group, whose comments were very helpful to shape this work and everyone in DØ without them, this work and others could not exist.

I think, this work would be useless and a wasted effort if there were no one to read and think about it. Thus I thank the reader for honoring this work and me by reading it.

Finally ...



# TABLE OF CONTENTS

<b>LIST OF TABLES</b>	<b>vi</b>
<b>LIST OF FIGURES</b>	<b>viii</b>
<b>Introduction</b>	<b>1</b>
<b>1 Theory</b>	<b>4</b>
1.1 Standard Model . . . . .	4
1.1.1 Particles, Short History . . . . .	4
1.1.2 Standard Model . . . . .	6
1.2 Di-Boson Physics . . . . .	16
1.2.1 Electroweak Theory . . . . .	16
1.2.2 Di-Boson Interactions . . . . .	17
<b>2 Experimental Apparatus</b>	<b>22</b>
2.1 Fermilab . . . . .	22
2.2 Particle Accelerators . . . . .	24
2.2.1 Proton Source . . . . .	26
2.2.2 Anti-proton Source . . . . .	29
2.2.3 Main Injector . . . . .	30
2.2.4 Tevatron . . . . .	31
2.2.5 Recycler . . . . .	35
2.3 DØ Detector . . . . .	35
2.3.1 DØ Coordinate System . . . . .	37
2.3.2 DØ Luminosity Monitor . . . . .	40
2.3.3 DØ Tracking Detectors . . . . .	41
2.3.4 DØ Pre-shower Detectors . . . . .	45
2.3.5 DØ Calorimeter . . . . .	47
2.3.6 DØ Muon Detectors . . . . .	53
2.3.7 DØ Trigger System . . . . .	54
<b>3 Event Reconstruction and Object Identification</b>	<b>61</b>
3.1 Introduction . . . . .	61
3.2 Tracks . . . . .	62
3.3 Primary Vertex . . . . .	63
3.4 Electromagnetic Objects . . . . .	64

3.5	Hadronic Objects, Jets . . . . .	67
3.6	Missing Transverse Energy, MET . . . . .	70
3.7	Muons . . . . .	70
<b>4</b>	<b>Data Samples</b>	<b>74</b>
4.1	Data Set . . . . .	74
4.2	Data Quality . . . . .	76
4.3	Monte Carlo . . . . .	78
<b>5</b>	<b>Cross Section Measurement</b>	<b>79</b>
5.1	Introduction . . . . .	79
5.2	Objects Identification . . . . .	80
5.2.1	Lepton Identification: Electrons . . . . .	80
5.2.2	Lepton Identification: Muons . . . . .	81
5.2.3	Jet Identification . . . . .	83
5.2.4	Missing Transverse Energy, MET . . . . .	86
5.2.5	Other Objects Identifications . . . . .	87
5.2.6	Constructing the Vector Boson: Z Boson . . . . .	88
5.2.7	Object Identification Efficiencies . . . . .	91
5.2.8	Trigger Efficiency . . . . .	93
5.3	Backgrounds . . . . .	94
5.3.1	<i>jet</i> Backgrounds . . . . .	95
5.3.2	<i>top-antitop</i> Backgrounds . . . . .	98
5.3.3	<i>Z + jets</i> Backgrounds . . . . .	101
5.4	Corrections . . . . .	103
5.5	Technique . . . . .	107
5.5.1	WZ and ZZ Event Selection . . . . .	107
5.5.2	Likelihood Method . . . . .	114
<b>6</b>	<b>Results</b>	<b>165</b>
6.1	Likelihood Results . . . . .	165
6.1.1	Systematic Errors . . . . .	171
6.2	Conclusion . . . . .	172
	<b>Bibliography</b>	<b>173</b>

# LIST OF TABLES

1.1	Three families of leptons, their masses and electric charges. Anti-particles of these have the same properties except the charge which should be negated. All of these particles have spins 1/2. . . . .	8
1.2	Three families of quarks, their masses and electric charges. Anti-particles of these have the same properties except the charge which should be negated. Besides electric charge quarks carry another type of charge: Color. There can only be three states of color charge which are red, blue and green. Previous rule (negation) applies on color charge too if one wants to get anti-particle counter-part of a quark. For explanation of the color see the tex. All of these particle have spins 1/2. . . . .	9
1.3	Four forces, their masses and electric charges of their carrier particles. All of these particles are observed except graviton. Anti-particles of these have the same properties except the charge which should be negated. However since gluon carries another charge, color, its antiparticle is not itself as in $\gamma$ or $Z$ but its anti-colored gluon. All of these particle have spins 1 except graviton which should have spin 2. . . . .	11
4.1	The integrated luminosity of the RunIIa period is shown in this table for the 2EMHighPt data sample. The run ranges include test runs also but those runs are not included in the luminosity calculation as well as those runs that are excluded due to bad data quality tags. An uncertainty of 6.5% is associated to the luminosity result, because of the way luminosities are measured at DØ. . . . .	77
4.2	The integrated luminosity of the RunIIa period is shown in this table for the 2MUhighpt data sample. The run ranges include test runs also but those runs are not included in the luminosity calculation as well as those runs that are excluded due to bad data quality tags. An uncertainty of 6.5% is associated to the luminosity result, because of the way luminosities are measured at DØ. . . . .	77
5.1	The division of regions with respect to the distance between the two highest $pT$ jets in the events. . . . .	113
5.2	The di-jet mass cut is kept constant over the regions. . . . .	113
5.3	$\eta_{jet1} * \eta_{jet2}$ cuts are shown in different regions of $\Delta R$ for both electrons and muons . . . . .	113

5.4	$p_T^{j1}$ vs $p_T^{j2}$ cuts are shown in different regions of $\Delta R$ for both electrons and muons. The numbers given here are the intersection points of a line with $p_T^{j1}$ and $p_T^{j2}$ plane. . . . .	114
5.5	The names of the variables are given in their region . . . . .	123
5.6	The names of the variables are given in their region . . . . .	124
6.1	Number of estimated events in the RunIIa data using the MC discriminant distributions as templates. . . . .	169
6.2	Table of luminosity values for RunIIa run period. . . . .	170
6.3	Table of overall efficiencies for WZ/ZZ event selection. . . . .	170
6.4	Table of measured cross sections for electron and muon channels for both WZ and ZZ processes. The measurement uses almost $1\text{ fb}^{-1}$ of data collected by DØdetector in both channels. . . . .	171
6.5	Table showing the systematic uncertainties of the different sources. . .	171

# LIST OF FIGURES

1.1	The elementary particles that are predicted by the SM. The left most column shows the observed gauge bosons carriers of three forces out of four observed in the Nature. There are eight different type of gluons ( $g$ ) carrying color-anticolor charge. $\gamma$ and $Z$ have anti-particles identical with themselves, $W^+$ is anti-particle of $W^-$ and anti-particles of the gluons are elements of the same set. Quarks carry electroweak and color charges. Next two columns show isospin doublets. Three different color charges are shown in the same area to emphasize that actually there are three different quarks. $u, c, t$ quarks have $+2/3$ fractional charge, $d, s, b$ quarks have $-1/3$ fractional charge. The unobserved and most sought after Higgs boson is shown in the right most column. . . . .	15
1.2	The leading order Feynman diagrams for $WZ$ process. The left one on top is for t-channel process, and the right one on top is for u-channel process. The bottom picture shows s-channel process. The decay products reflect that this analysis is interested in only: two leptons and two jets final states. . . . .	19
1.3	The leading order Feynman diagrams for $ZZ$ process. The left one for t-channel process, and the one on the right is for u-channel process. The decay products reflect that this analysis covers only two leptons and two jets final states. . . . .	21
2.1	An aerial view of Fermilab facility at village of Weston, 40 miles west of Chicago, IL. Tunnels of Main Injector, Tevatron and fixed target experiments can be seen. In the photo, one could see the north-east side of the Fermilab in the distance. . . . .	23
2.2	A schematic diagram of Fermilab's accelerator complex is shown in the figure. Drawings are smoothed at some points. The drawing is not scaled. . . . .	25
2.3	A detailed schematic diagram of Pre Accelerator. On the left side a part of the high voltage dome is shown. $H^-$ ions leaves from the pre-accelerator from the right side with an energy of 750 keV. . . .	26
2.4	A picture of Fermilab's Linac. On the left is shown the drift tube Linac whereas on the right is shown the high energy part of the Linac. Both of the components make up the Linac. $H^-$ ions enters the Linac at the drift tube side of the Linac. . . . .	27
2.5	A schematic diagram of Fermilab's Booster. All the major components are shown as well as the locations of the RF cavities. . . . .	28



2.6	A schematic diagram of Fermilab's nickel target for anti-proton production. It consists of alternating disks of target (Ni) and cooling disks (Al). The target is rotated after a period of usage in order to preserve the targets shape. . . . .	30
2.7	A schematic diagram of Fermilab's Debuncher and Accumulator. Protons with 120 GeV energy are hit on the target producing $\bar{p}$ s. They are collected via a lithium lens and sent to Debuncher. Then they are transferred to accumulator (smaller triangular ring). Being a small ring, accumulator cannot store all the $\bar{p}$ s, therefore $\bar{p}$ are sent to Recycler via transfer lines. . . . .	31
2.8	A schematic diagram of Fermilab's Main Injector, and its connections to its adjacent accelerator facilities. It is used for storing protons for further usage such as $\bar{p}$ creation, neutrino creation, proton studies, Tevatron stores and the like. . . . .	32
2.9	A schematic diagram of Fermilab's Tevatron showing the relative locations of the beams inside it. There are three "trains" of twelve bunches. The bunch to bunch spacing is 396 ns = 21 RF buckets. The abort gap between the trains of 2.617 $\mu$ sec buckets. Different bunches in a train encounter the opposing beam at different places around the ring. . . . .	34
2.10	The schematic view of the cross section of the DØ detector. The figure is scaled. The beam pipe carrying proton anti-proton beams passes through the center of the detector. The direction of the proton beam is assigned to positive z direction. From the center of the detector in radial direction the following detectors are located: Central Tracker (Silicon Microstrip Tracker, Central Fiber Tracker, Solenoid), Preshowers, Calorimeters Inter Cryostat Detectors, Luminosity Detectors, Muon Detectors. . . . .	36
2.11	The orientation of right handed coordinate system of the DØ detector. The direction of the movement of proton beam is accepted as positive z-direction; negative z-direction is assigned to the direction of anti-proton beam. y-axis is chosen skywards and x-axis points in the opposite direction of the center of the Tevatron ring. . . . .	38

2.12	The schematics of the DØ detector's tracking system. Silicon Microstrip Tracker (SMT) is surrounded by Central Fiber Tracker (CFT). During the RunII upgrade phase, another tracking detector is placed in the region between the beam pipe and SMT, layer-0 detector, which has increased the resolution of the beam spot and the tracks. The coverage of the tracker is up to $\eta_D = 2$ . Since the central tracking system sits inside a 2 T magnetic field providing solenoid magnet, it is possible to measure the momentum of the particles from the curvature of the tracks. . . . .	42
2.13	A nice picture showing the DØ detector's silicon micro-strip tracking system (SMT). It has six barrel shaped detector components laid in the direction of beam pipe. The barrels have four layers. 8 disks are dispersed between the six barrels and another four are further away from the center. The disks are placed perpendicular to the beam pipe.	43
2.14	The picture showing the cross sectional view of the DØ detector's silicon micro-strip tracking system (SMT). The SMT barrels and their support structure are shown. Four double sided layers are placed consecutively. . . . .	44
2.15	The picture showing the DØ detector's central fiber tracker system (CFT). Eight layers of scintillating fibers are used to get an accurate measurement of momentum measurement of the charged particles passing through the CFT. The solenoid is placed between CPS layer and the eighth layer of CFT, but is not shown in this figure. . . . .	45
2.16	Figure showing the forward preshower detector system (CFT). These detectors is placed between the central calorimeter and the end-cap calorimeters. . . . .	46
2.17	The figure showing the DØ detector's central pre-shower detector and forward pre-shower detector geometry. The geometry shows a little difference between the two detector systems, but in both of the detectors triangular scintillating fibers with a waveguide in the center are used to transfer light wave for position measurement. . . . .	47
2.18	The DØ calorimeter. The regions shown yellow and dark blue are built by depleted uranium to contain showers of the particles in a small volume. The rest is built with steel and copper. The calorimeter is cryogenic . The region between the layers of metals is filled with liquid argon as active media. The calorimeter has three parts: North End-cap Calorimeter, Central Calorimeter and South End-cap Calorimeter. The cylindrical hollow region in the center houses the tracking system of the DØ detector. . . . .	48

2.19	A nice picture showing the unit of the calorimeter cell of the DØ detector. The thickness of the uranium absorbing plates differs depending on which layer it is located. Between the plates resides the liquid argon as the active ionizing medium. . . . .	50
2.20	The cross sectional view of calorimeter quadrant. In this picture the calorimeter towers are shown as differing colors centered at the center of the calorimeter. For trigger system two of these towers are combined together and an approximate energy measurement is done for fast response times. . . . .	52
2.21	The schematics of the calorimeter readout chain. Every cell can be thought of as being a big capacitance charged according to the energy of the incoming particles. At the end of this chain the energies of the particles are digitized. . . . .	53
2.22	The schematic picture of the muon drift chambers are shown in all the layers. Due to the presence of the detector support, the bottom side of the detector coverage is partial. . . . .	55
2.23	The schematic picture of the muon scintillators are shown in all the layers. Due to the presence of the detector support, the bottom side of the detector coverage is partial. . . . .	56
2.24	The data flow diagram of the Level-1 and Level-2 trigger systems. SMT is not used in the first level because of the time constraint on this system. Trigger framework is the decision maker and the messenger between the different detector components and read-out crates. . . .	58
3.1	The figure showing the development of the jets in the calorimeter, hence the procedure to follow to reconstruct jets based on the information collected by the calorimeter. . . . .	68
3.2	Figure showing the calculation of the momentum of the muon locally by the muon detector. The toroid affects the path of the muon passing through it by deflecting it by certain angle which depends on the charge and the momentum of the muon. The magnetic field in the toroid is a known parameter of the calculation. . . . .	72
3.3	Figure showing construction of a muon track segment in drift tubes. The drift wires are perpendicular to the plane defined by the paper. Blue line is the constructed muon path according to the drift circles which are shown in red. . . . .	73
5.1	Di-electron mass distribution for the RunIIa Data set after preselection. All the events contributing to this histogram have two good quality electrons with $p_T > 15$ GeV and one good quality jet with $p_T > 20$ GeV . . . . .	89

5.2	Di-muon mass distribution for RunIIa Data set after preselection. All the events contributing to this histogram have two good quality muons with $p_T > 15$ GeV and one good quality jet with $p_T > 20$ GeV . . . . .	90
5.3	Figure show a typical trigger turn on curve. This is produced by using the CEM(1,11) trigger. It requires an electron with a transverse momentum of 11 GeV in the event. As it is seen from the figure selecting with this trigger is not quite efficient unless the object has at least 20 GeV transverse momentum. . . . .	94
5.4	The figure shows (a) the Z mass distribution for the QCD events and the fit before the application of cuts; (b) same distribution after the cuts; the number of expected events in different bins before normalization for (c) electron and (d) muon channels. . . . .	97
5.5	The figure shows MET distributions for the electron (left column) and the muon (right column) channels for Monte Carlo events. The effect of MET cut can be seen on the second row. . . . .	99
5.6	The figure shows di-lepton mass distributions for the electron (left column) and the muon (right column) channels for $t\bar{t}$ events. In the same panel is shown before (in black) and after (in blue) the missing transverse energy cuts. While the first row shows whole mass range, the second row shows only Z mass window region. . . . .	100
5.7	The di-jet mass distributions for signal (left hand side) and background (right hand side) Monte Carlo events for electron (first raw) and muon (second raw) channels. To preserve the relative strengths of the distributions, they are not normalized one. . . . .	102
5.8	The figure shows the discrepancy between the Monte Carlo events and data for $\eta_{j1}$ , $\eta_{j2}$ and $\Delta R_{j1,j2}$ distributions (from top to bottom). On the left is shown the electron channel, and on the right is shown the muon channel. Since our result will heavily depend on these distribution, a correction factor is assigned as a weight to every event.104	
5.9	The figure shows the fits that are used for correcting event weights of the Monte Carlo events for $\eta_{j1}$ , $\eta_{j2}$ and $\Delta R_{j1,j2}$ distributions (from top to bottom). Since our result will heavily depend on these distribution, a correction factor is assigned as a weight to every event. Left column is for electron channel and right column is for muon channel. . . . .	105
5.10	The figure shows distributions of $\eta_{j1}$ , $\eta_{j2}$ and $\Delta R_{j1,j2}$ (from top to bottom) after corrections are applied. Left column is for electron channel and right column is for muon channel. . . . .	106

5.11	The di-jet mass distributions for signal (left hand side) and background (right hand side) Monte Carlo events for electron (first row) and muon (second row) channels. To preserve the relative strengths of the distributions, they are not normalized one. . . . .	110
5.12	The distributions for $\eta_{jet1} \times \eta_{jet2}$ . The one on the left is obtained by using only the signal Monte Carlo events. The one on the right side is for the background Monte Carlo events. There is an obvious skewness towards right in the signal distribution, which is expected. . . . .	111
5.13	The distributions for $p_T^{j1}$ vs $p_T^{j2}$ . The left column is for electron channel and the right column is for muon channel. The lines show a probable cut on these two variable together. It is obvious from the plots that background events are mostly below the line. . . . .	112
5.14	An example distributions showing the color codes used in this thesis. . . . .	118
5.15	The distributions for di-jet mass for electron channel in first and second regions for likelihood discriminant input. . . . .	125
5.16	The distributions for di-jet mass for electron channel in third and fourth regions for likelihood discriminant input. . . . .	126
5.17	The distributions for di-jet mass for muon channel in first and second regions for likelihood discriminant input. . . . .	127
5.18	The distributions for di-jet mass for muon channel in third and fourth regions for likelihood discriminant input. . . . .	128
5.19	The distributions for leading jet $p_T$ for electron channel in first and second regions. . . . .	129
5.20	The distributions for leading jet $p_T$ for electron channel in third and fourth regions. . . . .	130
5.21	The distributions for leading jet $p_T$ for muon channel in first and second regions. . . . .	131
5.22	The distributions for leading jet $p_T$ for muon channel in third and fourth regions. . . . .	132
5.23	The distributions for second jet $p_T$ for electron channel in first and second regions. . . . .	133
5.24	The distributions for second jet $p_T$ for electron channel in third and fourth regions. . . . .	134
5.25	The distributions for second jet $p_T$ for muon channel in first and second regions. . . . .	135



5.26	The distributions for second jet $p_T$ for muon channel in third and fourth regions. . . . .	136
5.27	The distributions for Z rapidity in the center of mass frame of W/Z (di-jet) and Z (di-lepton) frame for electron channel in first and second regions. . . . .	137
5.28	The distributions for Z rapidity in the center of mass frame of W/Z (di-jet) and Z (di-lepton) frame for electron channel in third and fourth regions. . . . .	138
5.29	The distributions for Z rapidity in the center of mass frame of W/Z (di-jet) and Z (di-lepton) frame for muon channel in first and second regions. . . . .	139
5.30	The distributions for Z rapidity in the center of mass frame of W/Z (di-jet) and Z (di-lepton) frame for muon channel in third and fourth regions. . . . .	140
5.31	The distributions of the angle between reconstructed Z object and the center of mass frame of W/Z (di-jet) and Z (di-lepton) objects for electron channel in the first and second regions. . . . .	141
5.32	The distributions of the angle between reconstructed Z object and the center of mass frame of W/Z (di-jet) and Z (di-lepton) objects for electron channel in the third and fourth regions. . . . .	142
5.33	The distributions of the angle between reconstructed Z object and the center of mass frame of W/Z (di-jet) and Z (di-lepton) objects for muon channel in the first and second regions. . . . .	143
5.34	The distributions of the angle between reconstructed Z object and the center of mass frame of W/Z (di-jet) and Z (di-lepton) objects for muon channel in the third and fourth regions. . . . .	144
5.35	The distributions for $p_T$ difference of W/Z (di-jet) and Z (di-lepton) for electron channel in first and second regions. . . . .	145
5.36	The distributions for $p_T$ difference of W/Z (di-jet) and Z (di-lepton) for electron channel in third and fourth regions. . . . .	146
5.37	The distributions for $p_T$ difference of W/Z (di-jet) and Z (di-lepton) for muon channel in first and second regions. . . . .	147
5.38	The distributions for $p_T$ difference of W/Z (di-jet) and Z (di-lepton) for muon channel in third and fourth regions. . . . .	148
5.39	The distributions for di-jet $p_T$ for electron channel in first and second regions of likelihood. . . . .	149



5.40	The distributions for di-jet $p_T$ for electron channel in third and fourth regions of likelihood. . . . .	150
5.41	The distributions for di-jet $p_T$ for muon channel in first and second regions of likelihood. . . . .	151
5.42	The distributions for di-jet $p_T$ for muon channel in third and fourth regions of likelihood. . . . .	152
5.43	The distributions for the $p_T$ of the center of mass system for di-jet and di-lepton objects for electron channel in first and second regions. . .	153
5.44	The distributions for the $p_T$ of the center of mass system for di-jet and di-lepton objects for electron channel in third and fourth regions. . .	154
5.45	The distributions for the $p_T$ of the center of mass system for di-jet and di-lepton objects for muon channel in first and second regions. . .	155
5.46	The distributions for the $p_T$ of the center of mass system for di-jet and di-lepton objects for muon channel in third and fourth regions. . .	156
5.47	The distributions for the cosine of the angle between highest $p_T$ jet and second highest $p_T$ jet for electron channel in first and second regions. .	157
5.48	The distributions for the cosine of the angle between highest $p_T$ jet and second highest $p_T$ jet for electron channel in first and second regions. .	158
5.49	The distributions for the cosine of the angle between highest $p_T$ jet and second highest $p_T$ jet for muon channel in first and second regions. .	159
5.50	The distributions for the cosine of the angle between highest $p_T$ jet and second highest $p_T$ jet for muon channel in third and fourth regions. .	160
5.51	The distributions for the cosine of the angle between the highest $p_T$ jet and the Z (di-lepton) object for electron in first and second regions. .	161
5.52	The distributions for the cosine of the angle between the highest $p_T$ jet and the Z (di-lepton) object for electron in third and fourth regions. .	162
5.53	The distributions for the cosine of the angle between the highest $p_T$ jet and the Z (di-lepton) object for muon in first and second regions. .	163
5.54	The distributions for the cosine of the angle between the highest $p_T$ jet and the Z (di-lepton) object for muon in third and fourth regions. .	164

6.1	The distributions of likelihood discriminant for em channel. The left hand side shows signal and background Monte Carlo events discriminant distribution. These distributions are normalized to 1, so that their shape could be seen easily. The right hand side shows the discriminant for RunIIa events passing all the cuts previously mentioned. Total number of RunIIa data shown in this figure (right hand side) is 475 events. . . . .	166
6.2	The distributions of likelihood discriminant for muon channel. The left hand side shows signal and background Monte Carlo events discriminant distribution. These distributions are normalized to 1, so that their shape could be seen easily. The right hand side shows the discriminant for RunIIa events passing all the cuts previously mentioned. Total number of RunIIa data shown in this figure (left hand side) is 381 events. . . . .	167
6.3	Likelihood discriminants and their fits to data for electron channel. The points are for RunIIa data, the fit result is overlayed on them represents data as signal (red) and background (blue) contributions.	168
6.4	Likelihood discriminants and their fits to data for muon channel. The points are for RunIIa data, the fit result is overlayed on them represents data as signal (red) and background (blue) contributions. .	169

**Images in this thesis/dissertation are presented in color**

# Introduction

*"...I had this feeling that I'd never  
get to the other side of the street."*[1]  
J.D. Salinger

"What is it?" asked the boy. "Open and see for yourself." answered his mother. He was nervous. It could be anything, he would like or dislike. He hesitated but his curiosity overcame his hesitancy and he found himself trying to find what was beneath of all this beautiful covers.

This is our story. In front of us there lies this beautiful nature perfectly balanced, without any waste or luxury.

From the first human until now people always acknowledge their lack of knowledge and tried to know everything about themselves and their surroundings as much as they can. This is accomplished mostly inheriting knowledge from the predecessors. Last century witnessed the discovery of plenty of facts about ourselves and our environment. With them we understood that we still have innumerable things to uncover and learn.

Last century noticed blooming of atom like a rosebud. Thanks to Rutherford, Thompson and all the pioneers, we now know that not just atoms are composite objects even the bulk of their constituents are themselves composites. We learned that it is possible to break even the smallest things, and understood that their interactions between themselves are keys to answering questions such as 'why' or 'how'.



This work is also one of the many works by which the best working theory of all the littlest things, Standard Model, is tested against.

**Chapter 1** gives a basic introduction to the Standard Model (SM) and puts some emphasis on theory of diboson productions. The SM of particles is the most comprehensive (and provable by experiment) theory scientists could conjure up to today. In this chapter the motivations for di-boson cross section measurements are also is discussed.

**Chapter 2** portrays the experimental apparatus used to collect data, explicitly the DØ detector and the Tevatron  $p\bar{p}$  collider located at the Fermi National Laboratory (FermiLab). The DØ detector was built during the 1980s as a hermetic high energy particle physics detector in order to measure very precisely particle energies and momenta. It has gone through three extensive upgrades, the last being in 2006. The accelerator complex and the Tevatron is used to accelerate protons and anti-protons to 980 GeV energies. During this writing the Tevatron is the highest energy machine in the world.

**Chapter 3** explains the data collection and reconstruction procedures and how physics objects are identified. The collected data in its raw format is not very user friendly and lacks many corrections. The procedures for building useful physics objects for analysis out of energy bits are explained.

**Chapter 4** In this chapter data samples used in the analysis are explained and the total number of events are given in terms of integrated luminosity.

**Chapter 5** is the first place to look at for those who have very limited time. It presents a measurement of diboson cross section measurement in the  $WZ(ZZ) \rightarrow jets + leptons$  channel. Definitions of objects used in this analysis, selection criteria specific to this analysis, efficiencies of the objects and methods are explained. Both the electron channel and the muon channel are mentioned in this chapter.

**Chapter 6** is the summary of the results of the analyses.

# Chapter 1

## Theory

*“Yâni, zerre kimin ise, gezdiği bütün yerler de onundur.”<sup>1</sup>[2]*  
Bedüzzaman Said Nursî

The first part of this chapter presents a very short overview of particle physics and the Standard Model. The second part focuses on di-boson physics. This chapter should provide the reader with a basic understanding for the rest of the work.

### 1.1 Standard Model

#### 1.1.1 Particles, Short History

For a long time, it was known to humans that by bombarding it is possible to get past closed doors, but it is fairly new to use this technique for opening the door of the unknown behind the matter. In a sense, this is the technique widely used in Particle accelerators in order to see what’s beyond the veil.

Discoveries of several particles at the very end of 19<sup>th</sup> century caused a lot of enthusiasm among physicists. X-rays,  $\beta$  and  $\alpha$  radiations are among the very first of those. Before a new century’s helix started curling up; we knew that “the

---

<sup>1</sup>That is to say, whoever owns a particle must also own all the places it enters.

carriers of negative electricity are bodies having a mass very much smaller than that of the atom of any known element"[3] which are now called electrons instead of "corpuscles"[3].

The electron's discovery had led to a description of the atom<sup>2</sup> which was proved to be wrong by shooting  $\alpha$  particles ( $\text{He}^{+2}$  ions) at a thin foil of gold. Nowadays even in elementary schools the atom's structure is taught as resembling to the solar system. The disturbance of this metaphor in the physics community was calmed "in 1913 by the rules of quantization with help from the quantum theory(1900)"[4]. The photoelectric effect, wave nature of the electron and the concept that "only certain preferred motions, *quantized* motions, are possible or at least stable, since the energy can only assume values forming a discontinuous sequence"[5] forced physicist to adopt a new way of thinking about the matter and the first half of 20<sup>th</sup> century witnessed the birth of quantum mechanics. The knowledge about the atom, especially the hydrogen atom, was greatly increased with this new method.

While theorists were taking big steps in understanding how nature works, experimentalists were setting the spring of discoveries for the second half of the century. Although new particles were discovered occasionally until the mid century there were no signs of new particles that were proposed to explain some weird phenomena like the continuous energy distribution of electron as a result of  $\beta$  decay<sup>3</sup> and the like.

The second half of the century saw an explosion in the number of particles discovered. Most of the earlier questions were answered but the excitement caused by the new particles soon left its place to a little uneasiness. At earlier times those particles were thought to be fundamental, however, their numbers were defying that conception. Thus began a search for a new way of combining the properties

---

<sup>2</sup>This description stated that atoms are made of positive bodies with negative charges embedded in them

<sup>3</sup> Energy was not conserved by the visible particles, electrons energy spectrum was continuous as opposed to being quantized if there were two decay products in the process.

of these particles, which eventually resulted in the standard model of particle physics.

### 1.1.2 Standard Model

The abundance of observed new particles led physicists to the idea that there might be structures to the newly discovered particles. Building symmetric groups by newly found particles according to their properties, then, led to the idea of forming symmetry groups using point like constituents of those new particles (quarks), leptons and the go-between (bosons).

It is hard to explain the Standard Model (SM) thoroughly here since “it represents an enormous body of knowledge of nature that can be seen as the culmination of 400 years of physics” [6]. Although an essence of it will be given here, for rigorous treatments and explanations of SM the reader should refer to textbooks written on the subject like [7, 8, 9, 10].

The SM is about the elementary particles that can be observed in nature and the interactions between them. The term elementary in this context means that this type of particles are not composite objects, they are created and destroyed as a whole.

In reality there are quite a few elementary particles known today. It is necessary to group them so that the laws with which they are bound should emerge. The grouping is done according to their one fundamental property namely their spins<sup>4</sup>. One refers to a point like object when one speaks about elementary particles. That is why it is not very meaningful to see the spin of a particle as a spin of a spinning top, but as an internal property that affects its behavior towards other particle and forces, much like a *will* in humans. Yet this doesn't prevent physicists to use spin in a classical sense where it is appropriate. For example depending on how

---

<sup>4</sup>Spin is a vectoral quantity and usually expressed by  $\vec{s}$

you look at a particle, it may be right-handed ( $\vec{s} \cdot \vec{p} > 0$ ) or left-handed ( $\vec{s} \cdot \vec{p} < 0$ ); where  $\vec{s}$  and  $\vec{p}$  are spin vector and momentum vector respectively. This is an important discrimination, because if a particle is massless then it is possible to talk about a definite spin state<sup>5</sup>. Spin is a directional quantity, however, the classification is done according to the magnitude of the particle's spin. For all of the observed particles then, the classification<sup>6</sup> is :

- spin  $\frac{1}{2}$

- spin 1

Spin  $\frac{1}{2}$  particles, which are also called fermions since their statistical behavior described by Fermi-Dirac statistics, obey Pauli Exclusion Principle. According to that principle one and only one fermion can occupy a given quantum state. Fermions can be divided into leptons and quarks.

Fermions can be divided into leptons and quarks with respect to the role they play in electro-weak or strong interactions. While leptons feel the electro-weak force, they have no sense of the strong force. On the other hand, quarks can be attracted via the mediator of the strong force, they cannot interact with the electro-weak force carrier bosons.

Although fermions are grouped according to their interactions, physicists group them in three families with respect to their weak-interaction counter-part. In that respect there are three generations of fermions with the difference being only their masses and all the other properties the same over families. Leptons are electron ( $e^-$ ), electron neutrino ( $\nu_e$ ); muon ( $\mu^-$ ), muon neutrino ( $\nu_\mu$ ); tau ( $\tau^-$ ), tau neutrino ( $\nu_\tau$ ); and their respective antiparticles for which negative signs should

---

<sup>5</sup>Massless particles move at the speed of light regardless of the frame of reference. Because of this a particle's direction of momentum cannot change with respect to any reference frame. This fact becomes especially more important in the case of neutrino, since Standard Model assumes that they have no mass.

<sup>6</sup>Here we did not consider a still not observed but suspected particle, *graviton*, which is conceived to have a spin of 2.

	Particle Name	Mass ( $\text{GeV}/c^2$ )	Electric Charge
$\nu_e$	electron neutrino	$< 7 \times 10^{-9}$	0
$e^-$	electron	$5.11 \times 10^{-4}$	-1
$\nu_\mu$	muon neutrino	$< 3 \times 10^{-4}$	0
$\mu^-$	muon	$1.06 \times 10^{-1}$	-1
$\nu_\tau$	tau neutrino	$< 3 \times 10^{-2}$	0
$\tau^-$	tau	1.777	-1

**Table 1.1:** Three families of leptons, their masses and electric charges. Anti-particles of these have the same properties except the charge which should be negated. All of these particles have spins 1/2.

	Particle Name	Mass (GeV/ $c^2$ )	Electric Charge
$u$	up	0.002	$+\frac{2}{3}$
$d$	down	0.005	$-\frac{1}{3}$
$c$	charm	1.25	$+\frac{2}{3}$
$s$	strange	0.095	$-\frac{1}{3}$
$t$	top	175	$+\frac{2}{3}$
$b$	bottom	5	$-\frac{1}{3}$

**Table 1.2:** Three families of quarks, their masses and electric charges. Anti-Particles of these have the same properties except the charge which should be negated. Besides electric charge quarks carry another type of charge: Color. There can only be three states of color charge which are red, blue and green. Previous rule (negation) applies on color charge too if one wants to get anti-particle counterpart of a quark. For explanation of the color see the tex. All of these particle have spins 1/2.





be read **positive**. Quarks are up ( $u^{+\frac{2}{3}}$ ), down ( $d^{-\frac{1}{3}}$ ); charm ( $c^{+\frac{2}{3}}$ ), strange ( $s^{-\frac{1}{3}}$ ); top ( $t^{+\frac{2}{3}}$ ), **bottom** ( $b^{-\frac{1}{3}}$ ); and their respective antiparticles for which all the signs for charges (**both** electrical and color) should be negated.

One **striking** feature of quarks is that their charges are fractional contrary to the common **assumption** of the first half of the 20<sup>th</sup> century which stated that *charge is integer*. **Although** there are some theories in which quarks are also composite particles **and** their constituents have integer charges, they are out of the scope of this work.

The **material** in the universe is formed by bound states of the first family of these **fermions** (namely electron, its neutrino, u and d quarks), and probably their antiparticles. In general the bound state of quarks are called hadrons. All around us, we **don't** see a fractional charge carriers, which is a natural result of another striking **feature** of quarks that they don't have unbound states. They are observed either as  $q\bar{q}$  pairs (*mesons*) or in triplets of  $q$ 's and  $\bar{q}$ 's (*baryons*).

The **inability** to observe quarks as singlets and observing particles made up of same the **spin** state and charge of quarks brought up two ideas, i) there was an other **quantum** state associated with quarks<sup>7</sup>, ii) some force was barring them from **being apart** from each other. The new "charge" was termed as *color* with its three possible **values** (red, green, blue) and the force was named *color confinement*<sup>8</sup>[6].

**Tireless** efforts of many physicists via high energy experiments produced many bound **states** of quarks, but what remained unexplained was the assembling or **disassembling** forces. What, then, is responsible for keeping the particles in atoms?

**Quantum** electro dynamics (QED) was very successful in recognizing a quantum field – **electro magnetic** field – as the force; and its quanta – photons – as the carrier of that **force**. QED was a gauge invariant theory, and by symmetry all the other

---

<sup>7</sup>**Pauli** exclusion principle prevents two quarks (fermions) having been in the same **quantum state**

<sup>8</sup>**There** can be no colored bound states or free colored particles.

	Mediator of	Mass (GeV/c <sup>2</sup> )	Electric Charge
$W^-$ , $Z$	weak nuclear force	81,90	-1,0
$g$	strong nuclear force	0	0
$\gamma$	electromagnetic force	0	0
<i>graviton</i>	gravitational force	0	0

Table 1.3: Four forces, their masses and electric charges of their carrier particles. All of these particles are observed except graviton. Anti-particles of these have the same properties except the charge which should be negated. However since gluon carries another charge, color, its antiparticle is not itself as in  $\gamma$  or  $Z$  but its anti-colored gluon. All of these particle have spins 1 except graviton which should have spin 2.

interactions between the particles were explained as gauge invariant field theories<sup>9</sup>.

The weak nuclear force is responsible for interactions like  $\beta$  decay via mediators like  $W^\pm$   $Z$ , and the strong nuclear force is responsible for holding the nucleus of the atoms via gluon, electromagnetic force is responsible for keeping electron around the atom via photon.

The definition of the three forces (electro-magnetic, weak and strong) are done in such a way that they are gauge invariant.

All the mediator particles are bosons and obey Bose-Einstein statistics, which states that there can be as many particles as possible in a single quantum state.

As it is seen from the table 1.3 the symmetry of the boson masses is not preserved for weak nuclear force carriers. The same can be seen in fermions where the observed mass difference is on the order of  $10^9$  eV. This asymmetry problem

<sup>9</sup>Gravitation is yet to be explained as a gauge invariant field.

was overcome by proposing that the symmetry which would be observed in very high energy events is broken at the energy levels of our reach in high energy experiments. As its consequence another – yet to be observed – particle (whose spin should be 0) was introduced, Higgs particle.

The Standard Model combines three of these forces (weak, strong, electromagnetic) in a single Lagrangian and explains how elementary particles are coupled to each other. “Standard Model is a quantum field theory that is based on the gauge symmetry  $SU(3)_C \times SU(2)_L \times U(1)_Y$ ” [11].  $SU(3)_C$  part of this group corresponds to strong interactions with 8 gluon mediators,  $SU(2)_L \times U(1)_Y$  corresponds to electro-weak interactions with four mediators  $\gamma$ ,  $W^\pm$  and  $Z^0$ . Although gluons don’t carry electric charge, they carry color charge which allows them to interact with both quarks and themselves alike. Gluons cannot couple to other fermions (leptons) due to lack of electric charge. Weak bosons carry electroweak charge and they can interact with themselves[11] also; upon which we’ll talk about more in the next section. The Standard Model is very succesful in its predictions up to this day. It was successfull in passing all the tests with which it was challenged. There is only one challenge which still needs to be answered: where is the Higgs particle? This thesis doesn’t answer this question.

Before ending this section we would like to write the full lagrangian of standard model and the fundamental particles it foresees. The Lagrangian:

$$\mathcal{L}_{GSW} = \mathcal{L}_0 + \mathcal{L}_{em} + \mathcal{L}_\ell + \mathcal{L}_q + \mathcal{L}_H \quad (1.1)$$

where the first term is free Lagrangian and

$$\begin{aligned} \mathcal{L}_0 = & -\frac{1}{4}(A_{\mu\nu})^2 \\ & -\frac{1}{4}(B_{\mu\nu})^2 \end{aligned}$$

$$\begin{aligned}
& + \sum_{\ell} \{ \bar{\ell} (i\gamma^{\mu} \partial_{\mu} - m_{\ell}) \ell + \bar{\nu}_{\ell} i\gamma^{\mu} \partial_{\mu} \nu_{\ell} \} \\
& + \sum_q \{ \bar{q} (i\gamma^{\mu} \partial_{\mu} - m_q) q \} \\
& + \sum_{q'} \{ \bar{q}' (i\gamma^{\mu} \partial_{\mu} - m_{q'}) q' \}
\end{aligned} \tag{1.2}$$

the **second** term is electromagnetic part of the SM Lagrangian and defined as

$$\mathcal{L}_{em} = e \{ \sum_{\ell} \bar{\ell} \gamma_{\mu} \ell - \frac{2}{3} \sum_q \bar{q} \gamma_{\mu} q + \frac{1}{3} \sum_{q'} \bar{q}' \gamma_{\mu} q' \} A^{\mu} \tag{1.3}$$

the **third** term is the weak leptonic sector of the SM Lagrangian and defined as

$$\begin{aligned}
\mathcal{L}_{\ell} = & \sum_{\ell} \{ \frac{g}{2\sqrt{2}} [\bar{\ell} \gamma_{\lambda} (1 + \gamma_5) \nu_{\ell} W^{\lambda} + h.c.] \\
& + \frac{g}{4 \cos \Theta_W} [\bar{\nu}_{\ell} \gamma_{\lambda} (1 + \gamma_5) \nu_{\ell} - \bar{\ell} \gamma_{\lambda} (C_V + \gamma_5) \ell] Z^{\lambda} \}
\end{aligned} \tag{1.4}$$

the **fourth** term is the weak quark sector of the SM Lagrangian and defined as

$$\begin{aligned}
\mathcal{L}_q = & \sum_{q, q'} \{ \frac{g}{2\sqrt{2}} [\bar{q} \gamma_{\lambda} (1 + \gamma_5) U_{qq'} q' W^{\lambda} + h.c.] \\
& + \frac{g}{4 \cos \Theta_W} [\bar{q} \gamma_{\lambda} (C'_V + \gamma_5) q - \bar{q}' \gamma_{\lambda} (C''_V + \gamma_5) \ell] Z^{\lambda} \}
\end{aligned} \tag{1.5}$$

the **last** term is Higgs sector of the the SM Lagrangian and defined as

$$\begin{aligned}
\mathcal{L}_H = & \frac{1}{2} (\partial_{\mu} H)^2 - m_H^2 H^2 - h \lambda H^3 - \frac{h}{4} H^4 \\
& + \frac{g^2}{4} (W_{\mu}^{\dagger} W^{\mu} + \frac{1}{2 \cos^2 \Theta_W} Z_{\mu} Z^{\mu}) (\lambda^2 + 2\lambda H + H^2) \\
& + \sum_{\ell, q, q'} (\frac{m_{\ell}}{\lambda} \bar{\ell} \ell + \frac{m_q}{\lambda} \bar{q} q + \frac{m_{q'}}{\lambda} \bar{q}' q') H
\end{aligned} \tag{1.6}$$

where **h.c.** stands for ‘hermitian conjugate’ and

$\ell = (e, \mu, \tau)$  (electron, muon, tau)

$q = (u, c, t)$  (up, charm, top)

$q' = (d, s, b)$  (down, strange, bottom)

$$\mathbf{A}_{\mu\nu} = \partial_\mu A_\nu - \partial_\nu A_\mu + g[A_\mu \times A_\nu]$$

$$\mathbf{B}_{\mu\nu} = \partial_\mu B_\nu - \partial_\nu B_\mu$$

$$A_1^\mu + i A_2^\mu = \sqrt{2} W^\mu$$

$$A_3^\mu = \cos \Theta_W \cdot Z^\mu - \sin \Theta_W \cdot A^\mu$$

$$B^\mu = \sin \Theta_W \cdot Z^\mu + \cos \Theta_W \cdot A^\mu$$

$\Theta_W$  is the weak mixing angle and

$W_\lambda, W_\lambda^\dagger$  = charged intermediate boson field

$A_\lambda$  = photon field

$Z_\lambda$  = neutral intermediate boson field

$$e = g \sin \Theta_W = g' \cos \Theta_W$$

$$C_V = 1 - 4 \sin^2 \Theta_W$$

$$C'_V = 1 - \frac{8}{3} \sin^2 \Theta_W$$

$$C''_V = 1 - \frac{4}{3} \sin^2 \Theta_W$$

$$\sin^2 \Theta_W = 0.23 \pm 0.01$$

$$\mathbf{U} = \begin{pmatrix} c_1 & s_1 c_3 & s_1 s_3 \\ -s_1 c_2 & c_1 c_2 c_3 + s_2 s_3 e^{i\delta} & c_1 c_2 s_3 - s_2 c_3 e^{i\delta} \\ -s_1 s_2 & c_1 s_2 c_3 - c_2 s_3 e^{i\delta} & c_1 s_2 s_3 + c_2 c_3 e^{i\delta} \end{pmatrix} \quad (1.7)$$

with  $c_i = \cos \Theta_i$  and  $s_i = \sin \Theta_i$  and  $i = 1, 2, 3$ . Particles:

See **Figure 1.1**. In the Standard Model there are 17 free parameters such as the masses of the particles. These free parameters are not predicted in the SM, but need to be measured. This is the reason behind all the experiments.

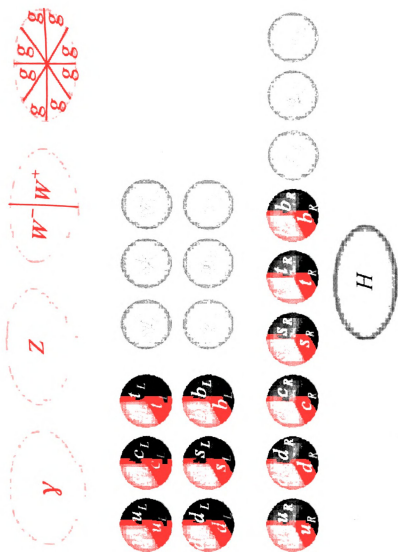


Figure 1.1: The elementary particles that are predicted by the SM. The left most column shows the observed gauge bosons carriers of three forces out of four observed in the Nature. There are eight different type of gluons ( $g$ ) carrying color-anticolor charge.  $\gamma$  and  $Z$  have anti-particles identical with themselves,  $W^+$  is anti-particle of  $W^-$  and anti-particles of the gluons are elements of the same set. Quarks carry electroweak and color charges. Next two columns show isospin doublets. Three different color charges are shown in the same area to emphasize that actually there are three different quarks.  $u, c, t$  quarks have  $+2/3$  fractional charge,  $d, s, b$  quarks have  $-1/3$  fractional charge. The unobserved and most sought after Higgs boson is shown in the right most column.

1.

1.2

1.3

1.4

1.5

1.6

1.7

1.8

1.9

1.10

1.11

1.12

1.13

1.14

1.15

1.16

1.17

1.18

1.19

1.20

1.21

1.22

1.23

1.24

1.25

1.26

1.27

1.28

1.29



## 1.2 Di-Boson Physics

### 1.2.1 Electroweak Theory

The Standard Model (SM) is based on group theory. It is part of the  $SU(3) \times SU(2)_L \times U(1)_Y$  group. The  $SU(2)_L \times U(1)_Y$  symmetry group is the part that defines gauge interactions of electroweak bosons with fermions. The gauge fields introduced by this theory are  $W_\mu^i$  (where  $i$  can take only three values) for  $SU(2)_L$  and  $B_\mu$  for  $U(1)_Y$ .

The SM requires massless neutrinos, and neutrinos only occur with one handedness, they are always in left-handed spin state, that's why electroweak interactions do not conserve parity. Conservation of parity means that the identical interaction happening for a left-handed neutrino should occur for right-handed one which do not exist [15]. Due to the fact that electroweak interactions don't conserve parity, fermions coupling via electroweak force are called left-handed fermion fields, they can be observed. But their right-handed counter-part fermion fields are never observed. The left-handed fermion fields are shown as isospin doublets

$$\begin{pmatrix} \nu_i \\ \ell_i \end{pmatrix} \quad \begin{pmatrix} q_k \\ q_{k'} \end{pmatrix} \quad (1.8)$$

where  $i = (e, \mu, \tau)$ ,  $k = (u, c, t)$  and  $k' = (d, s, b)$ ; and right handed fermion fields are shown as isospin singlets

$$\begin{pmatrix} \ell_i \end{pmatrix} \quad \begin{pmatrix} q_k \end{pmatrix} \quad (1.9)$$

where  $i = (e, \mu, \tau)$ ,  $k = (u, d, c, s, t, b)$ . The electroweak doublets transform under  $j = 1/2$  of  $SU(2)$  and singlets transform under  $j = 0$  representation of  $SU(2)$ .

As in quantum electrodynamics (QED), electroweak theory has an interaction

term of the **form** :

$$J_{WEAK}^\mu W_\mu, \quad (1.10)$$

with

$$J_{WEAK}^\mu = \psi_{aL}^- \gamma^\mu \psi_{bL} = \frac{1}{2} \bar{\psi}_a (\gamma^\mu - \gamma^\mu \gamma^5) \psi_b \quad (1.11)$$

$J_{WEAK}^\mu$  contains only left handed particles and has the vector – axial vector  $(V - A)$  **form**. Since the particles  $a$  and  $b$  can be different particles with different charge, **the** carrier of the field must carry charge too.

### 1.2.2 Di-Boson Interactions

The di-boson interactions are predicted by the Standard Model. This study is about the **simultaneous** production of massive electro-weak bosons (WW, WZ, ZZ). The **Lagrangian** describing these interactions is contained in the free lagrangian  $\mathcal{L}_i$ .

$$\begin{aligned} \mathcal{L} &= -\frac{1}{4}(A_{\mu\nu})^2 + \frac{1}{2}(\partial_\mu A_\nu - \partial_\nu A_\mu)\partial^\mu A^\nu \\ &= g[A_\nu \times A_\mu]\partial^\mu A_\nu + \frac{g^2}{4}\{(A_\mu A_\nu)(A^\nu A_\mu) - (A_\mu A^\mu)^2\} \end{aligned} \quad (1.12)$$

The **first term** in the above equation is the trilinear coupling term. The effective **Lagrangian** of the process then becomes

$$\begin{aligned} \frac{\mathcal{L}_{WWV}}{g_{WWV}} &= ig_1^V (W_{\mu\nu}^\dagger W^\mu V^\nu - W_\mu^\dagger V_\nu W^{\mu\nu}) + i\kappa_V W_\mu^\dagger W_\nu V^{\mu\nu} \\ &+ i\frac{\lambda_V}{M_W^2} W_{\lambda\mu}^\dagger W_\nu^\mu V^{\nu\lambda} - g_4^V W_\mu^\dagger W_\nu (\partial^\mu V^\nu + \partial^\nu V^\mu) \\ &+ g_5^V \epsilon^{\mu\nu\rho\alpha} (W_\mu^\dagger \overleftrightarrow{\partial}_\rho W_\nu) V_\alpha + i\tilde{\kappa}_V W_\mu^\dagger W_\nu \tilde{V}^{\mu\nu} \\ &+ i\frac{\lambda_V}{M_W^2} W_{\lambda\mu}^\dagger W_\nu^\mu \tilde{V}^{\nu\mu} \end{aligned} \quad (1.13)$$



The differential cross section for reaction

$$q_i \bar{q}_j \rightarrow W^\pm Z^0$$

and

$$q_i \bar{q}_j \rightarrow Z^0 Z^0$$

averaged over quark colors is given by [12].  $W^\pm Z^0$  expression contains four terms one for each channel ( $u, t, s$ ) and one for their interference. Depending on which part of the phase space one looks at the contributions coming from each of these diagrams change.  $s$  channel has more dependence on the available energy, thus as the center of mass energy increases its contribution decreases. However with the anomalous couplings one should expect to see an increase in the contribution to cross section from  $s$  channel.[13]  $Z^0 Z^0$  expression contains only two terms one for each channel ( $u, t$ ) since in the SM there is no  $s$  channel production mechanism for it. Both of these channels contribute equally to the total cross section of this process.

The search in this analysis is for those cases where one boson decays leptonically whereas the other decays hadronically. Due to the nature of the final particles in the process, there may be two different di-boson production mechanism: simultaneous production of  $W$  and  $Z$  bosons or simultaneous production of two  $Z$  bosons; with a  $Z$  decaying leptonically in both of the processes and the remaining boson decaying hadronically.

## $W Z$ Production

The simultaneous production of  $WZ$  bosons is described by three Feynman diagrams in the leading order as shown in the Figure 1.2. The most clean channel would be all lepton channel, and second to this is the two charged leptons and



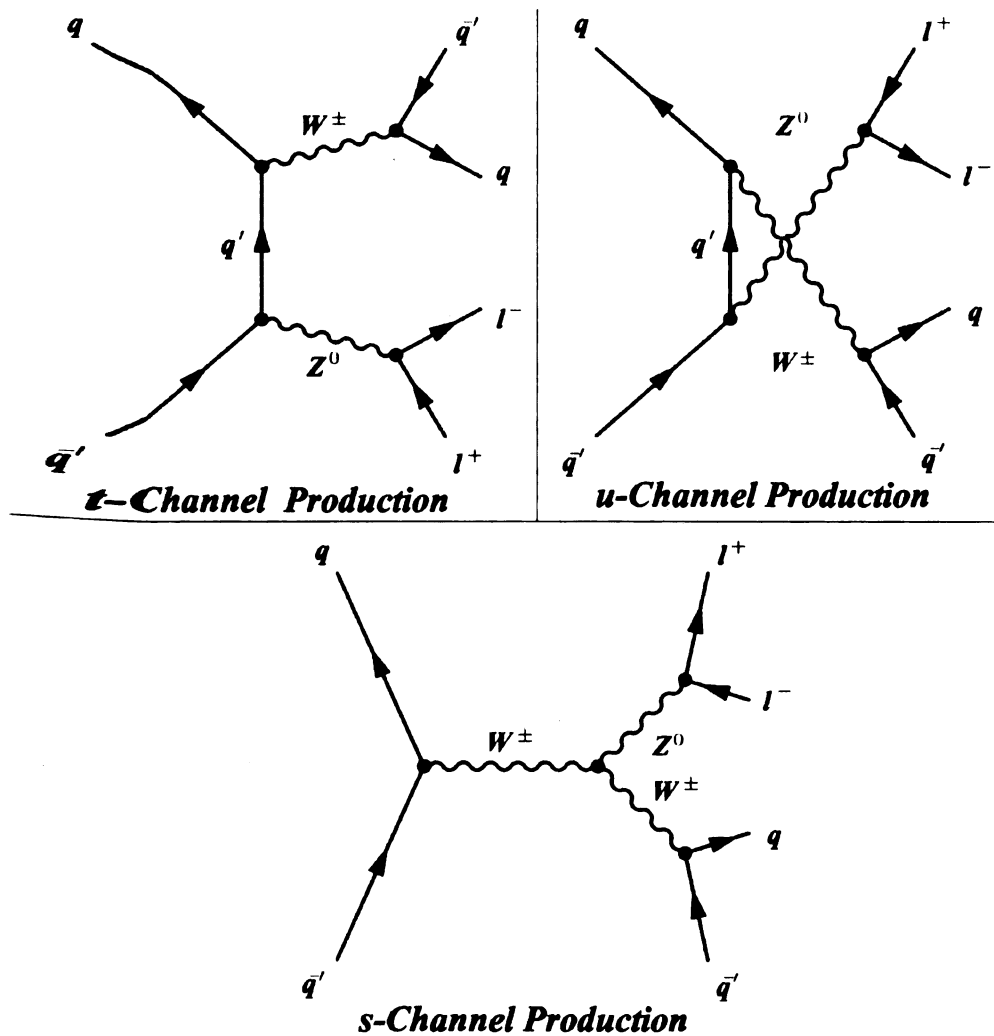


**Figure 1.2:** The leading order Feynman diagrams for  $WZ$  process. The left one on top is for  $t$ -channel process, and the right one on top is for  $u$ -channel process. The bottom picture shows  $s$ -channel process. The decay products reflect that this analysis is interested in only: two leptons and two jets final states.



two jets channel, where jets are decaying from  $W$  boson and charged leptons are decaying from  $Z$  boson. This work is devoted on this semi-leptonic decay channel where leptons are the decay products of the  $Z$  boson.

The leptons coming from the  $Z$  boson should be charged, so neutrino final states are excluded. Since  $\tau$  particles decay to lighter leptons, they are also excluded from the signal acceptance. Thus as our signal signature of the two possible final states for  $WZ$  decay are  $eejj$  and  $\mu\mu jj$ . For years it has been easy to construct a  $Z$  particle from its lepton signature due to the very cleanliness of the signature the  $Z$  leaves in the detector. But it is always hard to separate the two jets of the boson decay from jets of the remnants of the proton-proton interaction. Therefore this channel suffers most from the simultaneous production of jets along with a  $W$  or  $Z$  boson.

The theoretical production cross section for  $WZ$  production at the Tevatron is 3.68 pb[14]. To have an idea of how small the probability of producing  $WZ$  events, the reader should refer to the production cross section of  $t\bar{t}$  (the heaviest two particles known) events which is around 7 pb, doubling the rate of di-boson events. Including the detector effects such as the phase space coverage deficiencies, detection inefficiencies and the like, one could expect to see around 50 events in both electron and muon channels separately, for the whole RunIIa data taking period.

## $ZZ$ Production

The simultaneous production of  $ZZ$ s is somewhat different than simultaneous production of  $WZ$ . Although there may be an interaction vertex of  $WW(Z/\gamma)$  (trilinear) or  $WW(Z/\gamma)(Z/\gamma)$  (quartic), the SM does not allow for the same vertices for  $Z$  pairs, namely there is no trilinear  $ZZ(Z/\gamma)$  or quartic  $ZZ(Z/\gamma)(Z/\gamma)$  couplings.

Because of this the  $ZZ$  interaction cannot be described by s-channel interactions.



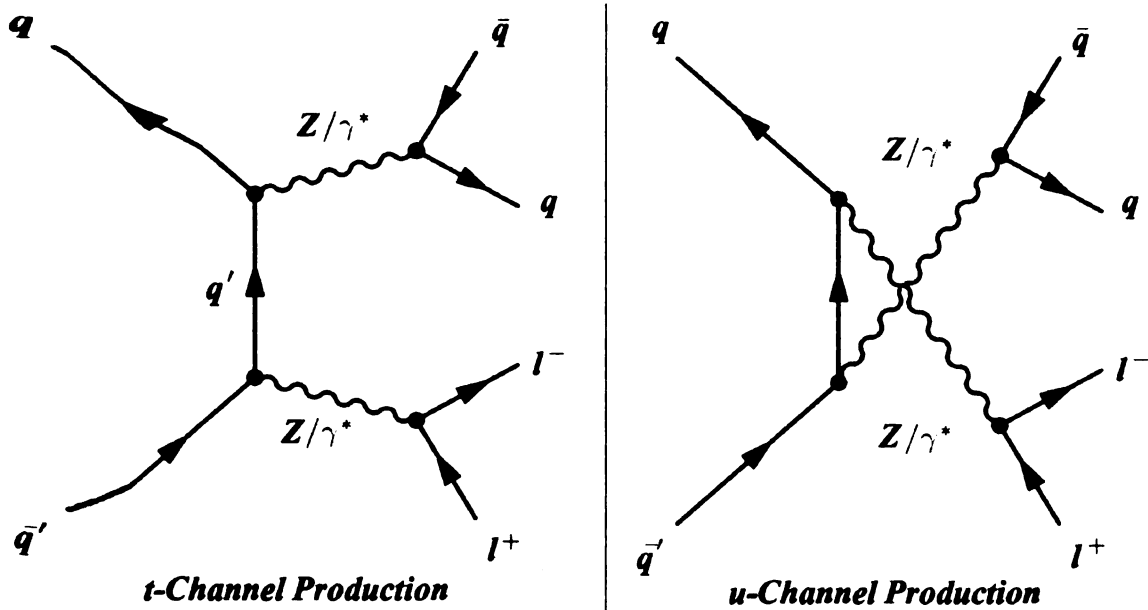


Figure 1.3: The leading order Feynman diagrams for  $ZZ$  process. The left one for  $t$ -channel process, and the one on the right is for  $u$ -channel process. The decay products reflect that this analysis covers only two leptons and two jets final states.

For the leading order Feynman diagrams please see Figure 1.3.

The leptons are required to have charges –excluding  $\tau$  final states–. Therefore the possible two final states for this process is  $eejj$  and  $\mu\mu jj$ . Although it is relatively easy to construct  $Z$  from leptons, it is a big challenge to construct  $Z$  from jets due to large volume of backgrounds. These channels suffer most from the simultaneous production of jets along with a  $Z$  boson.

The theoretical calculations of the cross section for  $ZZ$  production in the Tevatron is 1.46 pb[14]. As it is evident, this signal is very feeble and it is not expected to see more than 10 events for the whole RunIIa data taking period.

# Chapter 2

## Experimental Apparatus

*“The moment Hayy realized that  
all exists is His work, he saw things  
in a new and different light.”[16]  
Ibn Tufayl*

The previous chapter builds some interest in di-boson physics. In order to check and correct our theories we need experiments. Understanding the detector, its capacities and pitfalls, plays an important role in what type of physics can be tested. This chapter gives a minimal description of the accelerator facility, Tevatron and the DØ detector used for collecting data.

### 2.1 Fermilab

Chicago, the Windy City, is one of the most renowned and sought after cities in the world with its skyscrapers, beautiful location near the Great Lakes, and one of the attraction centers in the world by being “an American cultural capital” [17]. To a particle physicist however, it is the city which hosts the World’s highest energy machine, the Tevatron at Fermilab, in one of its suburbs.

Originally named as the National Accelerator Laboratory, Fermilab was commissioned by U.S. Atomic Energy Commission on November 21, 1967; built and has



Figure 2.1: An aerial view of Fermilab facility at village of Weston, 40 miles west of Chicago, IL. Tunnels of Main Injector, Tevatron and fixed target experiments can be seen. In the photo, one could see the north-east side of the Fermilab in the distance.

been operated by Universities Research Association since its founding. Renamed in honor of Enrico Fermi, on May 11, 1974 [18]; Fermilab defines its mission as “advancing the understanding of fundamental nature of matter and energy by providing leadership and resources for qualified researchers to conduct basic research at the frontiers of high energy physics and related disciplines”[19].

From the day with the first beam of 200 GeV energy (March 1977) to this day, Fermilab had many discoveries, among them bottom quark in 1977 and top quark in 1995 [20], merited many praises, among them International Mechanical Engineering Landmark from ASME [18]; all of which were possible with the accelerators(Main Ring -now Main Injector-,Tevatron) and the detectors(fixed target detectors, CDF, DØ) it is home to.

Not only is Fermilab one of the fore runners of advanced physics, but also it makes available the technologies developed there to the public. The connection

between public and Fermilab is on all levels. The prairie conservation site and the American bison keep its prairie connections alive and provides the local community with environmental richness .

Science is not just making elegant calculation for its devotees, it has an artistic side to it. It is very easy to grasp that by just visiting the site and seeing the sculptures made by scientists who genuinely combined art and science in their work.

## 2.2 Particle Accelerators

Charged particles can be accelerated by means of electro-magnetic fields, and with sufficient energies it is possible to observe “interesting things happen”, which usually means the creation of new particles that were absent before, by colliding a beam of charged particles with some targets.

Fermilab uses proton and anti-proton beams that are accelerated to kinetic energies of 980 GeV<sup>1</sup> in opposite directions to get a center of mass energy nearing to 2 TeV. In order to prepare these beams and give them the necessary energy, several different accelerator systems are utilized:

- Proton Source which is composed of Pre-accelerator, Linac and Booster,
- Anti-proton Source, which comprises Debuncher and Accumulator,
- Main Injector,
- Tevatron,
- Recycler.

---

<sup>1</sup>One eV (electron volt) is the amount of energy a particle of charge of an electron can get by crossing a potential difference of one volt. Thus one GeV equals  $10^9$  eV or  $1.602177 \times 10^{-10}$  J of energy.

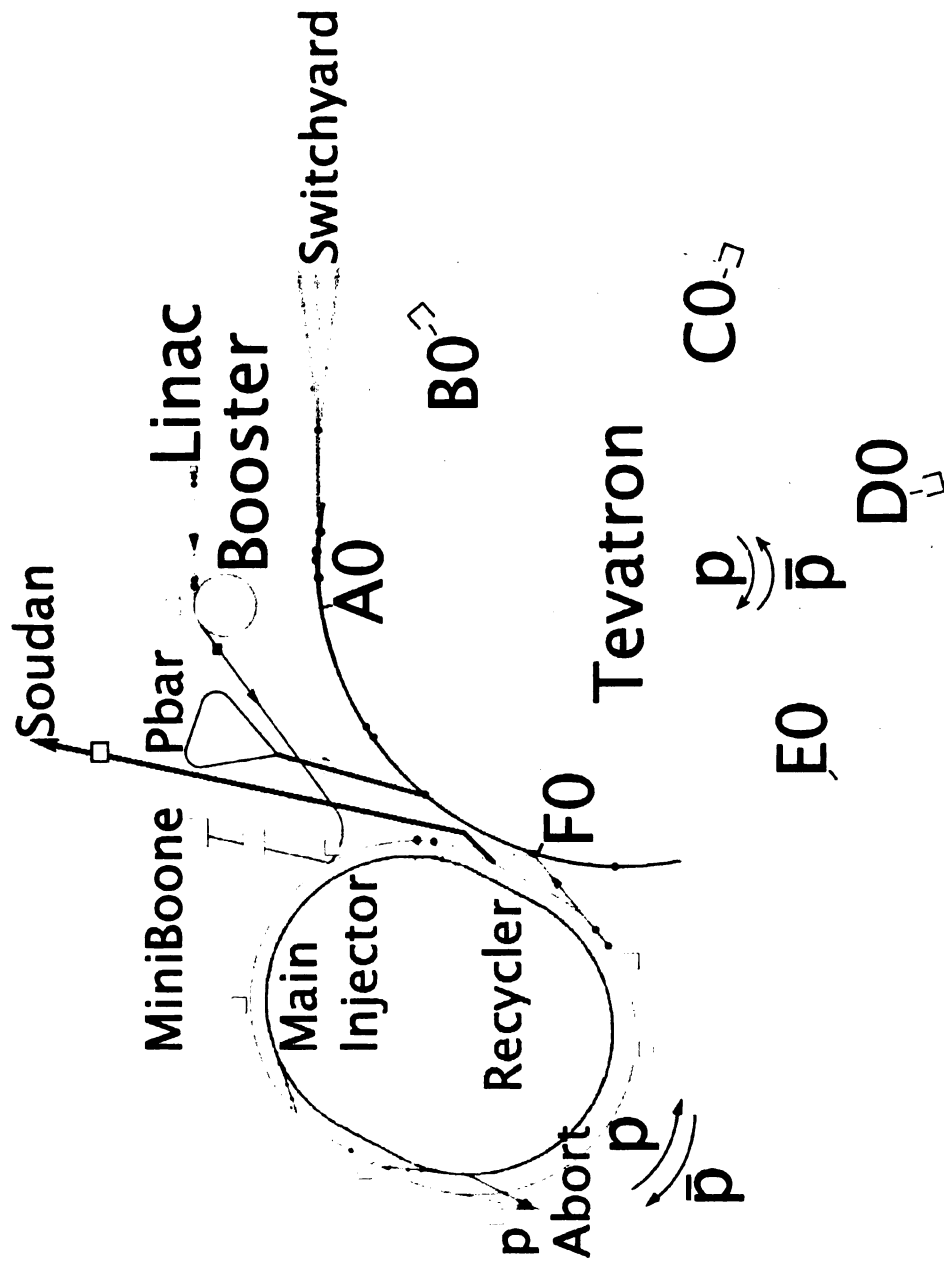
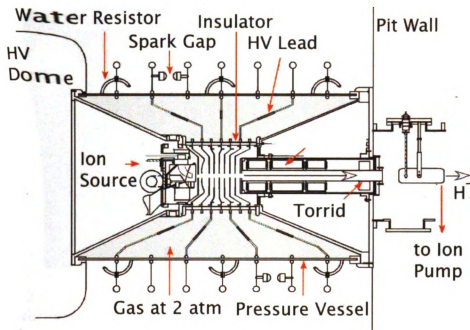


Figure 2.2: A schematic diagram of Fermilab's accelerator complex is shown in the figure. Drawings are smoothed at some points. The drawing is not scaled.





**Figure 2.3:** A detailed schematic diagram of Pre Accelerator. On the left side a part of the high voltage dome is shown.  $H^-$  leaves from the pre-accelerator from the right side with an energy of 750 keV.

### 2.2.1 Proton Source

Protons are essentially the nucleus of hydrogen atoms. So, as the easiest logical step hydrogen atoms are used in producing protons. Here it is described very briefly how.

The Pre-accelerator (Preacc) is the first accelerator in Fermilab's accelerator chains. It consists of a source -which converts hydrogen gas ( $H_2$ ) to ionized hydrogen gas ( $H^-$ )- resided in an electrically charged dome see Figure 2.3. The dome is charged to -750 kV. The ionized hydrogen gas is allowed to accelerate through a column from the charged dome to a grounded wall, therefore at the end of this process ions gain an energy of 750 keV. With a period of 66 ms, preacc can accelerate beams. After exiting the accelerating column, the beam is conveyed via a transfer line to the Linac.

The Linear Accelerator (Linac) increases the energy of the  $H^-$  beam that is

From  
Lent  
the  
of the

of the

of the

of the

of the

of the

of the

of the

of the

of the

of the

of the

of the

of the

of the

of the

of the





Figure 2.4: A picture of Fermilab's Linac. On the left is shown the drift tube Linac whereas on the right is shown the high energy part of the Linac. Both of the components make up the Linac.  $H^-$  ions enter the Linac at the drift tube side of the Linac.

delivered to it, from 750 keV to 400 MeV. It consists of two main sections, the low energy drift tube Linac and the high energy side coupled cavity Linac. In theory Linac also can accelerate  $H^-$  beam with a period of 66 ms, but this cannot be sustained for a long period of time without compromising safety.  $H^-$  ions may be transferred to one of two locations, based on the needs of that day: Booster which is last leg of proton source, or Linac dump, which is a large concrete block. The Linac is operated in three modes: High Energy Physics (HEP) mode referring to Booster transfer; Neutron Therapy Facility (NTF), for cancer treatment facility in this mode  $H^-$  are accelerated up to 66 MeV, and studies, dumps for various tune-ups or diagnostics.

The Booster, see Figure 2.5, is the last step to convert  $H_2$  gas into 8 GeV protons. It takes  $H^-$  ions that are accelerated to 400 MeV from the Linac, strips off their electrons by means of a carbon filter, and accelerates the remaining protons to 8 GeV. It is the first synchrotron<sup>2</sup> in the chain of accelerators that a proton

<sup>2</sup>A synchrotron is a type of circular accelerator where the strength of the magnetic field that keeps the beam in its orbit and the radio frequency found inside the accelerating



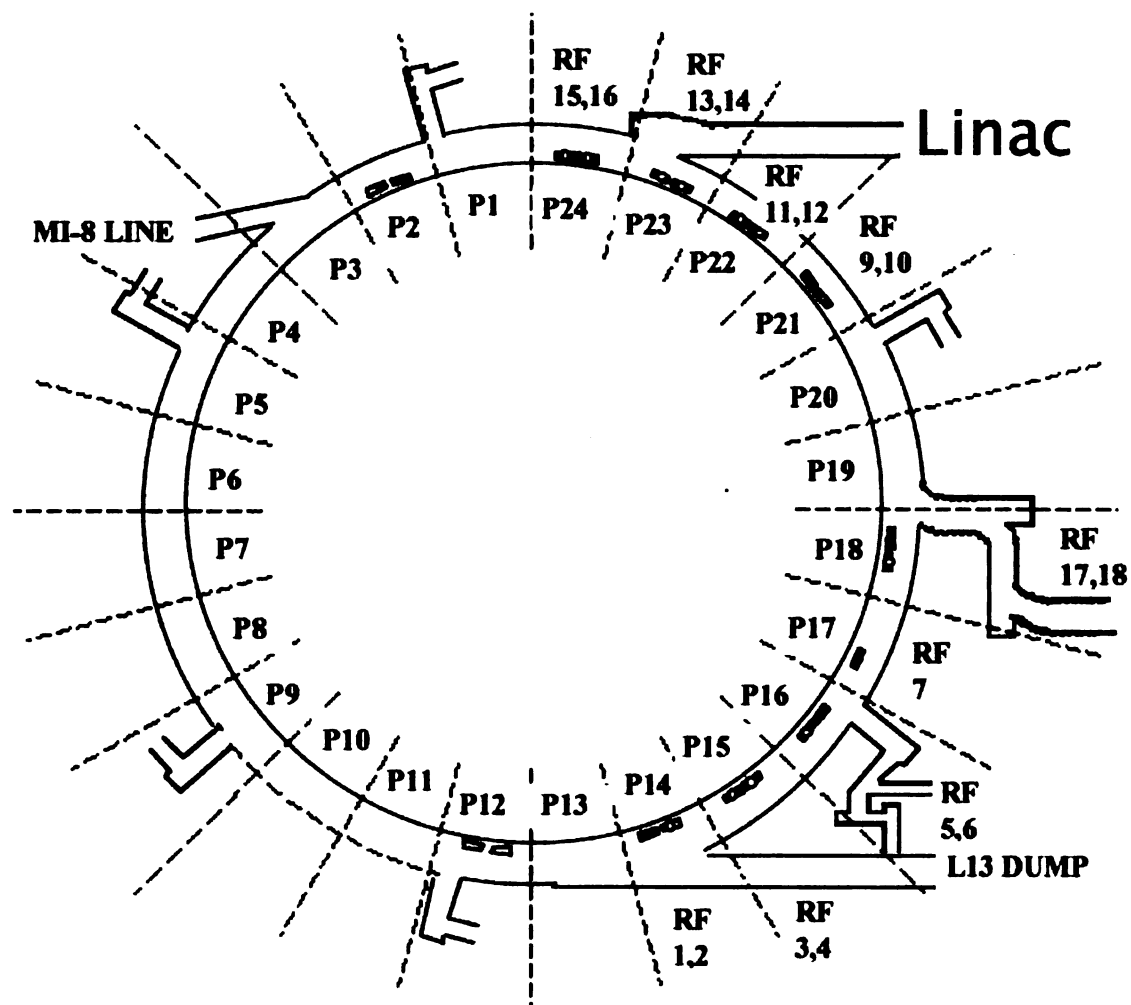


Figure 2.5: A schematic diagram of Fermilab's Booster. All the major components are shown as well as the locations of the RF cavities.

passes through at Fermilab. It consists of a series of magnets that are dispersed throughout of a 475 m circumference (75 m radius) circle, with 18 RF (radio frequency) cavities <sup>3</sup> interspersed. The Booster has a period of 66 ms for accelerating beams. As in the Linac the boosted proton beams can be guided to two different designated places according to the need: the MI-8 transfer line (Main Injector line carrying 8 GeV particles), or beam dump. Beams leaving the Booster via the MI-8 line can be used either in HEP mode or sent to MiniBooNE (Mini Booster Neutrino Experiment) for producing the neutrino beam aimed at the MiniBooNE detector.

### 2.2.2 Anti-proton Source

We live in a world made up of matter, therefore in contrast to the production of protons we basically have no easy access to anti-protons. Production of antimatter is rather cumbersome and in our case it is very inefficient too<sup>4</sup>. Anti-protons are created by striking 120 GeV protons from the Main Injector onto a nickel target see Figure 2.6. This process creates a lot of secondary particles some of which are anti-protons. By means of magnets anti-protons with an energy distribution averaging at 8 GeV are selected and transported to the Debuncher.

The Debuncher is a synchrotron which has a shape similar to a rounded triangle with an average radius of 90 m. It is designed to accept pulses of anti-protons at 8 GeV from the target station and to reduce their momentum spread by means of RF bunch rotation and adiabatic stochastic cooling while maintaining them at 8 GeV. There are two additional cooling systems which are used to reduce the beam region are synchronized to the beam momentum and revolution frequency.

---

<sup>3</sup>An RF cavity is basically a gap placed into the beam pipe across which an electric field is applied. They are electrically resonant structures with a natural frequency of radio frequency range. [21]

<sup>4</sup>The efficiency of this process is very low;  $10^5$  protons is needed to create one or two anti-proton.

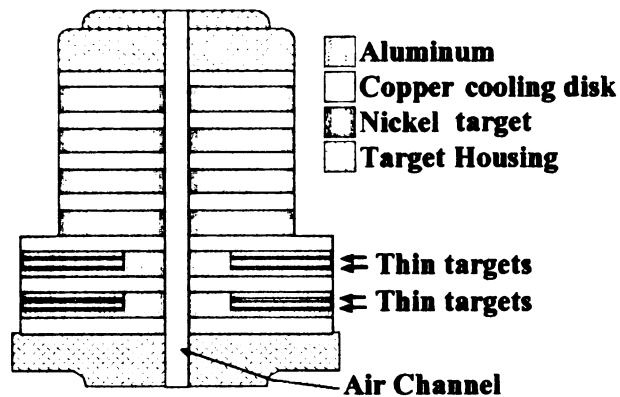


Figure 2.6: A schematic diagram of Fermilab's nickel target for anti-proton production. It consists of alternating disks of target (Ni) and cooling disks (Al). The target is rotated after a period of usage in order to preserve the targets shape.

spread in the horizontal and vertical directions.

The second synchrotron in the anti-proton source is the Accumulator which is also shaped like a rounded triangle with an average radius of 75 m. This system's purpose is to store anti-protons by stacking consecutive pulses of anti-protons from the Debuncher over a long time (several hours) until enough anti-protons are generated. The Accumulator has also several cooling systems: stack-tail momentum, core momentum, and core transverse. When enough  $\bar{p}$ 's are produced they are sent to Main Injector see Figure 2.7.

### 2.2.3 Main Injector

Protons and anti-protons are produced at a mean energy of 8 GeV, however the Tevatron is designed to accept beams of protons and anti-protons at energies of 150 GeV. During the RunI, the Tevatron was sharing its tunnel with the Main Ring which was responsible for accelerating protons and anti-protons to 120 GeV or 150 GeV depending on the need of the time. Due to complications of running the Main Ring and Tevatron at the same time in the same enclosure forced Fermilab to decommission the Main Ring and establish the Main Injector (MI) which is a smaller, faster and more efficient version of the Main Ring. The Main Injector

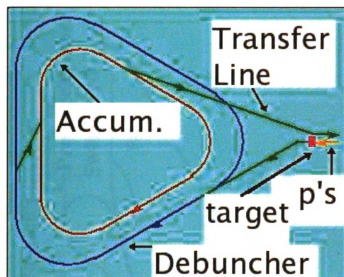


Figure 2.7: A schematic diagram of Fermilab's Debuncher and Accumulator. Protons with 120 GeV energy are hit on the target producing  $\bar{p}$ s. They are collected via a lithium lens and sent to Debuncher. Then they are transferred to accumulator (smaller triangular ring). Being a small ring, accumulator cannot store all the  $\bar{p}$ s, therefore  $\bar{p}$  are sent to Recycler via transfer lines.

is the second circular synchrotron in the accelerator chains of Fermilab after the Booster. See Figure 2.8. With its 18 accelerating RF cavities the Main Injector can accelerate 8 GeV protons from the Booster to 120 GeV for anti-proton production or 150 GeV for injection into the Tevatron. 120 GeV protons are utilized for fixed target experiments and neutrino experiments as well. The Main Injector is also used for transferring anti-protons from the Accumulator to the Recycler for further cooling and storing.

For more information please look at [21, 22]

## 2.2.4 Tevatron

The Tevatron is the largest most energetic synchrotron at Fermilab<sup>5</sup>. It has 8 accelerating RF cavities to increase the energy of the beams from 150 GeV to 980 GeV. The Tevatron is primarily a storage ring that's why beams are kept in it for

<sup>5</sup>The energy provided to the beams by the Tevatron is 980 GeV and its circumference is about 4 miles

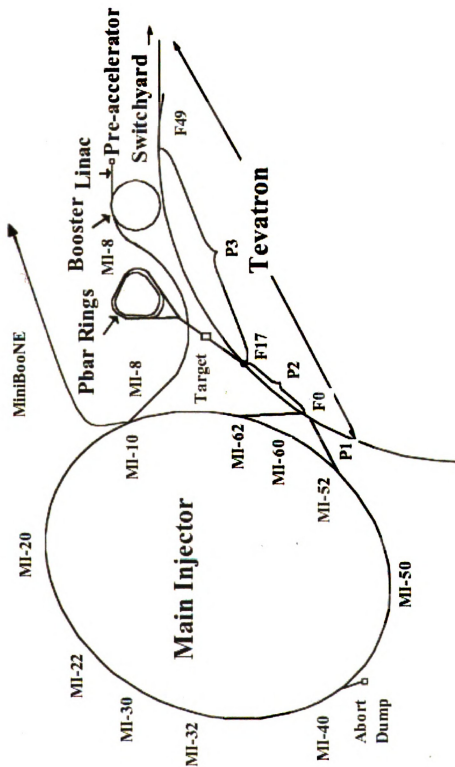


Figure 2.8: A schematic diagram of Fermilab's Main Injector, and its connections to its adjacent accelerator facilities. It is used for storing protons for further usage such as  $\bar{p}$  creation, neutrino creation, proton studies, Tevatron stores and the like.





hours until their quality degrades to a point where it is not efficient to keep beams, due to collisions at detector centers. It is the only cryogenically cooled (at 4 K) accelerator at Fermilab with about 1000 superconducting magnets which provide a field of 4.2 Tesla to keep the beams in orbit.

There are two modes of operation for the Tevatron, collider mode and studies mode. In collider mode protons and anti-protons are injected into the Tevatron from the Main Injector at 150 GeV energy respectively. These two beams of particles form a double helix around each other. The protons circle through the beam pipe clock-wise and anti-protons counter clock-wise. The proton and anti-proton beams are divided into 3 trains (super-bunch) and each train contains 12 bunches. The bunches in a super bunch are separated by 396 ns from each other. The time between any two super bunches is  $2.65 \mu\text{s}$ . When the Tevatron is filled with 36 bunches of the two beams, the energies of the beams are ramped up to 980 GeV, giving rise to  $p\bar{p}$  collisions at the center of mass energy of  $\sqrt{s} = 1.96$  TeV every 396 ns. Please refer to the Figure 2.9 for the relative locations of the bunches of the proton and anti-proton beams.

The Tevatron is divided into 6 sections labeled 'A' through 'F'. Each section has 5 buildings labeled '0' through '4'. Each '0' location has a straight section with a special purpose. The CDF detector and collision hall is located at the B0 straight section and the DØ detector and collision hall is located at the D0 straight section. At these two locations proton and anti-proton beams are squeezed and steered towards each other and forced to collide with each other. The duration of these collisions are called a '*store*' which lasts about a day if no problems occur.

For more information about the Tevatron please see[21, 23].

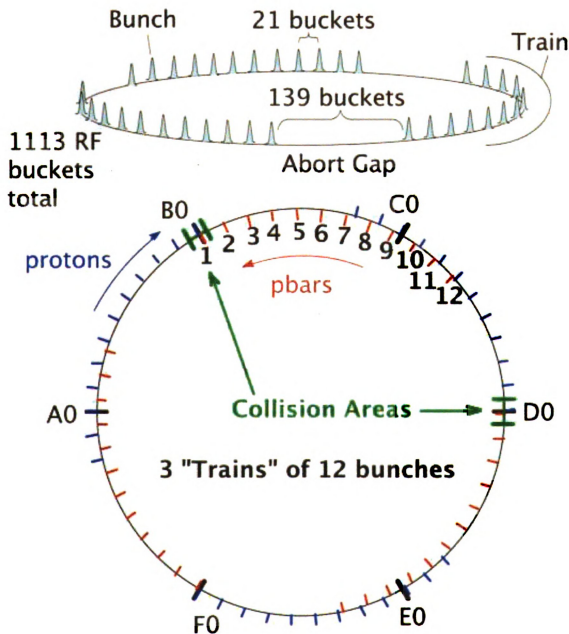


Figure 2.9: A schematic diagram of Fermilab's Tevatron showing the relative locations of the beams inside it. There are three "trains" of twelve bunches. The bunch to bunch spacing is  $396 \text{ ns} = 21 \text{ RF buckets}$ . The abort gap between the trains of  $2.617 \mu\text{sec}$  buckets. Different bunches in a train encounter the opposing beam at different places around the ring.

### 2.2.5 Recycler

The Recycler shares the same tunnel and is located just above the Main Injector. The primary purpose for building this machine was to reduce the time to have enough anti-protons by re-cycling anti-protons from the previous store. Due to technical difficulties, nowadays the Recycler is used only to store anti-protons for longer hours and to cool them down beyond the capabilities of the Accumulator. Stochastic cooling and electron cooling techniques are employed to cool anti-protons to the desired level of intensity. The Recycler has only permanent magnets.

For more information about the Tevatron please see[21, 24].

## 2.3 DØ Detector

As stated previously proton and anti-proton collisions happen at two points in the Tevatron tunnel, B0 and D0. In this section we will explain the detector which resides at D0 section of the Tevatron.

The DØ detector, see Figure 2.10, is a general purpose hermetic detector with a solid angle coverage of nearly  $4\pi$ . It is designed to study particles that are remnants of hard scatter collisions of  $p\bar{p}$ . The detector itself is built from inside-out in a layered fashion so that short lived particles are detected and measured first. The detector's components can be listed radially outward as:

- tracking system
- pre-shower detectors
- calorimeter and inner cryostat detectors
- muon detector

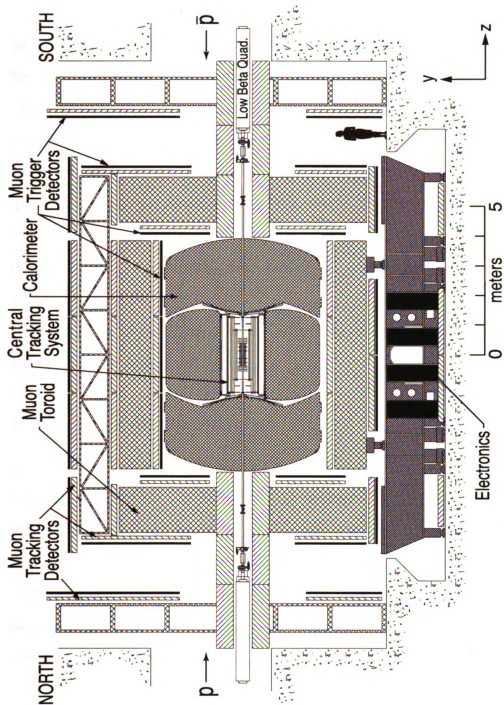


Figure 2.10: The schematic view of the cross section of the DØ detector. The figure is scaled. The beam pipe carrying proton anti-proton beams passes through the center of the detector. The direction of the proton beam is assigned to positive  $z$  direction. From the center of the detector in radial direction the following detectors are located: Central Tracker (Silicon Microstrip Tracker, Solenoid), Preshowers, Calorimeters Inter Cryostat Detectors, Luminosity Detectors, Muon Detectors.

Besides these components, the DØ detector has its own luminosity measuring detectors. Another important part of the detector is the trigger system which is not used for particle detection but used for selecting interesting events as most of the collisions between  $p\bar{p}$  beam are not capable of producing hard scatter events. This is due to the fact that momentum carried by a proton or anti-proton is distributed between the valance partons in the hadron. Thus many of the collisions produce stray particles going in the direction of the beam pipe. Even when a hard scatter occurs, from the signatures the particles leave behind, one can discriminate against uninteresting events (not containing weak bosons, or heavy quarks) by means of a trigger system.

Before going into detector components an introductory information about the detector's coordinate system will be given.

### 2.3.1 DØ Coordinate System

Choosing a reference point is necessary for every measurement, and the measurements done at the DØ are not different. The definition of a coordinate system for DØ is as following (see Figure 2.11): The origin of the right handed Cartesian coordinate system ( $x=0, y=0, z=0$ ) coincides with the central point of the DØ detector. The  $+z$  axis of this coordinate system is along the beam line in the direction of proton beam (clockwise in the Tevatron).  $+x$  axis points away from the center of the Tevatron ring and  $+y$  axis is pointing upwards.

In experimental high energy, one often finds oneself in need of transforming quantities such as speed or momentum from one frame to another. This process is not so simple requiring to make Lorentz transformations of the form

$$\beta'_L = \frac{\beta_L - \beta_v}{1 - \beta_L \beta_v} \quad (2.1)$$

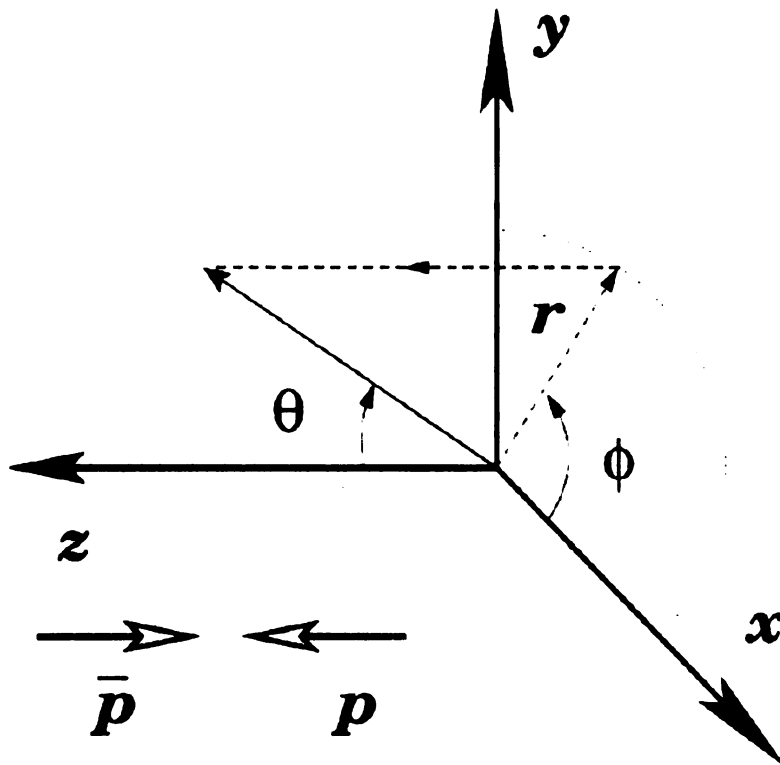


Figure 2.11: The orientation of right handed coordinate system of the DØ detector. The direction of the movement of proton beam is accepted as positive z-direction; negative z-direction is assigned to the direction of anti-proton beam. y-axis is chosen skywards and x-axis points in the opposite direction of the center of the Tevatron ring.

By making  $\beta_L = \tanh y$  parametrization this equation becomes

$$y' = y_L - y_v \quad (2.2)$$

and boosts along the movement become additive changes to this new parameter.

This parameter is called *rapidity* and is defined as

$$y = \frac{1}{2} \ln \frac{E + p_L}{E - p_L} \quad (2.3)$$

where L stands for ‘longitudinal’ (along the beam direction). For massless particles or very energetic ones one can approximate  $E = p$  and  $p_L = p \cos \theta$ , so that rapidity depends only on the direction. The resulting expression is used for massive particles as well since measuring  $\theta$  is easier, then it is called as ‘pseudo-rapidity’ and defined as

$$\eta = \frac{1}{2} \ln \frac{1 + \cos \theta}{1 - \cos \theta} = -\ln \tan \frac{\theta}{2} \quad (2.4)$$

and it is a very good approximation when the particles are moving close to the speed of light.

It is practically impossible to account for every particle produced by the collision since some of them escape through the beam pipe, which results in the inability of using momentum conservation, yet one can still use momentum conservation in the plane perpendicular to the beams movement, the transverse plane. To do this effectively several variables are defined.

$$E_T = E \sin \theta = \frac{E}{\cosh \eta} \quad (2.5)$$

$$p_T^2 = p_x^2 + p_y^2 = p^2 \sin^2 \theta = \frac{p^2}{\cosh^2 \eta} = \frac{p_x^2}{\cos^2 \phi} = \frac{p_y^2}{\sin^2 \phi} \quad (2.6)$$

Finally there is one other important relation which is used quite often

$$\Delta R = \sqrt{(\eta_i - \eta_j)^2 - (\phi_i - \phi_j)^2} \quad (2.7)$$

This relation defines the separation between  $i^{th}$  coordinate from  $j^{th}$  coordinate in a Lorentz invariant fashion. This variable lets us to discuss separation of the particles without referring to the frame of reference.

Although in the Tevatron, most of the time there is only one collision per bunch, due to the widths of the beams, the collision doesn't take place at the center of the detector all the time. Because of this fact, unless it is stated otherwise, the center of the coordinate system used for defining previous variables is taken to be the interaction point, which has a spread of about 25 cm around the detector's center. Thus,  $\eta$  calculated with respect to detector center is called *detector eta*,  $\eta_D$ , whereas  $\eta$  calculated with respect to event vertex is called *physics eta*,  $\eta$ .

### 2.3.2 DØ Luminosity Monitor

“The rate of interaction within a detector is given by

$$R = \sigma_{int} L \quad (2.8)$$

where  $L$  is the luminosity and  $\sigma_{int}$  is the cross-section of the interaction. The luminosity is a measure of the density of the particles in both beams.” [23]

Accurate measurement of the luminosity is very important since many measurable quantities depend on it. DØ's luminosity measurement is done by its luminosity monitor detectors placed at  $z = \pm 135$  cm from the detector's center. They have a coverage of  $2.7 < |\eta| < 4.4$ . These monitors are made up of twenty four wedge shaped scintillating tiles which have a thickness of 1.6 cm and length of 15 cm. The monitors provide an acceptance of about 98% for inelastic collision



detection, see Figure 2.12.

Another important quantity is the integrated luminosity which is a measure of collected data,  $\int L dt$  where  $L$  is *instantaneous luminosity*. In particle physics its unit is usually expressed in inverse barns  $bn^{-1}s^{-1}$ . The definition of the production cross section of any given process is given by

$$\sigma = \frac{dN/dt}{L} \quad (2.9)$$

where  $N$  is the expected number of events and  $L$  is the instantaneous luminosity. Therefore one can write cross section as

$$N = \sigma \int L dt. \quad (2.10)$$

### 2.3.3 DØ Tracking Detectors

Tracking detectors are used for the measurements of the momentum of the charged particles<sup>6</sup>. The idea is to form a path for every particle from the traces they leave behind, then to calculate the curvature of the paths to evaluate the momentums. For this purpose a light media should be used in order to decrease energy loss due to interactions between the media and the particles.

The tracking system was renewed completely for RunII. It covers a range of  $|\eta| \leq 3$ . The tracking system at DØ resides inside a 2 Tesla super conducting solenoid magnet. The magnetic field it produces is in the beam direction,  $z$ -axis. The magnetic field both helps to measure the charge of the particle and the momentum of the particle by bending the particle in the tracking system. Measurements of positions of primary and secondary vertexes, in the event are also done by the tracking system.

---

<sup>6</sup>Neutral particles do not interact with magnetic fields, thus they do not curve in the presence of a magnetic field.

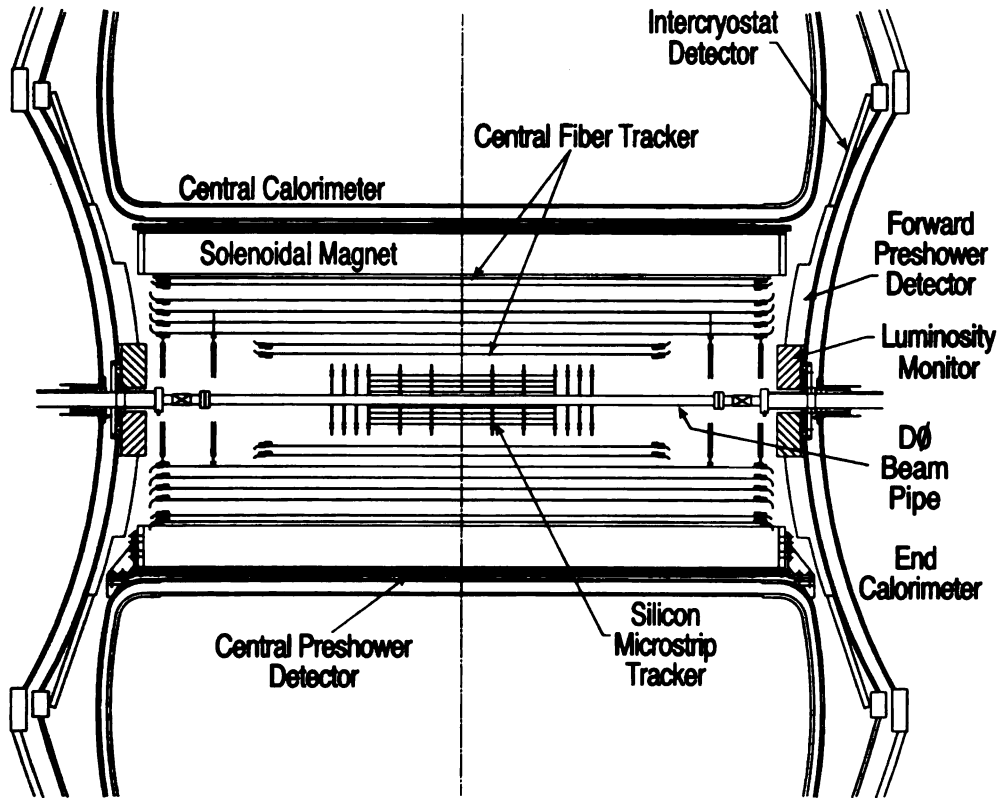


Figure 2.12: The schematics of the DØ detector's tracking system. Silicon Microstrip Tracker (SMT) is surrounded by Central Fiber Tracker (CFT). During the RunII upgrade phase, another tracking detector is placed in the region between the beam pipe and SMT, layer-0 detector, which has increased the resolution of the beam spot and the tracks. The coverage of the tracker is up to  $\eta_D = 2$ . Since the central tracking system sits inside a 2 T magnetic field providing solenoid magnet, it is possible to measure the momentum of the particles from the curvature of the tracks.

The tracking system of the DØ has 2 sub-detectors, Silicon Microstrip Tracker (SMT), and Central Fiber Tracker (CFT), see Figure 2.12

### Silicon Microstrip Tracker (SMT)

This was the closest detector to the beam pipe during RunIIa<sup>7</sup>. The SMT is designed to have a very high position resolution so that it is possible to examine

<sup>7</sup>During the upgrade in 2006 Another detector 'Layer 0' is placed between SMT and beryllium beam pipe to regain the lost SMT sensitivity due to radiation coming off of the beams.

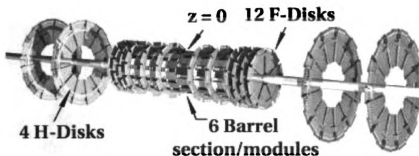


Figure 2.13: A nice picture showing the DØ detector's silicon micro-strip tracking system (SMT). It has six barrel shaped detector components laid in the direction of beam pipe. The barrels have four layers. 8 disks are dispersed between the six barrels and another four are further away from the center. The disks are placed perpendicular to the beam pipe.

the region closest to interaction points. See Figure 2.13.

The SMT is built from silicon wafers in two different shapes, rectangular ones forms concentric cylinders, 'barrels', running parallel along the beam pipe, wedge shaped ones are put into circular disks perpendicular to the beam pipe and dispersed among the barrels. There are six barrels and 16 disks (12 'F' disks, 4 'H' disks).

Barrels are 12 cm long and occupy the central region, hence they are used to identify particles with small  $\eta$ . Every barrel has four layers with both sides covered with silicon strips, see Figure 2.14.

On the other hand F-type disks stretch out radially from 2.5 to 9.8 cm from the beam pipe at the positions  $|z| = 12.5, 25.3, 38.2, 43.1$  and  $48.1$  cm. They are made of double sided silicon strips. The H-type disks are located at  $|z| = 100.4$  and  $121.0$  cm. H-type disks are built from single sided silicon strips.



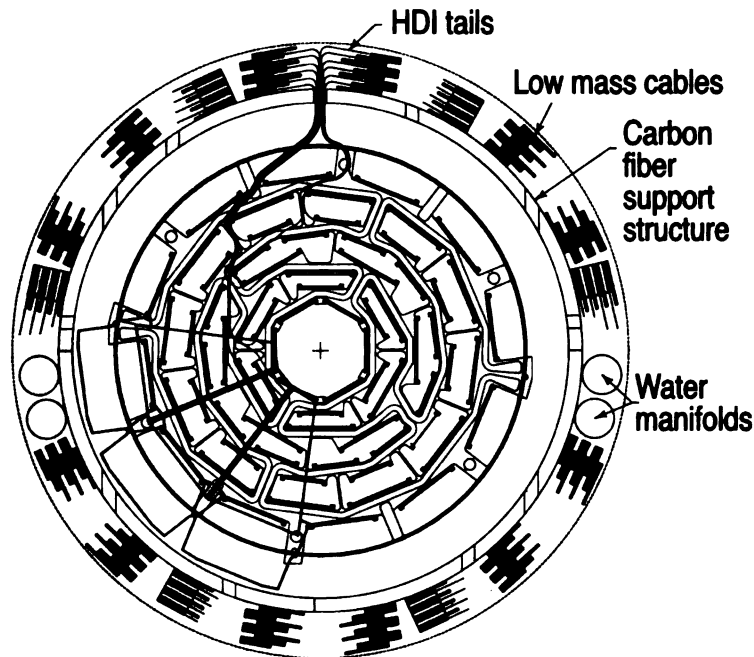


Figure 2.14: The picture showing the cross sectional view of the DØ detector's silicon **micro-strip** tracking system (SMT). The SMT barrels and their support structure are shown. Four double sided layers are placed consecutively.

### Central **Fiber Tracker** (CFT)

The CFT is the next detector for a particle to visit after its journey through the SMT. It covers the SMT completely with its eight equidistant super layers of scintillating fibers, see Figure 2.15 Its outer six layers are 2.5 m long whereas its inner two layers are only 1.7 m long in order to give room to the H-type disks of the SMT. The CFT's detection range is  $|\eta| \leq 2$ . Radially the CFT occupies a region from  $r = 20$  cm to  $r = 51$  cm with 76,800 fibers. Every super layer has one axial doublet layer (along  $z$  axis,  $x$  layer) and one stereo doublet layer ( $\pm 3^\circ$  from  $z$  axis,  $u/v$  layers). The axial layer is used for measuring  $\phi$  and stereo layers are used for measuring  $\eta$ . The resolution of the fiber doublets are about 100 micron. Compared to SMT, CFT is better for determining the transverse momentum ( $p_T$ ) of the particles due to the long range of radial coverage. The photons created by the passage of particles through the fibers are read by a Visible Light Photon Counter

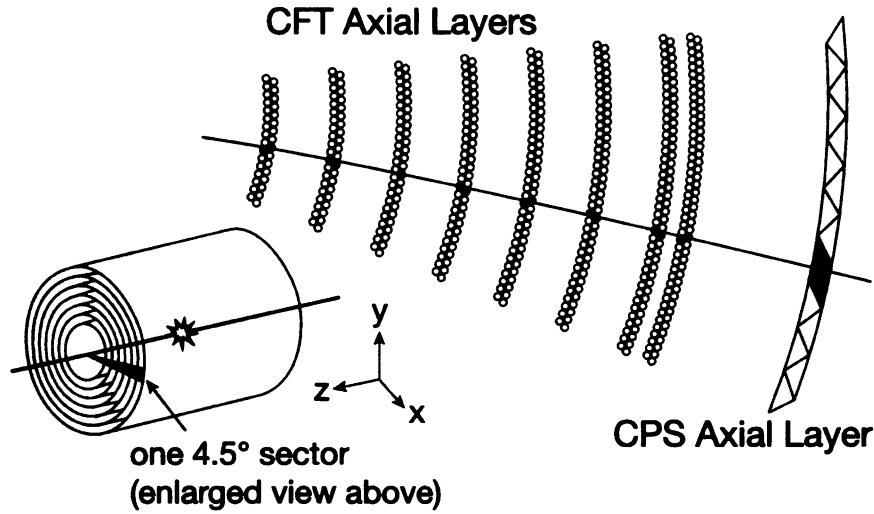


Figure 2.15: The picture showing the DØ detector's central fiber tracker system (CFT). Eight layers of scintillating fibers are used to get an accurate measurement of momentum measurement of the charged particles passing through the CFT. The solenoid is placed between CPS layer and the eighth layer of CFT, but is not shown in this figure.

(VLPC), a kind of photomultiplier. At their optimal operation temperature of 90K the photon detection efficiency of the VLPC is about 80%.

### 2.3.4 DØ Pre-shower Detectors

The placement of the solenoid at the center of the DØ detector degraded the calorimeter resolution, as it is uninstrumented. In order to regain it and improve separation of photons from electrons, DØ has another detector, the Pre-shower. There are three Pre-shower detectors, one for every calorimeter part, one central and two forward.

The part that sits between the tracking system and the Central Calorimeter is called the Central Pre-shower Detector (CPS) and has a coverage of  $\eta_D < 1.2$ . It is a cylindrical detector having a length of 2.73 m and a radius of 72 cm and cramped into a 5 cm gap. The CPS has three layers of scintillating strips of fibers. The central layer is axial whereas the outer two layers are situated with an offset

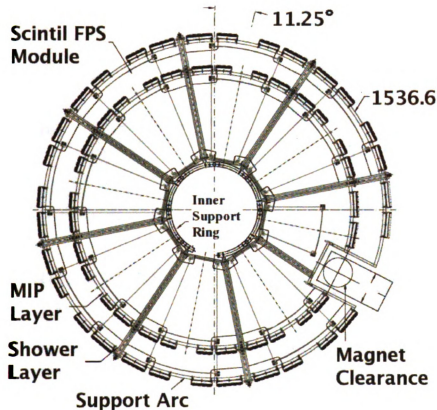


Figure 2. 16: Figure showing the forward preshower detector system (CFT). These detectors is placed between the central calorimeter and the end-cap calorimeters.

angle of  $\pm 22.5^\circ$  with z axis.

Two other detectors having the same constructional properties are located in front of the End-cap calorimeters. They are called Forward Pre-shower Detectors. Unlike the CPS they have four layers of scintillating fibers two u and two v type stereo layers. The main purpose of these are to improve electron photon separation power.

Every layer in these detectors is composed of triangles of scintillating fiber with a hole in the middle to accommodate wave-shifting fibers which carry the signal to waveguides which eventually transport signals to VLPCs. See Figure 2.16, 2.17. There are close to 23680 read-out channels for the pre-shower detectors.

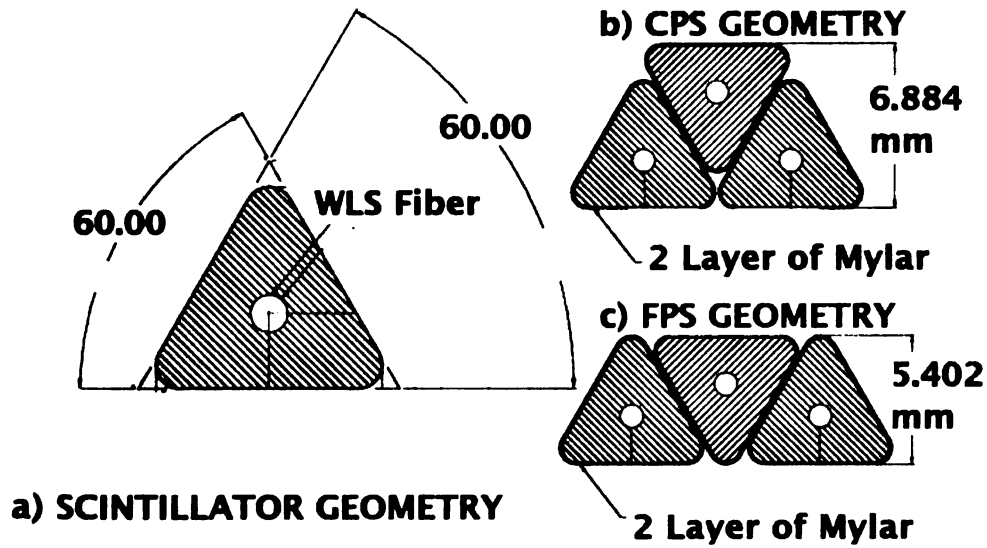


Figure 2.17: The figure showing the DØ detector's central pre-shower detector and forward pre-shower detector geometry. The geometry shows a little difference between the two detector systems, but in both of the detectors triangular scintillating fibers with a waveguide in the center are used to transfer light wave for position measurement.

### 2.3.5 DØ Calorimeter

The DØ calorimeter is one of the major parts of the detector. Because of that the DØ detector has such a big coverage in rapidity. Although there were some changes to the read-out system, the detector itself is the same as in the RunI period. It is designed to measure the energies of the jets of particles precisely.

The DØ calorimeter system is a sampling calorimeter system which uses depleted uranium ( $U^{238}$ ) as the absorbing material and liquid argon at 90°K as the sampling medium (active medium). It consists of three separate cryostats, one in the central region with an eta range of  $|\eta_D| < 1.2$  and one on either side of central cryostat, closing the detector from each side with an eta range of  $1.4 < |\eta_D| < 4.2$ . For a depiction of the calorimeter see the Figure 2.18. The one in the center is called Central Calorimeter (CC), and the others are appropriately called End-cap Calorimeters (EC). The Central Calorimeter (CC) is composed of three sections,



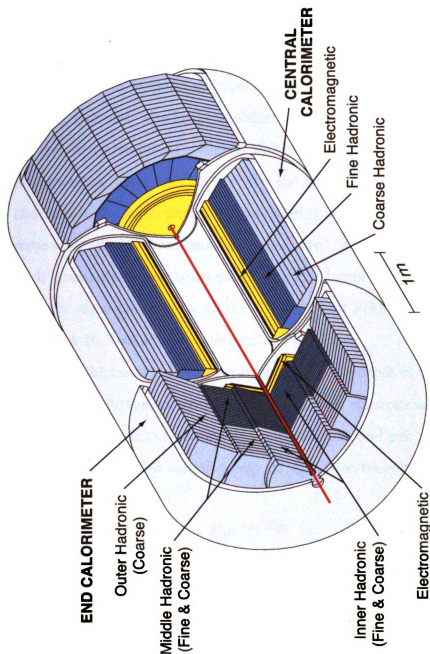


Figure 2.18: The DØ calorimeter. The regions shown yellow and dark blue are built by depleted uranium to contain showers of the particles in a small volume. The rest is built with steel and copper. The calorimeter is cryogenic. The region between the layers of metals is filled with liquid argon as active media. The calorimeter has three parts: North End-cap Calorimeter, Central Calorimeter and South End-cap Calorimeter. The cylindrical hollow region in the center houses the tracking system of the DØ detector.

electro-magnetic (EM), fine hadronic (FH), and coarse hadronic(CH). In the radial direction the CC is made up of 4 EM layers, 3 FH layers and 1 CH layer. The absorbing plates are 3 mm thick uranium plates in the EM layers whereas in the FH they are made of 6 mm uranium-niobium alloys. The CH has 46.5 mm copper plates as absorbing material. The End-cap Calorimeters (EC) are composed of the same sections but their orientation is slightly different. The EM layers are placed closest to the interaction point after them comes the fine hadronic layers, depending on the closeness to the beam pipe, they are called either inner, or middle. The CH layers come after the FH layers and are named inner, middle, and outer with respect to their proximity to the beam pipe. The EM layers and the FH layers of the EC have the same properties with the CC's EM and FH layers but its CH layers are built with 46.5 cm stainless steel instead of copper.

The choice of the thickness of the absorber plates and the depth of the layers is optimized according to the type of interaction. EM objects, electrons and photons interact with the uranium via two processes: bremsstrahlung and pair production. The energy of an electron with initial energy of  $E_0$ , after traveling through  $x$  amount of material is

$$E(x) = E_0 e^{-x/X_0} \quad (2.11)$$

where  $x$  is the distance traveled in the material and  $X_0$  is the radiation length for the material.  $X_0$  is defined as the average distance over which a high energy electron loses 63.21% of its energy ( $1 - 1/e$ ); and for photons as  $7/9$  of the mean free path for pair production. It is 3.2 mm for uranium. Hadrons interact with the uranium via the strong force. Secondary particles created by the interaction are mostly neutral pions,  $\pi^0$ , that decay to photons without delay. The rest of the secondary particles continue interacting strongly, and this results in the spread of the hadronic showers. The equation is similar to equation 2.11 with the replacement of  $X_0$  with  $\lambda_0$  nuclear radiation length.

Fluor  
Sulfur  
Nitrogen  
Carbon

Tr

Hydro

Chlorine

Phosphorus

Calcium

Sodium

Potassium

Magnesium

Iron

Copper

Lead

Mercury

Barium

Strontium

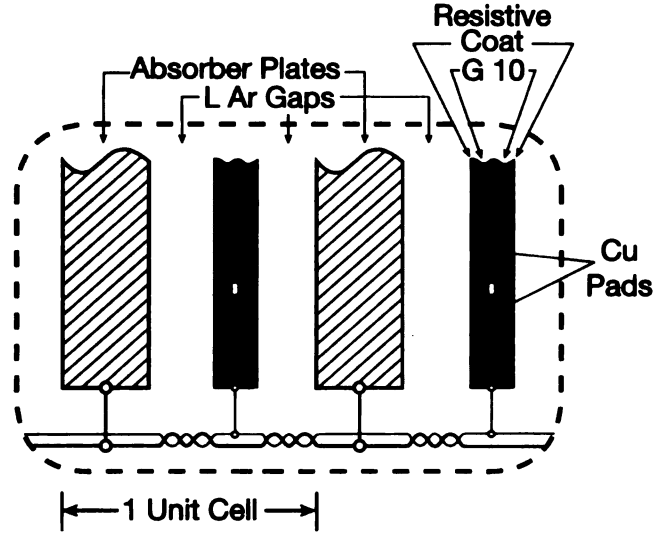


Figure 2.19: A nice picture showing the unit of the calorimeter cell of the DØ detector. The thickness of the uranium absorbing plates differs depending on which layer it is located. Between the plates resides the liquid argon as the active ionizing medium.

The energy measurement of the incoming particle is done by the charge collected in the fundamental unit of calorimeter, the gap. For a schematic drawing of this unit see Figure 2.19. Secondary particles (electrons, pions) from the shower, ionize liquid Argon. These electrons move under the influence of the high voltage electric field and accumulate on the signal board. The drift time for electrons to reach the signal board is 450 ns at most. From the signal board the charge is sent to pre-amplifiers. Earlier we mentioned that the calorimeter is built in layers like an onion. Every layer have several (not necessarily the same number of) gaps in them. In  $\eta \times \phi$  surface, every layer is divided into cells which have dimensions of  $0.1 \times 0.1$  ( $\Delta\eta \times \Delta\phi$ ) with one exception in third EM layer which has more fine segmentation  $0.05 \times 0.05$  ( $\Delta\eta \times \Delta\phi$ ). The reason for this finer partition is that this layer corresponds to the maximum of an EM shower. Although this was correct in the RunI period, due to solenoid and pre-shower detectors the maximum of EM showers happens between the second and the third layer of the EM calorimeter. For

[illegible]

schematic views of a calorimeter quadrant refer to Figure 2.20. Although cell sizes don't change in  $\eta \times \phi$  space, in the lab frame they change, as the second exception, for high  $\eta$  values ( $|\eta_D| > 3.2$ ) the sizes of the cells are increased to  $0.2 \times 0.2$  in all layers. The total number of cells, or read-out channels is on the order of 50,000, which are grouped into projective towers whose number is on the order of 5,000 see Figure 2.20.

The regions where ECs and CC meet are called 'inter cryostat region's (ICRs). In order to reduce the 'dead' region in the detector, two additional types of detectors are added to the calorimeters. The massless gap detectors are placed inside the cryostat covering  $0.6 < |\eta_D| < 1.3$ . They are ring shaped in  $\phi$ . They are similar to the gaps but don't have absorber plates, that's why they are called massless. The second type of detector is the 'inter cryostat detector' (ICD), which is again a ring in  $\phi$  covering  $1.1 < |\eta_D| < 1.5$ . Its structure is similar to the pre-shower detectors.

The read-out chain for the calorimeter is shown in Figure 2.21. A charge proportional to the lost energy of the particles passing through the cells is sent to the read-out electronics. This charge is integrated in the preamplifier, and turned into a voltage. These voltage pulses are carried to baseline subtractors (BLS), which shape the signal and remove the offsets in the input voltages. The signal is sampled at its peak at around 320 ns, which corresponds to only a portion of the actual signal (2/3). These signals are, then, stored in switched capacitor arrays (SCAs) until a trigger accept decision is sent, otherwise they are discarded. The trigger system is explained later. If the signal has high probability of containing heavy particles, then it is digitized by analog to digital converters (ADCs) and sent to the data acquisition system (DAQ). The read-out system is designed to handle data input up to a level1 rate of 10 kHz.

The calorimeter design criteria for the energy resolution are given as below.



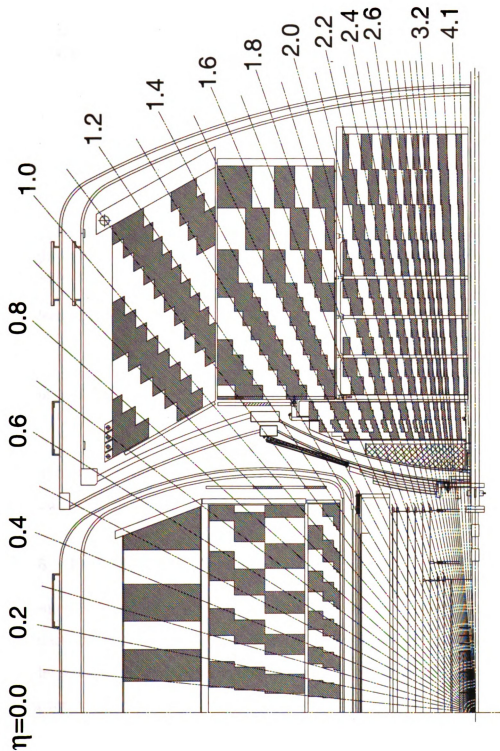


Figure 2.20: The cross sectional view of calorimeter quadrant. In this picture the calorimeter towers are shown as differing colors centered at the center of the calorimeter. For trigger system two of these towers are combined together and an approximate energy measurement is done for fast response times.



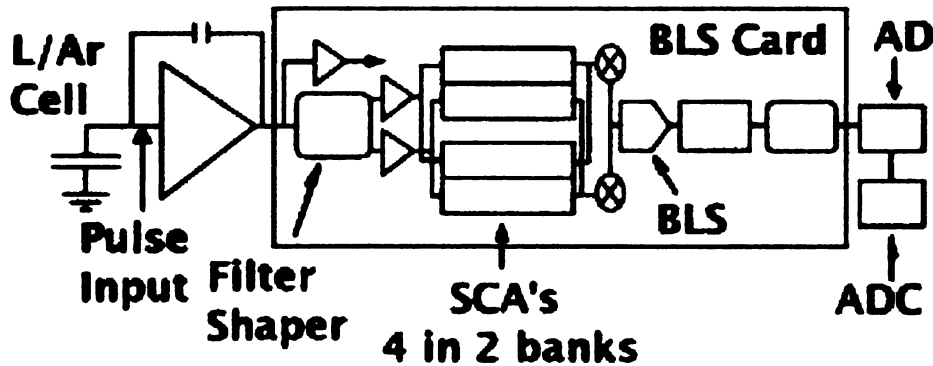


Figure 2.21: The schematics of the calorimeter readout chain. Every cell can be thought of as being a big capacitance charged according to the energy of the incoming particles. At the end of this chain the energies of the particles are digitized.

For electromagnetic energy

$$\frac{\sigma_E}{E} = \frac{0.15}{\sqrt{E}} \quad (2.12)$$

and for hadronic energy

$$\frac{\sigma_E}{E} = \frac{0.50}{\sqrt{E}} \quad (2.13)$$

However, the new material in front of the calorimeter worsened these resolutions in RunII.

### 2.3.6 DØ Muon Detectors

The outermost sub-detector in the DØ detector is the muon detector which is also manufactured in layers like all the other systems explained until now.

The muon detector is a cubic detector having four layers one of which is the muon toroid providing the necessary magnetic field to bend muons. The layers are placed in the following order: A layer, toroid, B layer and C layer. Due to being a cubic detector it has four sides running parallel to the beam pipe which are called muon central (MUC); the other two sides which are perpendicular to the beam pipe are called muon front (MUF). Being a rectangular detector MUC

covers approximately a range of  $|\eta| < 1$  and MUF covers from that point until approximately  $\eta < 2.0$ .

All the layers in both MUC and MUF contain wire chambers (drift tubes), depending on the position they contain scintillators too. Drift tubes (PDTs in MUC and MDTs in MUF) are used to measure position  $z$  and either  $x$  or  $y$ . The scintillators are used for  $\phi$  measurements as well as timing for triggers and background reduction. See Figures 2.22, 2.23 for inflated schematics of three layer of MUC and MUF for both drift tubes and scintillators. As mentioned above the toroid is located between A and B layers and provides a magnetic field of 1.8 Tesla. Drift tubes contain an ionizing gas and high voltage anodes(4.7 kV) and cathodes(2.3 kV). When a particle enters, it ionizes the gas and electrons are collected on the anode. From the drift time it is possible to locate where the particle hit in the tube with good precision ( 1mm for PDT, and 0.7 for MDT). The drift times for PDTs and MDTs are 490 ns and 10 ns respectively.

MUC coverage is compromised at  $4.25 < \phi < 5.15$  (can be seen in the Figures 2.22, 2.23) due to the fact that detector systems placed inside(calorimeter, tracking system) and readout electronics need support. Besides this MUC and MUF detectors have other gaps due to construction in  $\phi$  octants.

### 2.3.7 DØ Trigger System

An other component of the DØ detector, which is not used for measurements but plays a rather important role in data taking is the DØ trigger system. It is the system that selects events that are worth to keep for further processing. It may be tempting to analyze all data that is produced by the detector; however, this is impossible with today's technology. The collision rate at the Tevatron is 2.5 MHz, which corresponds to approximately 425 GB of data per second. This amount of data is impossible to write to tapes. Besides, most of the collisions happen in a

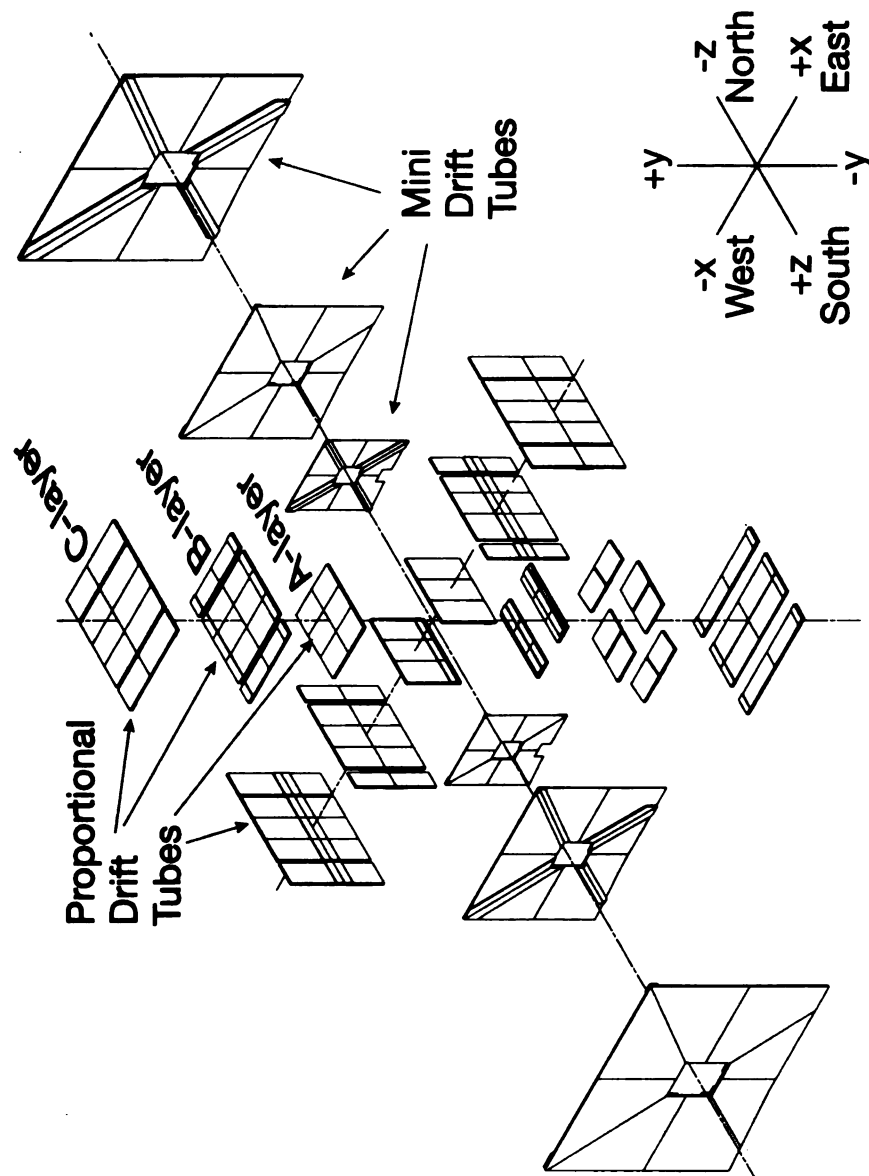


Figure 2.22: The schematic picture of the muon drift chambers are shown in all the layers. Due to the presence of the detector support, the bottom side of the detector coverage is partial.



way that doesn't produce a head on collision which has the potential to produce the particles related to the processes of interesting physics, such as W or Z bosons.

It is the responsibility of the trigger system to pick events with high probability of containing interesting physics objects such as bosons. The system consists of three stages: The Level-1 (L1) trigger system which makes very fast decisions by hardware level instructions, the Level-2 (L2) trigger system is a mixture of hardware and software; and the Level-3 (L3) carries out selections by a software system which takes the longest time between the three due to complexities of the instructions.

### The Level-1 Trigger

As shown in Figure 2.24 the decisions made by L1 trigger system are based on information given by four sub-detector systems: the calorimeter, the central fiber tracker, the muon and the forward proton detectors<sup>8</sup>. The L1 trigger decisions related with these detectors are made by their corresponding trigger systems. These systems use information collected by the detectors to feed L1 trigger framework with an acceptance decision named as an AND/OR term. Depending on the result of the AND/OR terms and the availability of the data acquisition system, the L1 Trigger System either issues an accept decision and sends the event to L1 Trigger System or a reject decision and discards the event.

The Level-1 Calorimeter (L1Cal) trigger uses a special form of calorimeter towers which are constructed from four neighboring standard read-out towers grouped together  $2 \times 2$ ; which means every tower has a cross sectional area of  $0.2 \times 0.2$  in  $(\eta, \phi)$  space. Totally, there are 1280 trigger towers for the calorimeter,  $\phi_D$  is divided in 32 and  $\eta_D$  is divided in 40 regions. The trigger towers are read separately as EM trigger towers and HAD trigger towers. The coarse hadronic part

---

<sup>8</sup>the forward proton detector was decommissioned at the beginning of the RunIIb

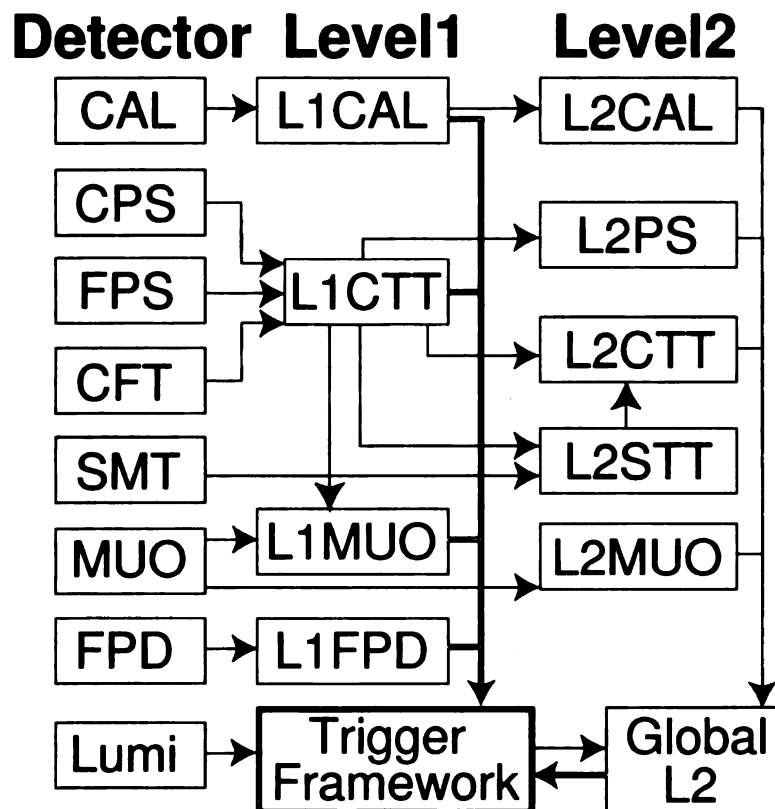


Figure 2.24: The data flow diagram of the Level-1 and Level-2 trigger systems. SMT is not used in the first level because of the time constraint on this system. Trigger framework is the decision maker and the messenger between the different detector components and read-out crates.

of the calorimeter, the massless gaps and the ICD detectors are not used in the triggering. The two parts of the trigger towers (EM and HAD) contain the sum of the energies in the EM layers and the FH layers of the calorimeter respectively. The energies in these towers are digitized in 8 bit numbers (ADC counts), and then converted to transverse energies (  $E_T(EM)$  and  $E_T(HAD)$  ). A low energy cut (pedestal removal) is applied at this point to remove noise. After calculating global  $E_T$  of EM and HAD for the entire calorimeter, the number of EM towers having an  $E_T$  above a certain threshold is counted. Both of these informations are used for making L1 Calorimeter decision.

The Level-1 Central Track Trigger (L1CTT) reconstruct tracks by only using CFT and CPS detector axial hits. The conditions for accepting an event is usually the number of tracks above a  $p_T$  threshold. The list of the tracks are passed to Level-1 Muon Trigger (L1Muon) system and TWF. L1Muon employs tracks consistent with a muon track pattern from the passed list and builds trigger objects by using both tracks and muon scintillator hits. An L1Muon trigger condition can be created by detector region, track quality and  $p_T$  threshold.

## **The Level-2 Trigger**

The L2 trigger system, builds physics objects by relating different components of the L1 trigger system for events passing the L1 triggers. It has access to more detector trigger systems. Its elements are shown in Figure 2.24. The L2 calorimeter (L2Cal) trigger runs EM and jet algorithms to form em objects (electrons and photons) and jets from EM and HAD trigger towers. The L2 Pre-shower (L2PS) is used to improve the electron photon separation efficiency. All the layers of PS detector are used to form track clusters. The L2 Central Track Trigger (L2CTT) takes information from both the L1CTT and the L2 Silicon Track Trigger (L2STT). It combines the L1CTT tracks and sorts, calculates several isolation criteria which

**help** increase trigger capabilities and  $\phi_0$  of the tracks with respect to beam axis. **Level-2 Muon** (L2Muon) produce muon candidates by combining track segments **and** layers of the detectors and sorts them in descending order of  $p_T$ . **Level-2 Pre-shower** (L2PS) is used in improving the detection efficiency of electrons. All the **information** from level-2 preprocessors are combined in **Level-2 Global** (L2GBL) **which** makes a decision of acceptance depending on the AND/OR terms. Then **that decision** is sent to TWF which eventually communicates with the read-out **crates** about sending the event to Level-3 triggers in the case of acceptance or **discarding** it in the case of rejection.

### **Level-3 Trigger**

**Accepting** an event at L2 causes the trigger system to send the event to the next **and the** final step Level-3 before writing the event to the tape for safekeeping. At this **system** all of the decisions are high-level (software). The trigger software is a **light version** of  $D\bar{D}$  reconstruction algorithm. Each detector system passes the **readout** information to the L3 farm nodes (high performance PCs). The events are **reconstructed** and by means of filters to identify physics objects such as jets and **muons**, **trigger** decision are made both on the objects and their inter-relations.

If **an** event passes an L3 trigger, it is sent to computing center to be recorded on **tape**.



# Chapter 3

## Event Reconstruction and Object Identification

*“The balance between the positive and the negative helps make it a safer environment. In any event, employ lots of data in the review. Because we’re a creative organization, people tend to assume that much of what we do can’t be measured or analyzed.”[25]*  
Ed Catmull

### 3.1 Introduction

Every collision passing trigger requirements is named as an event. Every event is composed of information from every active sub-detector system. At this stage an event is not very useful for physics analysis since it consists of digitized readout information for each channel of each sub-detector. These readouts are different for every sub-detector. For the calorimeter and silicon, it is the amount of collected charge, for the muon system it is time differences in the drift tubes and for scintillators it is the light yields. The software collected under the name DØreco is used to convert ‘raw’ data from each sub-detectors to physics objects such as muons or electrons. It also applies corrections from calibration and alignment studies.

## 3.2 Tracks

The tracking system is built in such a way that a charged particle leaves traces **along** its way through the SMT and the CFT detectors. By combining hits in the **consecutive** layers of this system it is possible to visualize a path where a particle **has passed**. Because of the presence of the magnetic field these paths are curved **allowing** one to measure their momentum and charge.

**DØ**reco starts building tracks from the data by first clustering hits in each layer of the SMT and the CFT. It uses two different algorithms, which take the energy **weighted** centroid of these clusters, in parallel. The two algorithms are called the Histogram Track Finder (HTF) and the Alternative Algorithm (AA).

The HTF algorithm uses the fact that a curve can be parametrized by  $\rho$ , curvature of the track,  $\phi$  the angular direction of the curve from the origin, and  $d_0$  the distance of the closest approach to the origin. Hits with the same  $d_0$  will produce a **line** in a  $\rho \times \phi$  histogram. Then hits that belong to the same curve should **intersect** at a point in  $\rho \times \phi$  space, and the corresponding histogram will have a local **maximum** at that point. Those hits which have the same  $(\rho, \phi)$  values should be on **the** same curve, then.

The AA algorithm finds track candidates by using the same technique in two **different** directions, from inside to outside, and in the reverse direction. It starts with **seed** clusters in SMT barrels or F-disks. Then tracks are built by searching a **second** cluster in any larger silicon layer within a window of  $|\Delta\phi| < 0.08$ . This **process** continues until three clusters are found. Then they are fit to a curve. If the **curve** has a  $d_0$  within 2.5 cm of the beam spot and its radius of curvature  $\rho$  is **greater** than 30 cm ( $p_T > 180$  MeV) and  $\chi^2$  of the fit is less than 16, then it is **accepted**. The same procedure is applied on the remaining layers of SMT and CFT in the order of increasing radius. If a multiplicity occurs due to getting the **same** track from different clusters, then both of the candidates are passed to the

**n**ext level of acceptance. This process is followed in the reverse order to find tracks **w**ith a few or no SMT hits.

After completion of both algorithms track candidates are eliminated by the **r**equirements on the number and type of missed hits along the candidate's path. **T**he tracks are processed by a Kalman fit algorithm which simulates the effects of **t**he non-uniform magnetic field, interaction of particles with the material in the **t**racking system and the beam pipe. Duplications due to processing twice are removed.

**T**hen the final list of the tracks are put into the event by the DØreco algorithm. These tracks have properties like curvature and distance of the closest approach ( $dca, d_0$ ) of the track with respect to beam spot, probable charge of the particle and so on.

### 3.3 Primary Vertex

The **c**enter of the coordinate system which is defined as the point where  $p\bar{p}$  collision happens and in principle the primary vertex, from which all objects originate. Its **p**osition changes between events, with a spread of  $40 \mu m$  in the x-y plane ( $\sigma_{xy}$ ) and **28** cm in the z-direction ( $\sigma_z$ ).

**I**dentifying the primary vertexes (PVs) is a two step process, the first primary **v**ertex **f**inder algorithm approximates a position for beam position and PV candidates. For this tracks with dca significance ( $dca/\sigma_{dca}$ ) less than 100 with respect to **d**etector center in  $(r, \phi)$  coordinates are used. The position of the PV is found **i**teratively calculating the fit value until its  $\chi^2$  is less than 10 otherwise removing the **t**rack with the largest contribution. Then other vertex positions are found by the **t**racks not used in the previous steps. Finally, the selection of the hard collision **c**enter from these candidates comes from a  $\log_{10} p_T$  track distribution of Monte

Carlo simulation of minimum bias events<sup>1</sup>. A probability value for every track **in** each vertex is calculated by using this distribution[29]. Then every vertex is **assigned** a probability by multiplying the probabilities of the tracks in them. The **vertex** having the lowest probability is chosen as PV.

### 3.4 Electromagnetic Objects

EM **object** reconstruction starts with a generation of a list of candidate clusters **in the** data produced by EM calorimeters *citation*. They are found with a simple cone **algorithm**. This algorithm starts with sorting all the EM towers<sup>2</sup> and selects the **most** energetic one as the seed tower. If the total transverse energy of the towers **within** a radius of  $r = \Delta R = \sqrt{\Delta\phi^2 + \Delta\eta^2} < 0.2$  is greater than 1.5 GeV ( $E_T > 1.5\text{GeV}$ ), then it is compared against EM variables.

The EM cluster should be isolated which is defined by the  $f_{iso}$  parameter.

$$f_{iso} = \frac{E_{total}(\Delta R = 0.4) - E_{EM}(\Delta R = 0.2)}{E_{EM}(\Delta R = 0.2)} \quad (3.1)$$

Another variable is the em fraction  $f_{EM}$  which is defined as

$$f_{EM} = \frac{E_{EM}(\Delta R = 0.4)}{E_{total}(\Delta R = 0.4)} \quad (3.2)$$

where  $E_{total}$  is the energy in all of the layers and  $E_{EM}$  is the energy in the four EM layers and the first FH layer. The requirement on these variables are  $f_{iso} < 0.2$  and  $f_{EM} > 0.9$ . Clusters passing these two criteria are subjected to search for a **matching** track. For a track to be matched to a cluster the  $\chi^2$  of the fit between

---

<sup>1</sup> A minimum bias event is a soft interaction, so most of the energy in the event is deposited close to the beam pipe, high  $|\eta_D|$ [28].

<sup>2</sup> An EM tower is defined as the four EM layers accompanied by the first FH layer of calorimeters (ECN,CC,ECS) having a cross-sectional area of  $0.1 \times 0.1$  in  $\eta \times \phi$  and originating from the PV.

the track and the EM cluster is determined. It is defined as

$$\chi^2 = \left(\frac{\Delta\phi}{\sigma_{\Delta\phi}}\right)^2 + \left(\frac{\Delta z}{\sigma_{\Delta z}}\right)^2 + \left(\frac{E_T/p_T - 1}{\sigma_{E_T/p_T}}\right)^2 \quad (3.3)$$

where  $\Delta\phi$  and  $\Delta z$  are the azimuthal angle and z position difference between the track and the EM cluster at the third EM layer;  $\sigma_\phi$  and  $\sigma_z$  are the corresponding resolutions. The ratio of  $E_T/p_T$  is the ratio of the transverse energy of EM cluster to transverse momentum of the track. This definition of  $\chi^2$  holds true only for the central calorimeter region, for end-caps the last term is dropped. For a track to match to an EM cluster  $\chi^2$  should be greater than 0.01. A cluster passing the  $f_{iso}$  and the  $f_{em}$  criteria is assigned an EMID of 10 (photon). If it satisfies all of the above conditions then it will be assigned an EMID of -11 for electrons and +11 for positrons.

To diminish contamination from the hadronic decays additional selection cuts can be applied to multivariate quantities such as the H-matrix and the electron likelihood. The H-matrix is a  $\chi^2$  test. It has seven variables:

- the fractions of the energies in the four layers of the EM calorimeter.
- the cluster size in the third layer of EM calorimeter.
- the z position for the PV.
- the logarithm of the cluster energy.

The  $\chi^2$  is calculated from the following equation:

$$\chi^2 = \sum_i \sum_j (x_i - \bar{x}_i)(x_j - \bar{x}_j)H_{ij} \quad (3.4)$$

where  $x_i$  is the values of the  $i^{th}$  variable of EM cluster,  $\bar{x}_i$  is the expected value for that variable from the test beam data and Monte Carlo simulations.  $H_{ij}$  is the

element of the inverse covariance matrix which is calculated from the test beam.

The electron likelihood [26] on the other hand, depends on the following variables:

- the EM fraction,  $f_{EM}$ .
- the H-matrix value.
- the spatial track match  $\chi^2$  probability.
- $\frac{ET}{PT}$  the ratio of the calorimeter cluster energy to its matched track's momentum.
- the distance of closest approach,  $d_0$ .
- the number of tracks in a cone of radius  $r=0.05$  from the associated track, including itself.
- the  $\sum_i p_T^i$  of the tracks in a cone of radius  $r=0.4$  from the associated track, excluding itself.

To calculate the value of the likelihood the following equation is used:

$$L(x) = \frac{P_{sig}(x)}{P_{sig}(x) + P_{bkg}(x)} \quad (3.5)$$

$$P_{sig}(x) = \prod_i P_{sig}(x_i) \quad (3.6)$$

$$P_{bkg}(x) = \prod_i P_{bkg}(x_i) \quad (3.7)$$

where  $x$  is a vector of afore mentioned variables;  $P_{sig}(x_i)$  is the probability of being an electron, assigned to the EM cluster;  $P_{bkg}(x_i)$  is the probability of being anything else, assigned to the EM cluster. These probabilities are obtained from the distributions of the variables entering the likelihood calculation.

### 3.5 Hadronic Objects, Jets

It was mentioned in the first chapter that quarks cannot be observed alone but rather they quickly form bonds with other quarks which are created from the vacuum. This process is known as hadronization. A high energy quark then becomes a jet of hadronic particles, which are referred only as jets. Some of the particles are charged whereas some are not. Thus instead of measuring properties of the quarks coming out of the interaction, one measures these jets' properties. See Figure 3.1

At  $D\bar{D}$  jet reconstructions and hence their measurements are done according to the information collected by the calorimeters. Although there is more than one jet reconstruction algorithms, this analysis uses jets reconstructed with the 'Simple Cone Jet Algorithm', therefore we will only speak about the simple cone algorithm. The following steps are taken in order to reconstruct a jet: formation of jet towers from the calorimeter cells, preclustering of the towers, proto-jet collection of preclusters, finalizing jets by splitting or merging of the proto-jets.

For every cell in the calorimeter, the program called E-scheme calculates the momentum four-vector assuming  $E$  of the cell equals the magnitude of the three-momentum (massless cell assumption). The direction of the momentum is defined from the primary vertex to the centroid of the cell. Then the four-momentum of the tower is calculated by adding four-momenta of all the cells in that tower. Once all the active cells are placed in jets, the list of jets is transferred to the Simple Cone Algorithm.

The Simple Cone Algorithm identifies preclusters from the jet towers as below. It selects the highest  $E_T$  tower as seed and adds to that tower its neighboring tower in  $\Delta R = \sqrt{\Delta\eta^2 + \Delta\phi^2} < 0.3$  one by one starting from the highest  $E_T$  tower, calculating the new center after each addition. When no tower is left, it filters out preclusters with only one tower or with  $p_T < 1$  GeV.

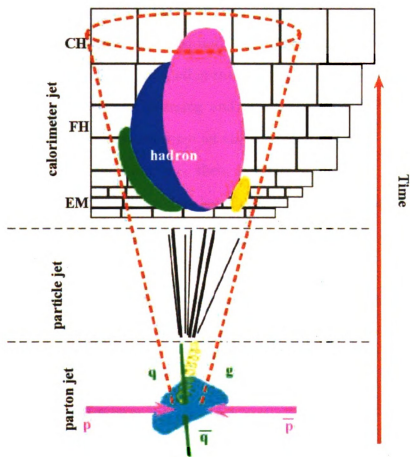


Figure 3.1: The figure showing the development of the jets in the calorimeter, hence the procedure to follow to reconstruct jets based on the information collected by the calorimeter.



Generation of proto-jets is similar to preclustering in the sense that instead of individual towers, preclusters are used. The difference comes from the fact that instead of using  $\eta$  (pseudo rapidity) to measure the distance from the center,  $y$  (rapidity) is used in the  $\Delta R$  calculation. Taking the highest  $p_T$  precluster as the first proto-jet seed, every precluster is consumed within a cone of radius  $r = \Delta R = 0.5$  by combining it with the seed via the E-scheme until the candidate is stable. This procedure is repeated until all the preclusters are used.

The next step is to verify that, all of the proto-jets are unique and none of them are sharing elements by the ‘Merging and Splitting Algorithm’. This algorithm merges two proto-jets if the lower  $p_T$  jet shares more than 50% of its  $p_T$  with the other. The one with the lower  $p_T$ , then, is removed from the jets list. On the other hand if the lower  $p_T$  jet shares less than 50% of its  $p_T$  then the two shared towers are split. The final list is the jets list. They are required to have at least a  $p_T$  of 8.0 GeV.

Once all these steps are taken, quality cuts are applied to separate real jets from fake ones. These requirements are:

- Electromagnetic fraction;  $0.05 < f_{EM} < 0.95$
- Coarse hadronic fraction;  $f_{CH} < 0.4$
- Hot Fraction  $< 10$
- $n_{90} > 1$

The first one of these is to remove electron or photon like objects and against too much hadronic activity. The second removes jets with very high coarse hadronic content. CH layers shouldn’t have too much energy deposition, and they tend to be noisy. The third cut means that the ratio of the energy in the most energetic cell to the energy of the second most energetic cell cannot be more than 10. That is a signature of a read-out problem. The forth one requires that the number of towers

with 90% of the energy of the jet be greater than 1. Besides these requirements, there is one more important cut which is the comparison between the energies of the jets found by the Level1 Trigger System and the DØreco system.

At this point it is said that the jet is reconstructed. However, in order to use these jets in analyses, the energies of the jets are corrected. These corrections account for the noise, calorimeter response, showering effects and the underlying event. This type of correction is termed Jet Energy Scale (JES) corrections. With JES it is aimed to get back the energies of the particles in the jet before they hit the calorimeter. Then

$$E_{JES} = \frac{E_{meas} - O}{R \times S} \quad (3.8)$$

where  $E_{meas}$  is the reconstructed energy,  $O$  is the offset of the energy due to electronic noise, uranium noise, energy pile-up or underlying event,  $R$  is the calorimeter response and  $S$  is the fraction of shower leakage from the cone.

## 3.6 Missing Transverse Energy, MET

Unlike the other particles, neutrinos interact with the matter in very rare occasions. The DØ detector does not detect neutrinos directly. However, the presence of the neutrino in the event manifests itself as an imbalance of the measured transverse energy. The magnitude of MET is the magnitude of the transverse energies of the calorimeter cells and its direction is the opposite in  $\phi$  so that it balances energies in transverse plane.

## 3.7 Muons

Muon system is built to see the path of the particle, hence to measure its momentum. Their reconstruction starts locally in the muon system. The hits in the drift

1  
 2  
 3  
 4  
 5  
 6  
 7  
 8  
 9  
 10  
 11  
 12  
 13  
 14  
 15  
 16  
 17  
 18  
 19  
 20  
 21  
 22  
 23  
 24  
 25  
 26  
 27  
 28  
 29  
 30  
 31  
 32  
 33  
 34  
 35  
 36  
 37  
 38  
 39  
 40  
 41  
 42  
 43  
 44  
 45  
 46  
 47  
 48  
 49  
 50  
 51  
 52  
 53  
 54  
 55  
 56  
 57  
 58  
 59  
 60  
 61  
 62  
 63  
 64  
 65  
 66  
 67  
 68  
 69  
 70  
 71  
 72  
 73  
 74  
 75  
 76  
 77  
 78  
 79  
 80  
 81  
 82  
 83  
 84  
 85  
 86  
 87  
 88  
 89  
 90  
 91  
 92  
 93  
 94  
 95  
 96  
 97  
 98  
 99  
 100  
 101  
 102  
 103  
 104  
 105  
 106  
 107  
 108  
 109  
 110  
 111  
 112  
 113  
 114  
 115  
 116  
 117  
 118  
 119  
 120  
 121  
 122  
 123  
 124  
 125  
 126  
 127  
 128  
 129  
 130  
 131  
 132  
 133  
 134  
 135  
 136  
 137  
 138  
 139  
 140  
 141  
 142  
 143  
 144  
 145  
 146  
 147  
 148  
 149  
 150  
 151  
 152  
 153  
 154  
 155  
 156  
 157  
 158  
 159  
 160  
 161  
 162  
 163  
 164  
 165  
 166  
 167  
 168  
 169  
 170  
 171  
 172  
 173  
 174  
 175  
 176  
 177  
 178  
 179  
 180  
 181  
 182  
 183  
 184  
 185  
 186  
 187  
 188  
 189  
 190  
 191  
 192  
 193  
 194  
 195  
 196  
 197  
 198  
 199  
 200  
 201  
 202  
 203  
 204  
 205  
 206  
 207  
 208  
 209  
 210  
 211  
 212  
 213  
 214  
 215  
 216  
 217  
 218  
 219  
 220  
 221  
 222  
 223  
 224  
 225  
 226  
 227  
 228  
 229  
 230  
 231  
 232  
 233  
 234  
 235  
 236  
 237  
 238  
 239  
 240  
 241  
 242  
 243  
 244  
 245  
 246  
 247  
 248  
 249  
 250  
 251  
 252  
 253  
 254  
 255  
 256  
 257  
 258  
 259  
 260  
 261  
 262  
 263  
 264  
 265  
 266  
 267  
 268  
 269  
 270  
 271  
 272  
 273  
 274  
 275  
 276  
 277  
 278  
 279  
 280  
 281  
 282  
 283  
 284  
 285  
 286  
 287  
 288  
 289  
 290  
 291  
 292  
 293  
 294  
 295  
 296  
 297  
 298  
 299  
 300  
 301  
 302  
 303  
 304  
 305  
 306  
 307  
 308  
 309  
 310  
 311  
 312  
 313  
 314  
 315  
 316  
 317  
 318  
 319  
 320  
 321  
 322  
 323  
 324  
 325  
 326  
 327  
 328  
 329  
 330  
 331  
 332  
 333  
 334  
 335  
 336  
 337  
 338  
 339  
 340  
 341  
 342  
 343  
 344  
 345  
 346  
 347  
 348  
 349  
 350  
 351  
 352  
 353  
 354  
 355  
 356  
 357  
 358  
 359  
 360  
 361  
 362  
 363  
 364  
 365  
 366  
 367  
 368  
 369  
 370  
 371  
 372  
 373  
 374  
 375  
 376  
 377  
 378  
 379  
 380  
 381  
 382  
 383  
 384  
 385  
 386  
 387  
 388  
 389  
 390  
 391  
 392  
 393  
 394  
 395  
 396  
 397  
 398  
 399  
 400  
 401  
 402  
 403  
 404  
 405  
 406  
 407  
 408  
 409  
 410  
 411  
 412  
 413  
 414  
 415  
 416  
 417  
 418  
 419  
 420  
 421  
 422  
 423  
 424  
 425  
 426  
 427  
 428  
 429  
 430  
 431  
 432  
 433  
 434  
 435  
 436  
 437  
 438  
 439  
 440  
 441  
 442  
 443  
 444  
 445  
 446  
 447  
 448  
 449  
 450  
 451  
 452  
 453  
 454  
 455  
 456  
 457  
 458  
 459  
 460  
 461  
 462  
 463  
 464  
 465  
 466  
 467  
 468  
 469  
 470  
 471  
 472  
 473  
 474  
 475  
 476  
 477  
 478  
 479  
 480  
 481  
 482  
 483  
 484  
 485  
 486  
 487  
 488  
 489  
 490  
 491  
 492  
 493  
 494  
 495  
 496  
 497  
 498  
 499  
 500  
 501  
 502  
 503  
 504  
 505  
 506  
 507  
 508  
 509  
 510  
 511  
 512  
 513  
 514  
 515  
 516  
 517  
 518  
 519  
 520  
 521  
 522  
 523  
 524  
 525

chambers of the three layers are used to make local track segments in the muon system. Hits from the scintillators are matched to the track segments. With the help of the toroid it is possible to make a local transverse momentum  $p_T$  measurement by measuring the deflection on the path of the muons, see Figure 3.2. The resolution and the precision of this measurement is increased by matching these tracks to the ones reconstructed by central tracking system.

The muon reconstruction algorithm starts building the tracks based on the drift chamber hits in individual layers of detectors. This process considers only one  $\phi$  octant at a time. The algorithm requires some restrictions on the track segments developed from the pairs of wire hits: i) no hit can lie on the same drift circle ii) the separation of the hits along the y axis should be less than 20 cm iii) hits should be on different wire planes unless they are from different neighboring wires. These can be more easily visualised by looking at the Figure 3.3. Track segment candidates are compared and connected together if they are compatible. The scintillator hits are used to refine the timing of the hits, the tracks are fitted to a line. The tracks with lowest  $\chi^2/N_{hits}$  are kept for each layer of an octant. This process is repeated for every octant. Afterwards a search for a possible track match in the central tracking system is done.

Depending on the number of hits a muon can have different quality which can be tight, medium or loose. These qualities are based on the local muon information.

For a muon to be tight, it should have both A and B+C layer segments, at least two wire hits and at least one scintillator hit in the A layer, at least three wire hits and at least one scintillator hit in the B+C layers and the fit between A and B+C layers should converge.

For a muon to be medium, there are a few different possible scenarios depending on the number of layers a muon has a hit. It is an 'nseg3' (number of layers in the muon detector that are hit by this muon) medium if it has at least two wire

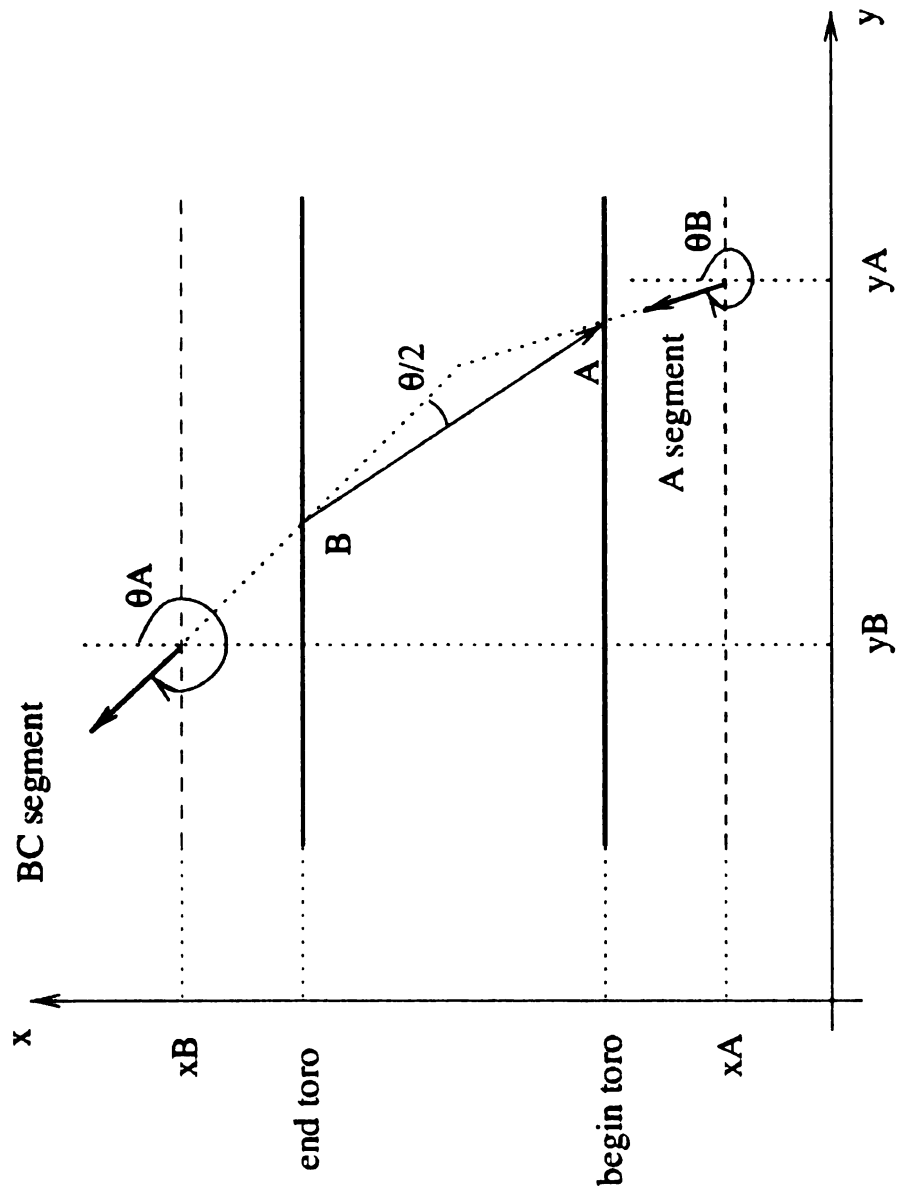


Figure 3.2: Figure showing the calculation of the momentum of the muon locally by the muon detector. The toroid affects the path of the muon passing through it by deflecting it by certain angle which depends on the charge and the momentum of the muon. The magnetic field in the toroid is a known parameter of the calculation.



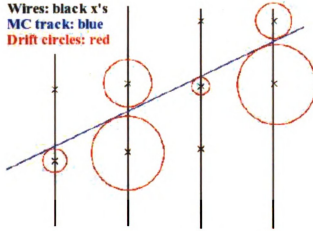


Figure 3.3: Figure showing construction of a muon track segment in drift tubes. The drift wires are perpendicular to the plane defined by the paper. Blue line is the constructed muon path according to the drift circles which are shown in red.

hits and one scintillator hit in the A layer, at least two wire hits and either one scintillator hit in the B+C layers or a central track is matched to it with less than four hits in B+C layers. The muon is an 'nseg2' medium if it has two wire hits and one scintillator hit in the B+C layers with a central track match. The muon is an 'nseg1' medium if it has at least two wire hits and one scintillator hit in the A layer with a central track match.

By dropping one of the requirements on the different type of medium muons, one can get loose muon definitions.

Matching is done between a muon track in the muon detector and a central track with at least  $p_T > 1$  GeV, if they are within  $|\Delta\eta| < 1$  and  $|\Delta\phi| < 1$  of each other. The track must have a  $\chi^2 \times d.o.f < 1000$ . In the calculation of  $\chi^2$  the position and momentum measurements are used. [27]

# Chapter 4

## Data Samples

*“ ‘I had’ said he, ‘come to an entirely  
erroneous conclusion which shows,  
my dear Watson, how dangerous it always is  
to reason from insufficient data.’ ”[41]  
Sir Arthur Conan Doyle*

As mentioned in the previous chapters, it is virtually impossible to analyze all the collisions happening in the detectors. Depending on the signature of the process for which one looks, most of the time, it is unnecessary to analyze all the recorded events as well. This chapter talks about data sets that are used in this analysis and the quality requirements by which they are bound to produce a scientific and unbiased result.

### 4.1 Data Set

This analysis uses data collected during the 2002-2006 physics runs. The versions of DØreco to reconstruct the events in these runs are p17.09.03 and p17.09.06. The term to refer to data just after reconstruction is ‘raw data’. The raw data from this period was further processed by DØCORRECT in order to make corrections on the properties of the physics objects such as EM, muon, jets and missing  $E_T$ .





The Common Samples Group (CSG) established in DØ is responsible for providing analyzers with pre-processed data in order to . Pre-processed here only means that a very first selection based on very loose criteria is done. For this analysis the following data sets are used:

- CSG\_CAF\_2EMhighpt\_PASS3\_p17.09.03
- CSG\_CAF\_2EMhighpt\_PASS3\_p17.09.06
- CSG\_CAF\_2EMhighpt\_PASS3\_p17.09.06b
- CSG\_CAF\_2MUhighpt\_PASS3\_p17.09.03
- CSG\_CAF\_2MUhighpt\_PASS3\_p17.09.06
- CSG\_CAF\_2MUhighpt\_PASS3\_p17.09.06b

These samples are CAF trees<sup>1</sup> produced by the Common Samples Group with the p17.09.03 or p17.09.06 DØreco versions. They were created by selecting 2 high  $p_T$  leptons from all the data collected during RunIIa with the following requirements. For the EM case there should be two simple cone objects with an EM ID of 10 (identification number for photon) or  $\pm 11$  (identification number for electron '-' or positron '+') having a  $p_T$  greater than 12 GeV. For the MU case however, there should be two 'Loose' muon objects with central tracks having at least a  $p_T$  of 10 GeV. Producing these data sets beforehand helps analyzers by reducing the time of running analysis code on the whole data.

Moreover the same data sets are used when measuring the QCD background, which will be discussed in more detail in the next chapter. The reason for using the same set is to avoid any biases.

---

<sup>1</sup>CAF trees are ROOT trees (a data format readable by ROOT) specialized to keep information about a collision event created by Common Samples Group (CSG).

1.0

1.2

1.4

1.6

1.8

2.0

2.2

2.4

2.6

2.8

3.0

3.2

3.4

3.6

3.8

4.0

4.2

4.4

4.6

4.8

5.0

5.2

5.4

5.6

5.8

6.0

6.2

6.4

## 4.2 Data Quality

Although constant emphasis is put on and much care is given to the quality of the data written to tape, complexity and the immensity of the system produces occasional hiccups under such as a failing power supply or unreliable read-out channel and so on. An analysis should be free of any of the problematic events in order to secure its results' reliability. For this reason there are several restraints placed on the states in which an event can be. The first one of these is the run to which this event belongs should be declared by the Data Quality Group as 'good' which means that for EM channels the SMT quality tag, CFT quality tag should be 'REASONABLE' or better and calorimeter quality tag should be 'UNKNOWN' or better; for MU channels SMT quality tag, CFT quality tag, MUON quality tag should be 'REASONABLE' or better and calorimeter quality tag should be 'UNKNOWN' or better.

Bad luminosity blocks<sup>2</sup> are also removed. Events with unphysical activity in the calorimeter for example 'ring of fire' or 'hot cells' are also removed by removing their corresponding luminosity blocks.

After removing all the bad quality events, it is possible to measure the luminosity of the data. As mentioned before in chapter 2, luminosity is a measure of how much data is collected. Nevertheless a trigger system is in place before even checking if the states of the detector components are fine, which weaves complexity into the calculation of luminosity. For the total luminosities of different luminosity epochs please see Tables 4.1, 4.2. An irreducible uncertainty of 6.5% is attached to all of these numbers.

---

<sup>2</sup>luminosity block refers to a data collection period which is about 1 minute

Trigger Version	Run Ranges	Luminosity ( $pb^{-1}$ )
$v8 - v11$	160582 – 178721	$118 \pm 8$
$v12$	178722 – 194566	$239 \pm 15$
$v13$	194567 – 208203	$375 \pm 24$
$v14$	208204 – 215670	$337 \pm 22$
$v8 - v14$	160582 – 215670	$1068 \pm 69$

Table 4.1: The integrated luminosity of the RunIIa period is shown in this table for the 2EMHighPt data sample. The run ranges include test runs also but those runs **are** not included in the luminosity calculation as well as those runs that are **excluded** due to bad data quality tags. An uncertainty of 6.5% is associated to the **luminosity** result, because of the way luminosities are measured at DØ.

Trigger Version	Run Ranges	Luminosity ( $pb^{-1}$ )
$v8 - v11$	160582 – 177283	$52 \pm 3$
$v12$	177284 – 194566	$248 \pm 16$
$v13$	194567 – 208203	$342 \pm 22$
$v14$	208204 – 215670	$292 \pm 19$
$v8 - v14$	160582 – 215670	$944 \pm 61$

Table 4.2: The integrated luminosity of the RunIIa period is shown in this table for the 2MUhighpt data sample. The run ranges include test runs also but those runs are **not** included in the luminosity calculation as well as those runs that are **excluded** due to bad data quality tags. An uncertainty of 6.5% is associated to the **luminosity** result, because of the way luminosities are measured at DØ.

## 4.3 Monte Carlo

*All* of the measurements are done on the data collected by the DØ detector. However **not** only to test the theory, but also to understand the detector response more *deeply*, one essentially needs a way of simulating high energy collisions. This is *achieved* through simulations of collisions and simulations of detector measurements of those events. The collection of them is referred to Monte Carlo events.

**The** DØ detector is modelled by a program named GEANT which has all the structural information about the detector so that it can incorporate all the effects of detector material (instrumented or uninstrumented) and the magnetic fields in the **bulk** of the detector. This program models the ionization and the secondary particle generations, as the particles move through the detector.

For this analysis the generation of the events the Pythia and AlpGen event generation programs are used. The parton distribution function used in the generation process is CTEQ6L1. If an event is generated by AlpGen, it is further processed by Pythia to add the effects of parton showering and hadronization to it.

To better approach and represent the real collision events, these Monte Carlo events **are** laid over min-bias<sup>3</sup> events. The program responsible for merging min-bias events with hard scatter events is called DØsim.

All **the** Monte Carlo generated events are required to pass all the above mentioned **data** quality requirements.

---

<sup>3</sup>A **minimum** bias event is a soft interaction, so most of the energy in the event is deposited **close** to the beam pipe, high  $|\eta_D|$ [28].

# Chapter 5

## Cross Section Measurement

*“Haste still pays haste, and leisure answers leisure,  
Like doth quit like, and measure still for measure.”[42]*  
Shakespeare

In this chapter a cross section measurement for the process  $WZ(ZZ) \rightarrow 2j + 2l$  is explained.

### 5.1 Introduction

W and Z bosons can decay into both leptons and quarks, which eventually form jets of hadrons. We are interested in events where a Z boson decays to leptons and a W boson decays to hadrons. The mass of the W is 80.41 GeV and the mass of the Z boson is 91.19 GeV. The energy resolution of the DØ calorimeter for the jets is insufficient to distinguish a W decaying to jets<sup>1</sup> from a Z boson decaying to jets, since the uncertainty of the measurement (12.65 GeV) is greater than the mass difference of the bosons. Therefore it is practically impossible for us to distinguish Z and W bosons in the case where both of them decays to jets. This led us to choose our analysis chain as being WZ and ZZ events producing two

---

<sup>1</sup>Due to hadronization of the quarks as mentioned above

leptons and two jets. From now on whenever ‘signal’ is mentioned, it is expected to be understood as both kind of interactions.

## 5.2 Objects Identification

*In order* to centralize common tasks that are performed in every physics analysis, *such as* finding objects in a consistent manner and applying similar cuts in a *consistent* manner, a framework is established and it is called Comman Analysis **Format** Environment (CAFé). The code for this analysis (WZ/ZZ cross section *measurement*) is also a small part in the framework and utilizes the components of the **framework**.

**This** analysis has a real Z decaying to leptons, therefore, it starts with identifying a **Z** in the event, which is a relatively easy step. It consists of finding at least two **leptons** consistent with decay products of a Z boson. Then it is required that the **event** should have at least one jet excluding many events that have no interest to our **final** state while keeping enough of them for the multivariate technique to work.

### 5.2.1 Lepton Identification: Electrons

There **are** several different electron definitions within DØ. Depending on the need of the **analysis**, one can select the electron type that best suits one’s analysis. The **definitions** differ only in the quality cuts. In this analysis, *Loose\_trk* type of **electrons** are used. The following conditions must be met by EM objects to qualify as a **Loose\_trk** electron. The object should have

- **EM** ID = 10 or  $\pm 11$
- **Calorimeter** isolation  $f_{iso}$   

$$f_{iso} = \frac{E_{tot}(0.4) - E_{em}(0.2)}{E_{em}(0.2)} < 0.2$$



- EM fraction  $f_{em}$

$$f_{em} = \frac{E_{em}(0.4)}{E_{total}(0.4)} > 0.9$$

- electron likelihood<sup>2</sup>

$$likelihood_{em} > 0.2$$

- the transverse momentum of the electron  $p_T > 3 \text{ GeV}$

This concludes the definition of Loose\_trk electrons. Any object passing these requirements will be named as being at least a Loose\_trk electron. However, because electrons are decaying from a very heavy particle –Z boson–, they are expected to have high transverse momentum. Due to this fact, the  $p_T$  requirement on the electrons are tightened by incrementing it to 15 GeV.

The region between the Central Calorimeter (CC) and the Endcap Calorimeters (ECs) –the inter cryostat region (ICR)– is not instrumented as well as the other regions. This results in very poor resolution for that region. Because of this, electrons that are in the ICR are not used, and electron detector eta coverage is limited to include only  $|\eta_D| < 1.1$  and  $1.5 < |\eta_D| < 2.5$  regions with the full  $\phi$  range. Since the ultimate goal in identifying the leptons is to reconstruct a Z boson, it is necessary that the event have at least two electrons of the same quality.

## 5.2.2 Lepton Identification: Muons

As in the case of electrons, muons have several different definitions depending on the need of the analysis. The definitions of muons differ in the number of hits in the chambers and tracking system. Different analysis use different definitions.

The definition of a muon includes three quantities: its quality from the local muon system (muon detector), its track quality from the central tracking system, and its isolation quality from both tracking system and the calorimeter. This anal-

---

<sup>2</sup>as defined in the third chapter

ysis uses *Medium* quality muons<sup>3</sup>, having a matching central track with medium quality and NPThight isolation (tight definition made by New Phenomena group meeting their requirements). All these definitions are done centrally by the object-*id* groups to be used by analyzers and can be found in muon ID note [27] but a *summary* will be given here for convenience.

**The** quality of the muon object depends on the number of hits it leaves behind in the muon system. The *nseg* quantity gives the number of layers hit in the muon detector. This quantity is negated if no track is found in the tracking matching to the object. Against cosmic muon radiation there is a cosmic veto flag which depends on the time difference between the scintillator hits of the track and the event timing. The difference should be less than 10 ns otherwise the muon is accepted as a cosmic ray. The distance of closest approach (dca) of the muon should be less than 0.02 mm or 0.2 mm depending on whether its track has an SMT hit or not respectively. The tracker part of the isolation requires that the  $p_T$  sum of all of the tracks sharing the same vertex with the muon in a cone of radius of 0.5 be less than 2.5 GeV. The calorimeter part, on the other hand, necessitates that the energy sum of all the cells in a hollow cone defined by radii of 0.4 and 0.2 around the muon track be less than 2.5 GeV. To summarize all of them a muon

- having a medium quality with an ‘nseg’ parameter of  $nseg > 0$
- being inconsistent with a cosmic muon
- having an associated track with a dca parameter of  $|dca| < 0.02$  with SMT hits and  $|dca| < 0.2$  without SMT hits
- having a spatial track match of  $\chi^2/d.o.f \leq 4$
- being isolated in the tracker by  $\sum_{tracks} p_T(R < 0.5) < 2.5$  GeV and in the calorimeter by  $\sum_{cells} E_{T_{cell}}(0.2 < R < 0.4) < 2.5$  GeV

---

<sup>3</sup>for more explanations see chapter 3

Since the ultimate goal in identifying the leptons is to reconstruct a Z boson, it is necessary that the event have at least two muons of the same quality.

### 5.2.3 Jet Identification

Since this analysis searches for an event signature that has at least two leptons and two jets; as a preliminary selection criteria at least the presence of one jet is imposed on the events. The jet algorithm used in DØ is the simple cone jet algorithm. For this analysis, the construction of the jets is done as explained in Chapter 4 with a radius of  $\Delta R = 0.5$ . The name of the algorithm type of jets is “JCCB”. For this analysis, at the preselection level there should be at least one good jet with the following properties<sup>4</sup>:

- the electromagnetic energy fraction<sup>5</sup> of the jet ( $f_{em}$ ) should be in the range  $0.05 < f_{em} < 0.95$
- the coarse hadronic energy fraction of the jet ( $f_{ch}$ ) should be  $f_{ch} < 0.40$
- the Level-1 trigger system should confirm the presence of the jet
- the detector eta ( $\eta_D$ ) position of the jets should be  $\eta_D < 2.5$ .

As with the leptons, the jets (or more appropriately quarks) are coming from heavy particles (either a W boson or a Z boson), they are expected to carry high transverse momentum, given the fact that bosons are more or less created motionless. Because of this, at the pre-selection stage events are required to have at least one good jet with  $p_T > 20$  GeV.

The main reason for having a cut at  $p_T > 20$  GeV stems from the following reason: In order for us to make a healthy comparison between Monte Carlo events

---

<sup>4</sup>The cuts listed here are generalized for the convenience of the reader. For more rigorous and accurate cuts the reader should refer to [30]

<sup>5</sup>its definition is given above

and data events another set of corrections is done on Monte Carlo events. Those are the re-weighting of the event with respect to the transverse momentum of the  $Z$  boson (*ZPtReweighting*) and the number of jets in the event. There are actually *three* ZPtReweighting procedures changing according to the complexity of the final *particles* in the events. If one is only interested in the inclusive production of  $Z$  *particles*, then it is not necessary to implement a re-weighting with respect to the **number** of jets in the events, since the sheer number of  $Z$  events in the ‘zero’ jet bin **would** drown all the others. The second one is optimized for the previous run **period** (p14 version of the DØreco), which is old and cannot produce correct **results** as there are many changes to the reconstruction of the objects. The third has **two** branches depending on the Monte Carlo event generator, ALPGEN or PYTHIA. Both of these branches implement the re-weighting both with respect to the **number** of jets or without considering the number of jets in the event giving an **average** correction over the jet multiplicity. Since eventually the event selection will **include** at least two jets, this analysis uses ZPtReweighting with jet multiplicity folded **in** for the PYTHIA generator. As its name suggests, the event should have a  $Z$  boson generated. Although the signal (as mentioned earlier, WZ and ZZ events) has **also** at least one  $Z$  boson in it, this re-weighting is not applied to signal events.

The **measurement** of the energies of the jets is affected by several factors as will be **explained** and it is essential to know the energy carried away by the particle jets to **make** an accurate measurement. The Jet Energy Scale (JES) is the bridge to reach **from** measured jet energy  $E_{jet}^{meas}$  to the particle jet energy  $E_{jet}^{ptcl}$ . The relation **between** the two is

$$E_{jet}^{ptcl} = \frac{E_{jet}^{meas} - E_0}{R_{jet} S_{jet}} \quad (5.1)$$

where:

- Offset Energy  $E_0$ :

is defined as the energy that is not associated with the hard scattering. The noise from the decay of the uranium absorber, the noise from the electronics, additional  $p\bar{p}$  events (underlying events) and the additional energy from the previous crossings (pile-up) are the causes of the presence of an offset in energy. To determine this contribution minimum bias events, events containing no hard interaction, are used.

- Calorimeter Response  $R_{jet}$ :

is the energy response of the calorimeter to particle jets. Jets are made up of different kind of particles, which get different response from the calorimeter. This number is smaller than unity due to energy lost before the calorimeter, uninstrumented regions between the calorimeter modules and lower response of the calorimeter to hadrons as compared to electrons and photons. The inhomogeneities between the modules contributes as well. The calorimeter response depends on the jet energy and the detector eta ( $\eta_D$ ). The radius of the cone of the jet also affects it, since the particles near the center of the cone have higher energies and therefore higher response.  $R_{jet}$  is measured from the  $p_T$  imbalance in the back-to-back  $\gamma + jets$  events making use of the electromagnetic energy scale for photon since it is known to a high accuracy from  $Z \rightarrow ee$  events.

- Showering Correction  $S_{jet}$ :

is the correction factor due to the inability to include only particles radiated from the hard scatter and to exclude all else. Because of the energy deposited outside of the jet cone from the run-away particles of the jet and the energy included from the particles that don't belong to the jet. Usually it is smaller than unity and depends on the cone size of the jet and the detector eta. This quantity is measured from the jet energy profiles.

1.1

1.2

1.3

1.4

1.5

1.6

1.7

1.8

1.9

1.10

1.11

1.12

1.13

1.14

1.15

1.16

1.17

1.18

1.19

1.20

1.21

1.22

1.23

1.24

1.25

1.26

1.27

1.28

1.29

1.30

The total uncertainty of the JES contains systematical and statistical uncertainties from both data and Monte Carlo. [31, 32, 33]

After the hadronization step and processing the events with the detector simulation, the Monte Carlo events have to go through jet corrections in order to replicate ‘real data’. Jet Shifting, Smearing and Removal (JSSR) [34, 35] is the one that comes after JES. The purpose of JSSR is to correct Monte Carlo events in three classes: i) differences in the reconstruction and identification efficiency ii) energy resolution iii) calorimeter responses. The corrections are calculated using  $\gamma + jets$  and  $Z + jets$  events and provided to analyses by the JES Group.

The measurements for the inter-cryostat region (ICR) are deemed unreliable. If a selected jet’s position is in the ICR than that event is completely ignored. Less than 0.05% of the events are rejected due to this requirement.

EM objects are usually reconstructed as jets with small radius of cone. The list of EM objects and the list of jet objects are separate entities in the event. This has a significant effect on event selection. One may find events where a jet is actually an electron. This led us to correct our list of jets by comparing the locations of EM objects and the locations of jet objects in the calorimeter. If an overlap occurs between the two lists, the jet is removed from the good jets list. Double counting of an em object as a jet is prevented this way.

#### 5.2.4 Missing Transverse Energy, MET

In previous chapters, we mentioned that properties of neutrinos cannot be measured directly. They are rather identified indirectly as a transverse momentum imbalance. By using momentum conservation in the transverse plane with respect to the z-axis (beam pipe), and using every active cell in the calorimeter it is possible to measure its transverse momentum. The transverse momentum of the neutrino, then corresponds to the missing transverse energy in the event; because

the transverse momentum carried away must be zero and neutrinos do not interact with matter.

$$\overrightarrow{MET} = - \sum_{visible} \overrightarrow{E_T} \quad (5.2)$$

One problem of calculating MET indirectly is that even when neutrinos are not present in the event, limited detector resolution may lead to calculate a finite MET (fake). Another problem is that, there is no way of knowing how many neutrino particles were in the event, since we could only see the vector sum of their transverse momenta.

Because MET is derived from other quantities, the corrections made on them such as JES corrections or EM scale corrections should be reflected on MET as well. Furthermore, if an event contains a muon which interacts with the calorimeter minimally, one has to correct the value of MET with respect to transverse momentum of the muon in the event.

Therefore, the final MET value includes summation of positive energy deposits (raw energies), EM scale, JES and muon corrections; see below.

$$MET^{corr} = \sqrt{MET_x^2 + MET_y^2} + \Delta_{EM} + \Delta_{JES} + \Delta_{\mu} \quad (5.3)$$

The final states of the signals do not include any neutrino. This actually gives a good handle on the events against backgrounds including a neutrino in the event. We will employ this fact to reduce  $t\bar{t}$  events in the final selection.

### 5.2.5 Other Objects Identifications

The distribution of the z-coordinate of the primary vertex has a Gaussian shape with a spread of approximately 30 cm. Therefore, it is required that the z position of the reconstructed primary vertex of the event should fall between  $\pm 60$  cm of



the detector center. Having a jet and at least two charged leptons is translated as a requirement of the number of tracks coming from the primary vertex. If the number of tracks coming out of it is less than three the event is not accepted.

In a channel it is very unlikely to have another isolated high pt lepton of another kind. This is dictated by the final state of the processes. Thus a veto mechanism is active in the selection process which prevents events with two selected electrons and a high  $p_T$  isolated muon or vice versa.

### 5.2.6 Constructing the Vector Boson: Z Boson

The reconstruction of the Z boson is a two step process. The first is the selection of leptons. If an event has at least two good quality leptons, it is considered for having a Z candidate in it. The second step is the actual reconstruction of a new object from the two leptons in the event and comparison of the new object's properties with the Z boson's properties. One question that comes to mind is how to select two leptons if more than two leptons are found in the event. The answer for this question is the combination that has the closest invariant mass to 91.19 GeV (Z mass). Thus every combination is considered as a candidate.

For further selections we consider an invariant mass cut around 91 GeV, and the points from where the leptons radiate out. As it is evident from the figures 5.1 and 5.2 there are slight changes in the observation of the Z boson. Therefore the selection criteria shows little differences between the two channels.

For the **electron channel**, the mass window for Z candidates is set to be  $70 < M_Z < 110$  GeV. As can be seen from the Figure 5.1 this cut doesn't compromise our acceptance. Besides the mass cut on the Z candidate, it should have originated within the probable spread of the primary interaction point. Moreover, since Z particles decay almost instantaneously, the calculated primary interaction point for the event should be within the 3 cm distance of the extrapolated position of

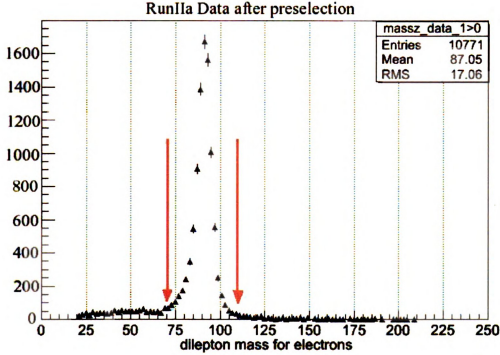


Figure 5.1: Di-electron mass distribution for the RunIIa Data set after preselection. All the events contributing to this histogram have two good quality electrons with  $p_T > 15$  GeV and one good quality jet with  $p_T > 20$  GeV

the Z particle.

For the **muon channel**, the mass window cut for Z candidates is larger than the one for electron channel,  $50 < M_Z < 130$  GeV due to the fact that the muon detector resolution is not as good as the calorimeter resolution for electrons. As can be seen from the Figure 5.2 this cut, although allowing more backgrounds than the one on the electron channel, still does a very good job. Besides the mass cut on the Z candidate, it should have originated within the probable spread of the primary interaction point. By the same reasoning as the electron channel, the calculated primary interaction point of the event should be within the 3 cm distance of the extrapolated position of the Z particle.

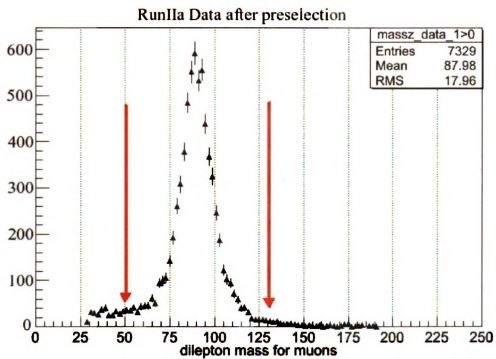


Figure 5.2: Di-muon mass distribution for RunIIa Data set after preselection. All the events contributing to this histogram have two good quality muons with  $p_T > 15$  GeV and one good quality jet with  $p_T > 20$  GeV

### 5.2.7 Object Identification Efficiencies

Due to the difference observed in the reconstruction and identification efficiencies between the Monte Carlo events and the data, correction factors are applied to the Monte Carlo events. They are all referred here as object identification efficiencies.

#### Electron Efficiency

The efficiencies of selecting a single electron with given properties are determined by the EM ID group [36]. The group uses a method named *tag-and-probe* [37, 38] on a pure sample of  $Z \rightarrow ee$  events. In the tag and probe method a tag electron is first selected by a very tight cut:

- $EMID = 10$  or  $\pm 11$ ,
- $f_{iso} < 0.2$ ,
- $f_{em} > 0.9$ ,
- either  $\eta_D < 1.1$  and  $\chi^2_{HMx7} < 12$ , or  $1.5 < \eta_D < 2.5$  and  $\chi^2_{HMx8} < 20$ ,
- $E_T > 25 GeV$ ,
- a track matched to EM object with  $E/p > 1$  and number of SMT hits  $> 0$ ,
- the trigger object matched to EM object.

The remaining electron (probe) should pass the cuts. The efficiency is the ratio of the number of events with a passing electron(A) to the total number of events(T).

$$\epsilon = \frac{A}{T} \tag{5.4}$$

If there is more than one electron qualifying as a tag electron in an event, then that event is used for both electrons being as tag electrons. The efficiency is

parametrized with respect to  $\eta_D$  and  $\phi_D$ . This is done both on data and Monte Carlo (PYTHIA generated) events. Comparison of the two gives the correction factors that should be applied on the Monte Carlo events. Thus after making the corrections Monte Carlo events look more like real data. The efficiency is close to 90% in the central calorimeter (CC) and goes down to around 50% in the endcap calorimeters (EC). There is also a dependency on the  $\eta$  value, and this dependence is also taken into account. The correction factors are applied in the same way through all the analyses: First an analyst applies the pre-selection efficiencies to the selected events, afterwards the electron type efficiencies are applied by use of '.spc' files, which keep binned efficiency factors with respect to different parameters like  $\eta$  or  $\phi$ .

### **Muon Efficiency**

The efficiencies of selecting a single muon with given properties are determined by the Muon ID group [27]. This group also uses the same method *tag-and-probe* method to measure muon identification efficiencies. Similarly, they use a sample of pure  $Z \rightarrow \mu\mu$  events. The procedure for calculating efficiencies is the same as explained above. Muon ID efficiencies include, muon identification in the muon detector, track efficiencies and isolation efficiencies.

### **Jet Efficiency**

The efficiencies of identifying and selecting jets with predetermined properties are measured by the Jet-ID group [38, 39]. The efficiencies are provided collaboration-wide by Jet-ID group to account for the inefficiencies when selecting jets in the prescribed fashion. In order to be free of any trigger biases on the probe object the tag jet is required to be capable of firing the level-1 level-2 and level-3 terms of the trigger. This is done by matching the jet with the triggering object. The two

efficiencies can be summed up as reconstruction efficiencies and jet-id efficiencies. For the calculation of the jet-ID efficiencies, a pure sample of back-to-back dijet events which have an MET less than 40 GeV are used. The former is the fraction of calorimeter jets in the probe region ( $\Delta\phi_{tag, probe} > 3.0$ ) and the latter is the fraction of the jets passing jet-id cuts in the same region. The jet-id efficiencies are very high, in the vicinity of 99%. The application of the efficiencies to correct Monte Carlo events is done through the application of efficiency factors by loading '.spc' files. The efficiencies are parametrized in detector eta ( $\eta_D$ ) and transverse momentum of the jet ( $p_T^{jet}$ ).

### 5.2.8 Trigger Efficiency

For any event to be recorded, it has to pass trigger requirements. As shown in the Figure 5.3 unless the triggered object falls on the plateau region, there is an inefficiency associated with the triggers. To better replicate the effects of imperfect measuring media Monte Carlo events are weighted so that the trigger turn on curve is reproduced.

For this analysis, instead of selecting some triggers, we employed a newly developed procedure: Trigger Super OR'ing. It can be explained as follows. This analysis requires that there should be at least two charged leptons and two jets. Depending on this final state, one can choose to select events with “di-lepton triggers”, “single-lepton triggers”, “lepton+jets triggers” or “jet triggers”. It is not wise to use just the last element of this set. Instead of selecting one element from the set the union of the elements are used. For this single-lepton triggers are combined with lepton+jets triggers. If an event fires any of the unprescaled triggers from single-lepton or lepton+jets triggers it is accepted. This way the trigger acceptance and efficiency is increased. This gives a correction factor for the Monte Carlo events on the order of 99%.

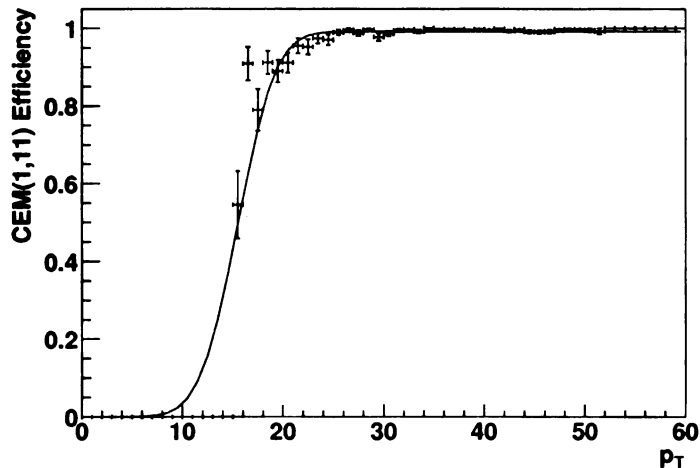


Figure 5.3: Figure show a typical trigger turn on curve. This is produced by using the CEM(1,11) trigger. It requires an electron with a transverse momentum of 11 GeV in the event. As it is seen from the figure selecting with this trigger is not quite efficient unless the object has at least 20 GeV transverse momentum.

### 5.3 Backgrounds

Even though this term has been used in this study, it hasn't been properly introduced to the reader. In the dictionary it is defined as “the totality of effects that tend to obscure a phenomenon under investigation and above which the phenomenon must be detected” [40]. If we adapt this definition to this analysis, ‘every interaction that produces the same final state particles, yet different from the physics that is sought after’. Then any interaction that produces two leptons and two jets other than WZ or ZZ events comprise the background for the WZ/ZZ productions. Those are

- *jet final states*
- *top quark and anti-top quark production*
- *Z+jets*

### 5.3.1 *jet* Backgrounds

This type of background is due to misidentification. One or both of the leptons ( $e, \mu$ ) are actually jet objects that are faking  $e$  or  $\mu$ . The origin of the jets may be anything, a genuine jet coming from the hard scatter or a low energy jet or else an instrumental hiccup making a jet appear as a lepton.

We make an estimation of the degree to which this analysis is susceptible to jet background. The main feature of the estimation is a ratio test. The signal region is two jets with a Z boson having a mass in the mass window range<sup>6</sup>. We assume that outside of the mass window the number of signal events is negligibly small.

The di-lepton mass spectrum includes a Z mass peak at around 91 GeV laid on top of continuous spectrum of Drell-Yan events. Drell-Yan events can be simulated but jet events may not. The presence of the Z peak in the mass spectrum wouldn't change the shape of the Drell-Yan mass spectrum. Since jet events are due to instrumental deficiency we can safely assume that at every mass interval those events behave similar to Drell-Yan events. Because the number of Drell-Yan events is several order larger than jet events, the shape of the distribution doesn't change anyway. Then it can be concluded that if one calculates the number of jet events outside of the Z mass window, by extrapolation it should be fairly straightforward to estimate the number of events inside the window.

For the purpose of counting the number of possible jet events, one changes the selection criteria of the leptons. The final state contains two leptons which means that either one of them or both of them may be faked by a jet. For the definition of a fake lepton the isolation quality is reversed. For the electron channel it is the *likelihood* and for the muons it is the combination of  $E_T^{Halo}$  and  $p_T^{tracks}$ . Thus for a jet “faking” a lepton, it is required that the event has one good quality lepton

---

<sup>6</sup>For the sake of completeness the mass window for electron channel is  $70 < M_Z < 110$  GeV and for muon channel  $50 < M_Z < 130$  GeV.



and one bad quality, jet-like (fake) lepton; and for two “fakes” we require two bad quality leptons.

The definition of the fake electron is the same as the good one’s, other than likelihood. Its likelihood value should be in the range  $0 < lhood < 0.2$ . If an electron doesn’t have an associated track its likelihood is assigned a negative value that’s why reversal of the likelihood cut is limited to positive values.

The definition of the fake muon is the same as the good one’s, except the isolation requirement is completely removed along with events containing good muons.

The comparison of Monte Carlo events with data events in the low di-lepton mass region is done. The difference between the number of data events and the number of Monte Carlo events is the jet events in this region. The number of possible jet events in the Z-mass region, can be found out by fitting this number to the di-lepton mass distribution of fake electrons. See Figure 5.4(a). However, after all the cuts, we didn’t even need to make the fit since the number of events in Z-mass window was very low. See Figure 5.4(b,c,d). From this one can conclude that the number of jet events are negligibly small.

Thus, in this analysis the number of jet events is set to zero.

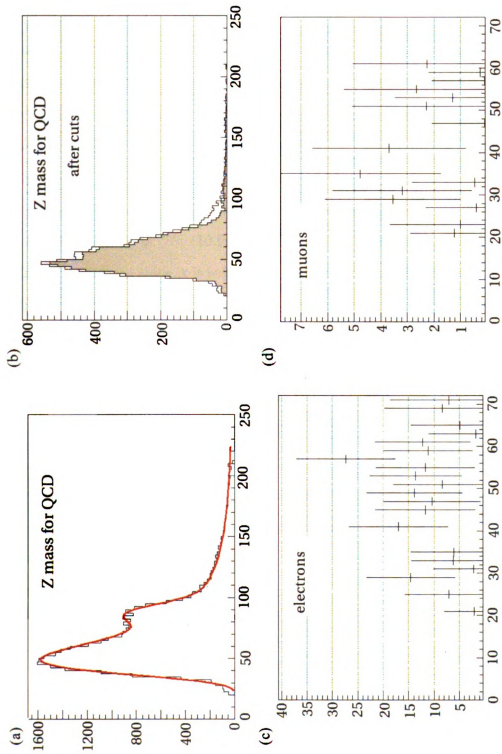


Figure 5.4: The figure shows (a) the Z mass distribution for the QCD events and the fit before the application of cuts; (b) same distribution after the cuts; the number of expected events in different bins before normalization for (c) electron and (d) muon channels.

### 5.3.2 *top-antitop* Backgrounds

Only when both of the W bosons in  $t\bar{t}$  events decay to leptons (di-lepton channel) the final particles of this process ( $t\bar{t}$ ) are the same as the signal's ( $WZ/ZZ$ ), two leptons and two jets with one addition, neutrino. However, the presence of the neutrinos in the  $t\bar{t}$  events helps eliminate a big portion of these events by the MET cut imposed on the events. Figure 5.6 shows the effect of MET cut on  $t\bar{t}$  events. In the electron channel the reduction of  $t\bar{t}$  events is 90% ( $27.64 \rightarrow 2.78$ ) whereas in the muon channel it is 75% ( $16.99 \rightarrow 4.30$ ) with the  $MET$  and  $Z$  mass window cut. From this picture alone it is safe to infer that by this cut alone we have a very good handle on  $t\bar{t}$  events. One other aspect of these events is that the two leptons don't have to be same kind for  $t\bar{t}$  events, which also helps reduce the background we get from these events.

The cut on the MET quantity is calculated by rounding off the cut removing most top-antitop events and keeping the signal events. Thus in the electron channel it is 45 GeV and in the muon channel it is 55 GeV. See Figure 5.5

The effect of MET cut on the events that are passing the Z-mass window cut is shown in Figure 5.6. The number of events entering that region is small, and by means of this cut the number of events gets even more smaller (less than 5 in both of the channels for RunIIa period data of  $\sim 1fb^{-1}$  data).

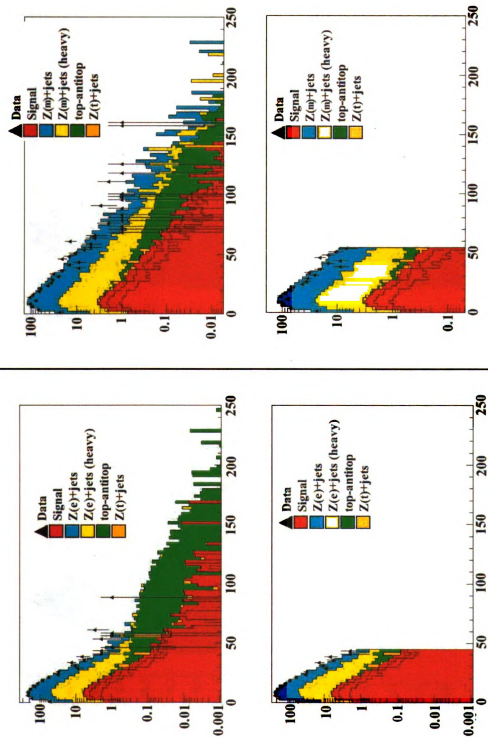


Figure 5.5: The figure shows MET distributions for the electron (left column) and the muon (right column) channels for Monte Carlo events. The effect of MET cut can be seen on the second row.

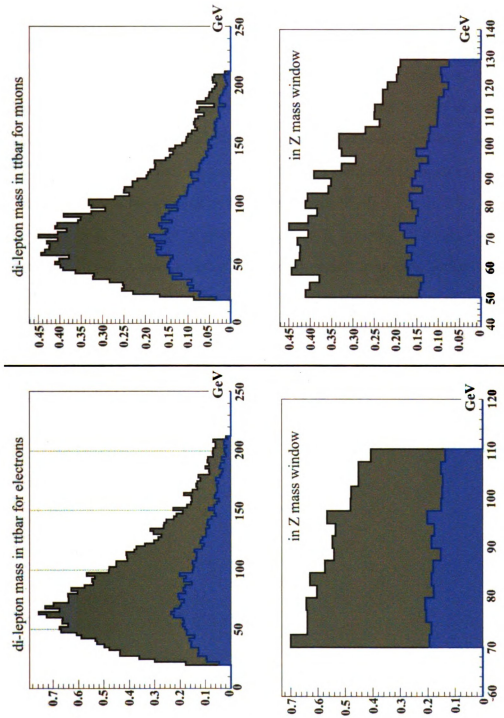


Figure 5.6: The figure shows di-lepton mass distributions for the electron (left column) and the muon (right column) channels for  $t\bar{t}$  events. In the same panel is shown before (in black) and after (in blue) the missing transverse energy cuts. While the first row shows whole mass range, the second row shows only Z mass window region.

### 5.3.3 $Z + jets$ Backgrounds

The production of a Z boson accompanied with jets has the exact same signature as our signal. The production mechanism, however, is entirely different. Initial or final state gluon radiation can cause these events be created as well as jets from soft interactions. The only remarkable difference between  $Z + jets$  and the signal ( $WZ/ZZ$ ) is that while the di-jet mass spectrum of the former has an exponential form, the latter has a sharp peak at the W mass region. See Figure 5.7

The number of events for a given luminosity is favoring  $Z + jets$  events by one to two hundred. Thus, in order to separate signal from this background, we have looked at several different methods, and decided that an ‘improved’ likelihood method gives enough power to distinguish one from the other.

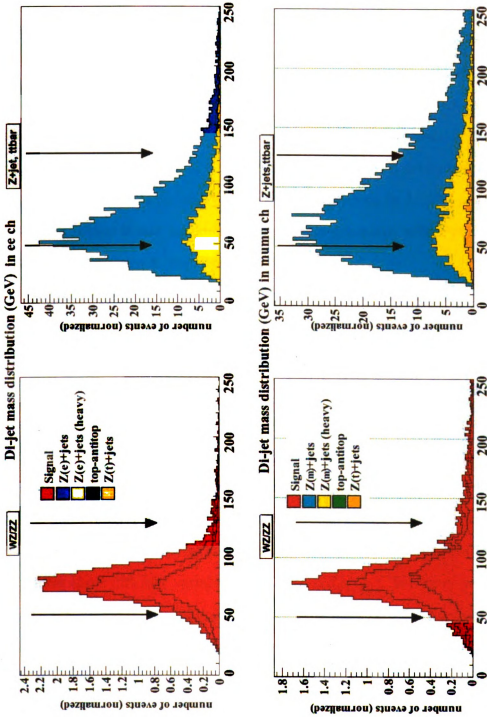


Figure 5.7: The di-jet mass distributions for signal (left hand side) and background (right hand side) Monte Carlo events for electron (first row) and muon (second row) channels. To preserve the relative strengths of the distributions, they are not normalized one.

## 5.4 Corrections

Before proceeding any further, it should be stated that, recently another corrections to the Monte Carlo generated (W/Z) + jets events are proposed. The reason for this correction is that Monte Carlo events generated by Pythia are not capable of representing the distributions of the jets' eta ( $\eta_j$ ) and of the distance between the jets ( $\Delta R_{j1,j2}$ ) for boson (W/Z) + jets events. This study is dependent on ( $\eta_j$ ), ( $\Delta R_{j1,j2}$ ); therefore it is necessary to do those corrections on MC Z+jets events. Although the reason is still not known fully, events generated with Pythia causes the discrepancies as seen in the Figure 5.8.

The recipe for dealing with this is as following. Since the reason behind the discrepancies are Pythia generated events, one should consider to correct those events only, by differing their weights in the plots. For this study,  $t\bar{t}$  events from background events and all of the signal events (WZ/ZZ) are excluded from this corrections because in their production Pythia was not used.  $Z + jets$  events, however, are generated by Pythia and the correction factors are calculated by using exclusive  $Z + jets$  events. Both of the channels (e and  $\mu$ ) the correction factors are calculated separately. At the pre-selection level, expected number of events for signal and top-antitop events are subtracted from the RunIIa Data set bin by bin in three different variables ( $\eta_{j1}$ ,  $\eta_{j2}$ ,  $\Delta R_{j1,j2}$ ). For every variable, a bin-by-bin ratio histogram is obtained between the data and the  $Z + jets$  Monte Carlo events. Then the ratio histograms are fitted to second degree polynomials giving rise to small but crucial corrections in the afore mentioned variables. See Figure 5.9, 5.10. The fit results are used as average corrections in the form of an event weight for all the variables that are used in this analysis. Any further cuts are applied after employing these corrections on every variable used in this analysis.



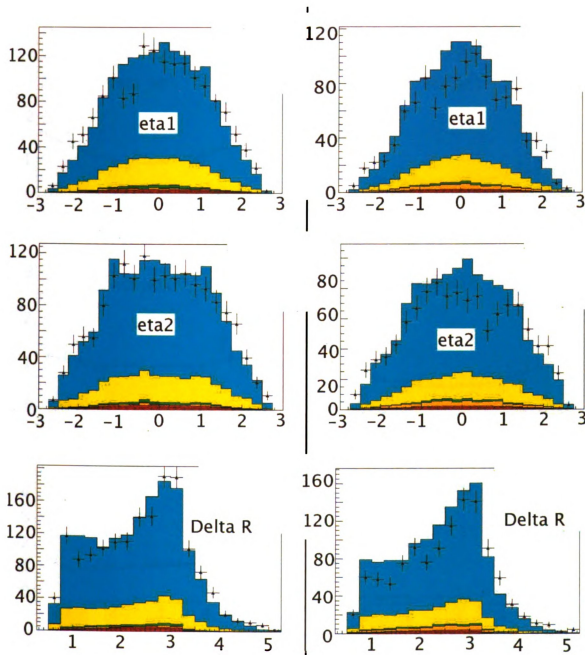


Figure 5.8: The figure shows the discrepancy between the Monte Carlo events and data for  $\eta_{j1}$ ,  $\eta_{j2}$  and  $\Delta R_{j1, j2}$  distributions (from top to bottom). On the left is shown the electron channel, and on the right is shown the muon channel. Since our result will heavily depend on these distribution, a correction factor is assigned as a weight to every event.

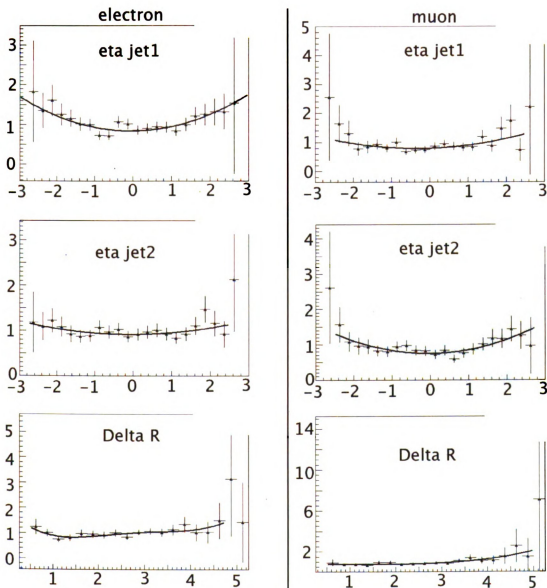


Figure 5.9: The figure shows the fits that are used for correcting event weights of the Monte Carlo events for  $\eta_{j1}$ ,  $\eta_{j2}$  and  $\Delta R_{j1,j2}$  distributions (from top to bottom). Since our result will heavily depend on these distribution, a correction factor is assigned as a weight to every event. Left column is for electron channel and right column is for muon channel.

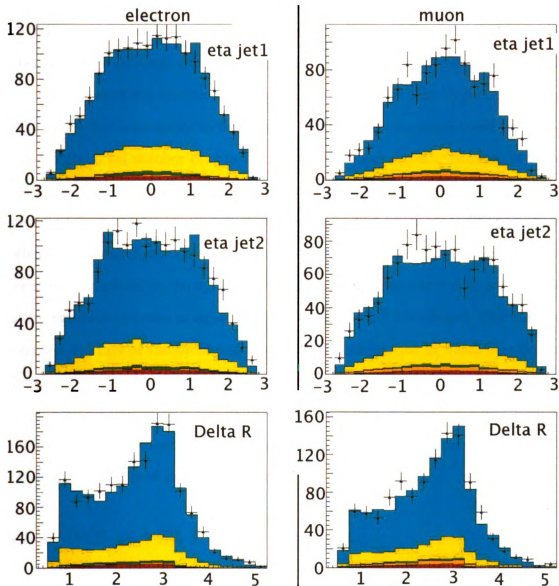


Figure 5.10: The figure shows distributions of  $\eta_{j1}$ ,  $\eta_{j2}$  and  $\Delta R_{j1,j2}$  (from top to bottom) after corrections are applied. Left column is for electron channel and right column is for muon channel.

## 5.5 Technique

The rule of thumb “the simpler the better” has to be given up in some cases. This analysis is one of them. The cross sections of the processes are very low ( $\sim 3.5$  pb for WZ production and  $\sim 1.5$  pb for ZZ production). As if this is not enough, the cross section of the most similar background is very high ( $\sim 750$  pb for Z+jets). If one were to count the number of signal events that can be seen by just employing square cuts, the uncertainty in the number of just this background could be on the order of the total number of expected events from the signal<sup>7</sup>. Because of these reasons one has to develop new methods, for this analysis I checked the feasibility of the next two methods: the matrix element method and the random forest method. While the former requires a through knowledge of the Z+jets matrix elements and needs huge numbers of cpu cycles for the calculations; the latter does not provide much difference in terms of significance than the method I developed. The method used is a mixture of the likelihood method and decision tree in which selection of the variables are not left to computer but done by the analyser.

Although a multivariate technique will be employed, pure samples will improve our ability of discriminating signal from background. There are three obvious cuts which will be explored in the next section.

### 5.5.1 WZ and ZZ Event Selection

A further selection of WZ and ZZ events following  $Z \rightarrow e^+e^-$  and  $Z \rightarrow \mu^+\mu^-$  selection is done by requiring the following cuts.

The usual way for an analysis is to use square cuts and get a limited region in which the number of events is comparable to or more than the number of background events. For this analysis, however, after selecting objects one has to

---

<sup>7</sup>The expected number of events for WZ and ZZ processes for whole RunIIa period ( $\sim 1fb^{-1}$ ) is about 36 events.

use more complicated methods such as multivariate techniques since the properties of the background differ from the signal only slightly. But in order to improve the separation power of those techniques, some obvious cuts are employed. Those cuts are :

- The di-jet mass window cut
- The  $\eta_j$ - $\eta_j$  cut
- The  $p_T$ - $p_T$  cut

### **The di-jet mass window cut**

Because we are interested in the cases where two jets decay from weak bosons, the reconstructed W/Z boson from the two jets should be in the vicinity of real W/Z mass ( $\sim 80$  GeV and  $\sim 90$  GeV). While the signal Monte Carlo events have a definite peak in this region, the background events show an exponential decay. See Figure 5.11. The di-jet mass should be above 50 GeV and below 130 GeV.

$$50\text{GeV} < M_{jj} < 130\text{GeV} \quad (5.5)$$

See Table 5.2. In the case where an event has more than two jets, selection of the jets are limited to the first and second jets. As mentioned before this is the correct choice 90% of the time. It is possible to choose the combination that is giving the mass closest to  $M_W$ , we avoided that to not introduce an unknown bias.

### **The $\eta_j$ - $\eta_j$ cut**

Decaying from a heavy particle causes the jets to be boosted. This results in the jets being closer to each other in the signal Monte Carlo events compared to the background Monte Carlo events. When one multiplies the physics  $\eta$  of the jets, one expects that the distribution be skewed to the right for the signal and no

skewness for the background since in the latter the jets don't originate from one heavy particle but have random directions and origins. In Figure 5.12 this cut is shown as  $\eta_j - \eta_j > -1$ . For its values please see Table 5.3.

### **The $p_T$ - $p_T$ cut**

As mentioned earlier the momentum carried in transverse directions by jets should be large due to momentum conservation. Although events are already required to have a jet with a  $p_T > 20$  GeV there is still some room to go. Our region of interest is events with a W/Z decaying into jets. This means that the two jets are strongly coupled together. Even by employing a very simple relation between the two jets will help us recover lost events due to square cuts and removing events sneaking in originating from background. Thus, a linear relation between first and second jets  $p_T$ 's are used. A triangular cut is employed on the two highest jets  $p_{T_{jet1}}$  vs  $p_{T_{jet2}}$ . See Figure 5.13. As it is seen on the plots a definite peak exists in signal. As an example the cuts put on the Figure 5.13 are

$$\frac{p_T^{j2}}{40} + \frac{p_T^{j1}}{60} - 1 > 0 \quad (5.6)$$

for electron channel and for muon channel it is:

$$\frac{p_T^{j2}}{40} + \frac{p_T^{j1}}{80} - 1 > 0 \quad (5.7)$$

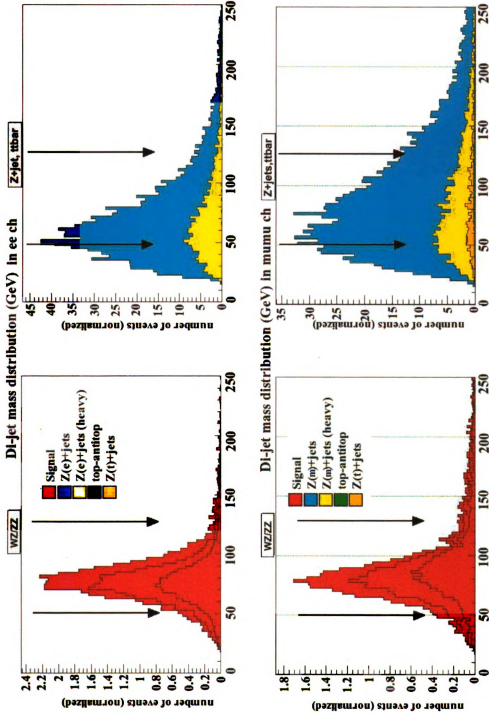


Figure 5.11: The di-jet mass distributions for signal (left hand side) and background (right hand side) Monte Carlo events for electron (first row) and muon (second row) channels. To preserve the relative strengths of the distributions, they are not normalized one.

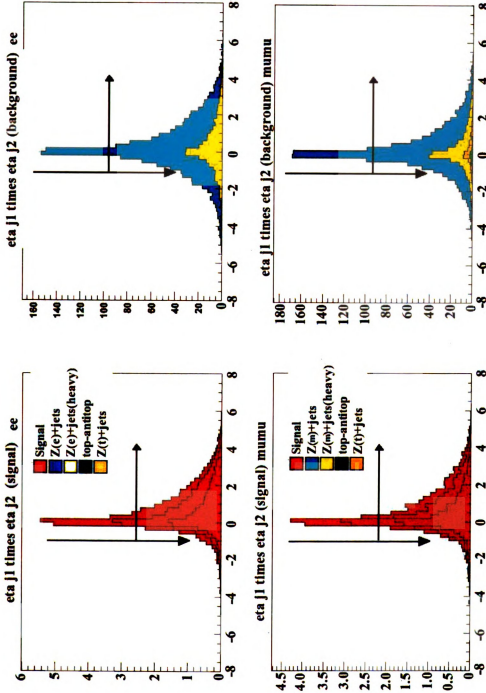


Figure 5.12: The distributions for  $\eta_{jet1} \times \eta_{jet2}$ . The one on the left is obtained by using only the signal Monte Carlo events. The one on the right side is for the background Monte Carlo events. There is an obvious skewness towards right in the signal distribution, which is expected.



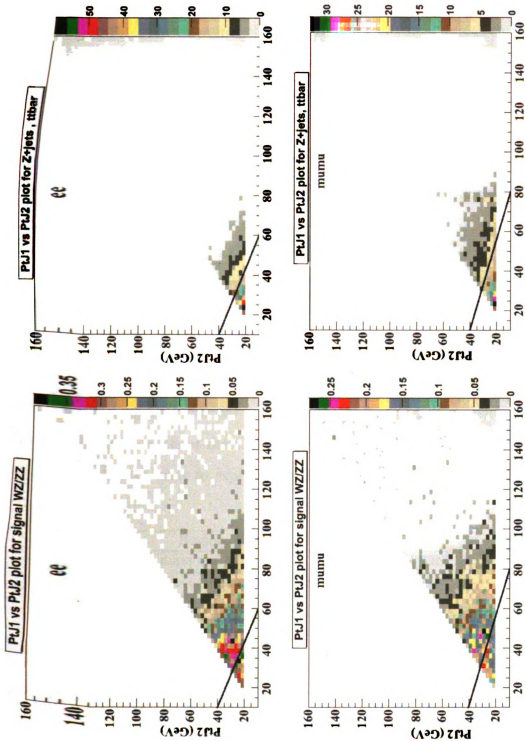


Figure 5.13: The distributions for  $p_T^{j1}$  vs  $p_T^{j2}$ . The left column is for electron channel and the right column is for muon channel. The lines show a probable cut on these two variable together. It is obvious from the plots that background events are mostly below the line.

Before giving the values of these cuts, another different aspect of this analysis should be clarified. It is discovered that, instead of blindly applying all the cuts to all the events, it is much wiser to select cuts event by event. Due to time restrictions on the analysis, it is chosen to separate events into four different regions and apply an average cut on the events in their regions. For this purpose  $\Delta R$  between the first two jets is used. The regions are shown in Table 5.1. In the following section it will be explained why one separates the phase space into four regions.

Region	I	II	III	IV
$\Delta R$	$< 1.8$	$\geq 1.8, < 2.3$	$\geq 2.3, < 2.9$	$> 2.9$

Table 5.1: The division of regions with respect to the distance between the two highest  $p_T$  jets in the events.

The limits of the regions are chosen so that on average the changes in the behaviour of the distribution would be captured. Although it is mentioned that in different regions different cuts are applied, what is shown in the previous figures are all of the events without dividing them into four regions. So that the reader has a general idea of what to expect. For the di-jet mass window cut please see Table 5.2

Region	For all regions
Di-jet mass cut $e$ channel	$50 < M_{jj} < 130 \text{ GeV}$
Di-jet mass cut $\mu$ channel	$50 < M_{jj} < 130 \text{ GeV}$

Table 5.2: The di-jet mass cut is kept constant over the regions.

The next tables, Tables 5.3 and 5.4, show the cuts put on the  $\eta_j - \eta_j$  and the  $p_T - p_T$  variables respectively.

Region	I	II	III	IV
$\eta_{jet1} * \eta_{jet2}$ for electrons	$> -0.725$	$> -0.525$	$> -0.425$	$> -0.425$
$\eta_{jet1} * \eta_{jet2}$ for muons	$> -0.825$	$> -0.725$	$> -0.925$	$> -0.525$

Table 5.3:  $\eta_{jet1} * \eta_{jet2}$  cuts are shown in different regions of  $\Delta R$  for both electrons and muons

Region	I	II	III	IV
$p_T^{j1}$ vs $p_T^{j2}$ for electrons	(74,53)	(73,42)	(78,34)	(49,46)
$p_T^{j1}$ vs $p_T^{j2}$ for muons	(201,39)	(114,29)	(84,24)	(33,52)

**Table 5.4:**  $p_T^{j1}$  vs  $p_T^{j2}$  cuts are shown in different regions of  $\Delta R$  for both electrons and muons. The numbers given here are the intersection points of a line with  $p_T^{j1}$  and  $p_T^{j2}$  plane.

If an event has a value for  $\eta_j - \eta_j$  greater than the one mentioned in the table, it passes this cut. If an event falls in the region above defined by the line intersecting with  $x - y$  ( $p_T^{j1} - p_T^{j2}$ ) axes at points given in the Table 5.4, it passes this cut also.

The values of the cuts for the different channels are shown in the same tables. They are calculated by finding the values for which the significance of the signal is highest. Its definition is given below:

$$\sigma = \frac{N_{signal}}{\sqrt{N_{signal} + N_{background}}} \quad (5.8)$$

where  $N_{signal}$  is the number of signal Monte Carlo events passing a certain cut and  $N_{background}$  is the number of background Monte Carlo events passing the same cut. The cut point for which this value is the maximum is chosen for the most optimum cut. For all of the three cuts mentioned above this formula is used. The optimized cuts are applied for the following optimization.

### 5.5.2 Likelihood Method

For this analysis, a modified simple likelihood is chosen to separate signal from the background.

In the very early versions of the method, we were using only five variables and two of them were  $\eta_{j1} \times \eta_{j2}$  and  $\Delta R_{j1, j2}$ . They are taken out of the list of the likelihood variables for the following reasons: The cut imposed on the former one

is powerful and removes dissimilarities between the signal events and background events, we didn't want to use it in the likelihood any further. The latter, on the other hand is used to define different regions. The idea behind it is that not all of the variables have the same discrimination strength in every phase space. For that purpose we compared variables in different regions for their effectiveness and separation power. When building the likelihood, we use only those variables that are more powerful in that particular region where the event falls. The comparison is done based on the histograms and the k-test. For that test the 'R' program <sup>8</sup> is used. By the same token, one should doubt the validity of the implications such as any cut has the same significance in every point in phase space. That is why, after the division of the phase space, we re-optimize the cuts specific to this analysis. It turned out that, indeed, applying a cut blindly, with an assumption that in every region it has the same desired effect is wrong. One can only optimize a cut to the average this way. However, optimizing the cuts for different regions could buy some significance for the analyzer.

In order to build the likelihood among the many possible variables, the ones that separate signal and background best in Monte Carlo events are chosen. They are:

- The reconstructed di-jet mass
- The transverse momentum of the leading jet
- The transverse momentum of the trailing jet
- The rapidity of the Z boson in the WZ/ZZ frame
- The angle of  $\alpha_R$
- The  $p_T$  difference of the di-jet and Z

---

<sup>8</sup> Please see <http://www.r-project.org>

- The  $p_T$  of the di-jet object
- The  $p_T$  of WZ/ZZ frame
- The cosine of the angle between the two jets
- The cosine of the angle between the Z and jet

The definition of the likelihood is given below:

$$L(x) = \frac{P_{sig}(x)}{P_{sig}(x) + P_{bkg}(x)} \quad (5.9)$$

$$P_{sig}(x) = \prod_i P_{sig}(x_i) \quad (5.10)$$

$$P_{bkg}(x) = \prod_i P_{bkg}(x_i) \quad (5.11)$$

where  $x$  is a vector of afore mentioned variables;  $P_{sig}(x_i)$  is the probability of being a signal (WZ/ZZ) event;  $P_{bkg}(x_i)$  is the probability of being the total background events (Z+jets and top-antitop). These probabilities are obtained from the Monte Carlo distributions of the variables entering the likelihood calculation. Again, there are four different MC distributions for a variable corresponding to four different regions of the phase space. After obtaining distributions of the variables for different regions, these distributions are normalized to unity to get corresponding probability for that variable in that region. This means that the distribution of the variable is translated to a binned probability distribution for the signal and background Monte Carlo events. Some work went into finding the best binning for the histograms when calculating corresponding probability. If one considers the limiting cases it will be apparent why one needs an optimum set of binning. For instance, if all of the histograms had only one bin then the likelihood would come out as 0.5. If, on the other hand histograms had too large binning then

we would see unphysical accumulation and spikes on the two extremes; many of the events would not have a valid likelihood value. Because very fine binning means empty bins in the distribution's tail for some of the variables, such as transverse momentums. It is essential that without including nonphysical cases, the likelihood distribution has discriminative power. Therefore it is required that the likelihood distribution be a smooth one.

Ideally, one should use

$$P_n(x) = P_n(x_i) \quad (5.12)$$

for calculation of probabilities. That is to say if there are 'n' variables, one should use an 'n' dimensional probability space for calculating p values entering the likelihood. However, this requires infinite amount of signal and background Monte Carlo events, especially for the case in the hand since we have ten variables. For an 'n' dimensional likelihood to be effective, every cell in 'n' dimension should have significant number of events in them. Instead, we chose not to include some of the variables in some regions when calculating the likelihood.

Shown in the Figure 5.14 is the example of a distribution and its corresponding probability distribution. It is required to remove the legends in some of the distributions for their clarity. Thus, in this picture is explained the color codes used throughout this section. The hatched histograms, always in red (signal MC) and black (background MC), are for probability distributions. Other histogram is for the comparison of the data points with the signal + background distributions.

### The reconstructed di-jet mass

In order to calculate the di-jet mass, an event should at least have two jets. Thus there is an implied cut on the number of jets in the events. If an event has more than two jets, then the recipe is to utilize only the ones that have the highest

number of  
40  
35  
30  
25  
20  
15  
10  
5  
0

Flow

train

prod

dev

ET i

jet t

is ri

or Z

de

Fig

MC

his

the

Tr

in

Pe

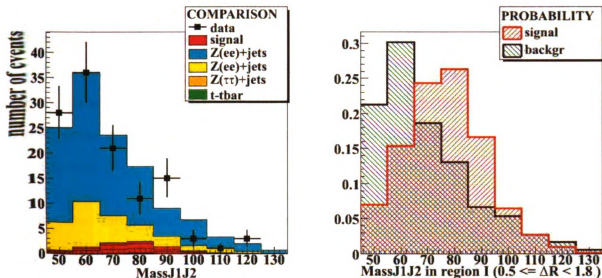


Figure 5.14: An example distributions showing the color codes used in this thesis.

transverse momentum. There is an error associated with this choice, since a jet produced with WZ or ZZ events is not guaranteed to have less  $p_T$  than those jets decaying from the bosons. More than 90% of the time the selection for the highest  $p_T$  is correct, which means that it comes from the W or Z, however for the second jet this efficiency goes down close to 85%. As mentioned earlier the di-jet mass is the most powerful discriminant, because coming from a high mass particle (W or Z), the di-jet has a definite peak in its mass distribution whereas background doesn't form due to the fact that there is almost no relation between the jets. See Figures 5.15, 5.16, 5.17 and 5.18. In these figures left column shows the data MC event comparison whereas in the right column the corresponding probability distributions are shown. Probabilities of the individual events are obtained from these probability distributions for the likelihood discriminant.

### Transverse momentum of the leading jet

In the previous bullet it is mentioned that the selection of the first jet is usually correct. That's why the average  $p_T$  is higher in signal MC events than in background



MC events. Moreover the background MC events has a long tail, indicating that they are not strongly coupled to other objects in the event. See Figures 5.19, 5.20, 5.21 and 5.22. The left column shows data MC event comparison and the right column shows corresponding probability distributions. Probabilities of the individual events are obtained from these probability distributions for the likelihood discriminant.

### **Transverse momentum of the trailing jet**

Trailing in this context means the second highest  $p_T$ . Due to requiring a second jet in the event, we are placing an implied lower cut on the number of jets, but there is no upper cut on the number of jets that may be found in the event. Again having decayed from a heavy particle, for signal MC events  $p_T$  distribution has higher mean values compared to background MC events. One can see a tail for background events also. See Figures 5.23, 5.24, 5.25 and 5.26. The left-hand side column shows data MC comparison whereas right-hand side column shows corresponding probability distributions for signal and background MC events. Probabilities of the individual events are obtained from these probability distributions for the likelihood discriminant.

### **The rapidity of the Z boson in the WZ/ZZ frame**

In theory both of the bosons may be utilized equally, however, since Z bosons are constructed by leptons, and their measurements are more reliable due to the fact that most of the events have only two leptons, W bosons are not used for this variable. As seen in the Figures 5.27, 5.28, 5.29 and 5.30 the background events populates the  $y = 0$  region. This is a result of the balancing of the di-jet object in signal (WZ/ZZ) events. Whereas in the background the di-jet object is not fully correlated with the di-lepton object due to inclusion of an unrelated jets (first

or second highest  $p_T$  jet). The rapidity of the leptonic boson is expected to be central in background from the previous measurements of Z boson rapidity. The left column in these figures are for data MC event comparison, whereas the right one is for corresponding probability distributions. Probabilities of the individual events are obtained from these probability distributions for the likelihood discriminant.

### **The angleR : $\alpha_R$**

angleR is the angle between the reconstructed Z object in the WZ/ZZ frame and the direction of the WZ/ZZ frame itself. From the Figures 5.31, 5.32, 5.33, and 5.34, the distribution of this variable for signal events has a dip towards the center (especially in second and third regions), whereas the background distribution is more or less constant. This variable is one of the last additions to the set of variables. Data MC comparison is shown in the left column and probability distributions used in likelihood discriminant are shown in the right column. Probabilities of the individual events are obtained from these probability distributions for the likelihood discriminant.

### **The transverse momentum difference : $\Delta p_T^{Z,jj}$**

The transverse momentum difference of Z boson and di-jet object could be used as one of the discriminating distributions because of the correlation between di-jet and di-lepton objects. In the signal case they should balance each other, whereas in the background, we expect to see a slight skewness in the distribution. This variable is defined as

$$p_T^{jj} - p_T^{ll} \quad (5.13)$$

See Figures 5.35, 5.36, 5.37 and 5.38. Data MC comparison is shown in the left column and probability distributions used in likelihood discriminant is shown in the right column. Probabilities of the individual events are obtained from these

probability distributions for the likelihood discriminant.

**The transverse momentum of di-jet :  $p_T^{jj}$**

The transverse momentum of the di-jet object. It is expected to behave differently from the real  $W$  events since the jets cannot make a real  $W$ . The mean value for this distribution is expected to be greater in signal than in background. See Figures 5.39, 5.40, 5.41 and 5.42. Data MC comparison is shown in the left column and probability distributions used in likelihood discriminant is shown in the right column. Probabilities of the individual events are obtained from these probability distributions for the likelihood discriminant.

**The transverse momentum of center of mass :  $p_T^{WZ}$**

The transverse momentum of the  $WZ/ZZ$  frame is in a way an opposite to the transverse momentum difference. Any difference that is overlooked should emerge in this variable. This distribution behaves differently in electron channel than in muon channel. We suspect that since the only difference is the usage of muons instead of electrons while reconstructiong the leptonic  $Z$  boson, the resolution effects of the muon detector plays an important role here. See Figures 5.43, 5.44, 5.45 and 5.46. Data MC comparison is shown in the left column and probability distributions used in likelihood discriminant is shown in the right column. Probabilities of the individual events are obtained from these probability distributions for the likelihood discriminant.

**The angle between to jets :  $\cos \alpha_{j_1 j_2}$**

The correlation between the two jets for signal ( $WZ/ZZ$ ) events should manifest itself as a difference in the distribution of the angles between the two jets making the hadronic boson. For the cosine of the angle between the two jets having the

highest  $p_T$  see Figures 5.47, 5.48, 5.49 and 5.50. As mentioned before there is an uncertainty attached to the selection of the correct jets combination making up the boson (correct for 85% of the time). Data MC comparison is shown in the left column and probability distributions used in likelihood discriminant is shown in the right column. Probabilities of the individual events are obtained from these probability distributions for the likelihood discriminant.

### **The angle between the first jet and Z : $\cos \alpha_{j_1 Z}$**

There is another angle which should be different between signal (WZ/ZZ) and background is the angle between the first jet and the reconstructed Z boson. Z boson and the first jet combination is more reliable because the first jet assignment is 90% of the time correct, that's why the angle between second jet and the leptonic boson was not chosen. For the distributions please see the Figures 5.51, 5.52, 5.53 and 5.54. Data MC comparison is shown in the left column and probability distributions used in likelihood discriminant is shown in the right column. Probabilities of the individual events are obtained from these probability distributions for the likelihood discriminant.

In the Tables 5.5 and 5.6, the variables and their respective regions are shown for electron and muon channels respectively.

There are correlations between the variables. In order to properly take into account for these correlations, one should build the likelihood in multiple dimensions. Although this is not impossible, yet it is quite impractical, since for building such multiple dimensional likelihood one literally needs hundreds of millions of Monte Carlo events and one can make some assumptions to ease the burden on the event generation. The number of necessary events is so large because of the following reasons:

- For this method to work, one has to bin the phase space in the same number

Region	I	II	III	IV
$\Delta R$	$< 1.8$	$\geq 1.8, < 2.3$	$\geq 2.3, < 2.9$	$\geq 2.9$
<i>EM Channel Variables</i>	$M_{JJ}$	$M_{JJ}$	$M_{JJ}$	$M_{JJ}$
	$P_T^{J1}$	$P_T^{J1}$	$P_T^{J1}$	$P_T^{J1}$
	$P_T^{J2}$	$P_T^{J2}$	$P_T^{J2}$	$P_T^{J2}$
		$\alpha_R$	$\alpha_R$	$\alpha_R$
	$y_Z$	$y_Z$	$y_Z$	$y_Z$
	$\cos \alpha_{J1, Z}$	$\cos \alpha_{J1, Z}$	$\cos \alpha_{J1, Z}$	$\cos \alpha_{J1, Z}$
		$\cos \alpha_{J1, J2}$	$\cos \alpha_{J1, J2}$	$\cos \alpha_{J1, J2}$
		$P_T^{J1J2, Z}$		$P_T^{J1J2, Z}$
	$\Delta P_T^{J1J2, Z}$	$\Delta P_T^{J1J2, Z}$		
	$P_T^{J1J2}$	$P_T^{J1J2}$		

Table 5.5: The names of the variables are given in their region

Region	I	II	III	IV
$\Delta R$	$< 1.8$	$\geq 1.8, < 2.3$	$\geq 2.3, < 2.9$	$\geq 2.9$
<i>MUChannelVariables</i>	$M_{JJ}$	$M_{JJ}$	$M_{JJ}$	$M_{JJ}$
		$P_T^{J1}$	$P_T^{J1}$	$P_T^{J1}$
	$P_T^{J2}$	$P_T^{J2}$	$P_T^{J2}$	$P_T^{J2}$
	$\alpha_R$	$\alpha_R$	$\alpha_R$	$\alpha_R$
	$y_Z$	$y_Z$	$y_Z$	$y_Z$
	$\cos \alpha_{J1, Z}$	$\cos \alpha_{J1, Z}$	$\cos \alpha_{J1, Z}$	$\cos \alpha_{J1, Z}$
		$\cos \alpha_{J1, J2}$		$\cos \alpha_{J1, J2}$
	$P_T^{J1J2, Z}$	$P_T^{J1J2, Z}$	$P_T^{J1J2, Z}$	$P_T^{J1J2, Z}$
	$\Delta P_T^{J1J2, Z}$	$\Delta P_T^{J1J2, Z}$	$\Delta P_T^{J1J2, Z}$	
	$P_T^{J1J2}$		$P_T^{J1J2}$	$P_T^{J1J2}$

Table 5.6: The names of the variables are given in their region

of dimensions as the number of variables which results in very few to none events in some bins. This causes unrealistic results.

- One can increase the bin sizes, however after a point the goal of using this techniques blurs away and the method doesn't deliver any separation power.

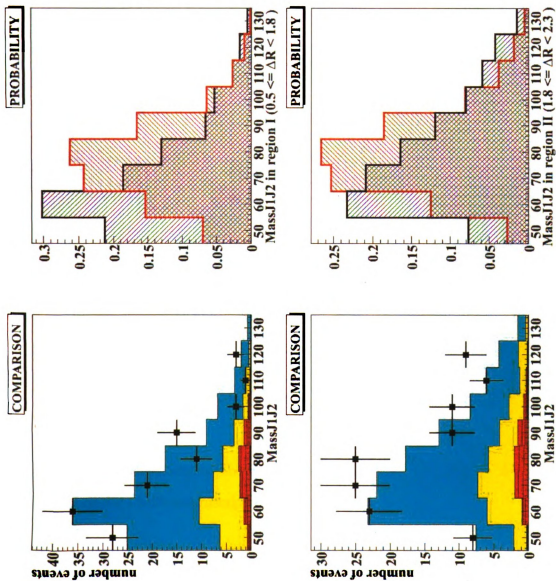


Figure 5.15: The distributions for di-jet mass for electron channel in first and second regions for likelihood discriminant input.

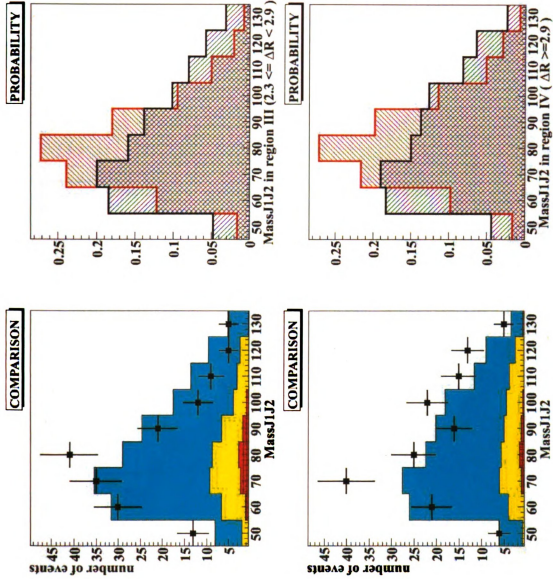


Figure 5.16: The distributions for di-jet mass for electron channel in third and fourth regions for likelihood discriminant input.



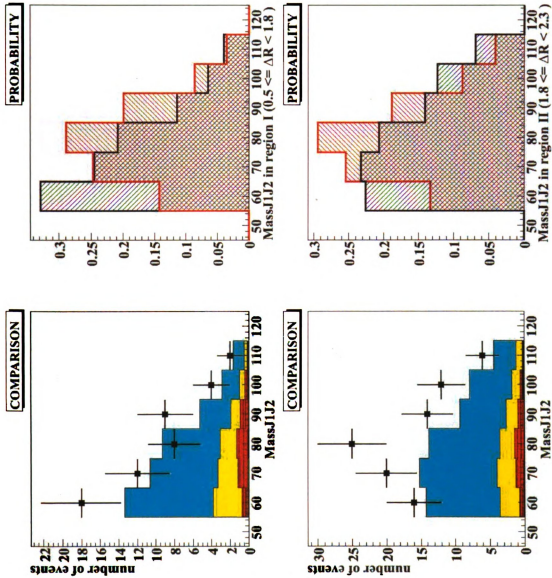


Figure 5.17: The distributions for di-jet mass for muon channel in first and second regions for likelihood discriminant input.

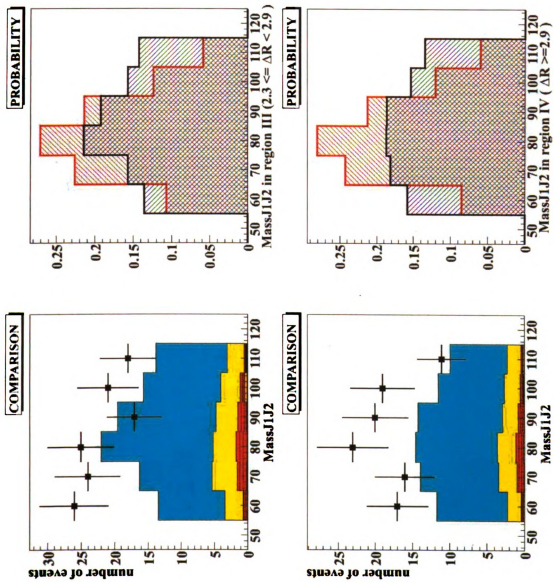


Figure 5.18: The distributions for di-jet mass for muon channel in third and fourth regions for likelihood discriminant input.

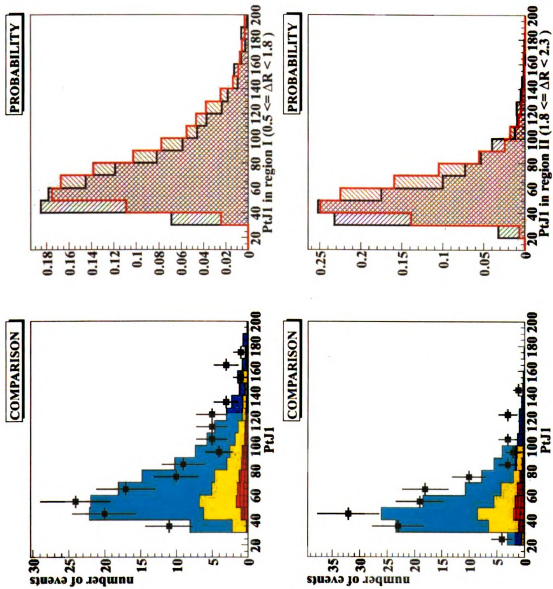


Figure 5.19: The distributions for leading jet  $p_T$  for electron channel in first and second regions.

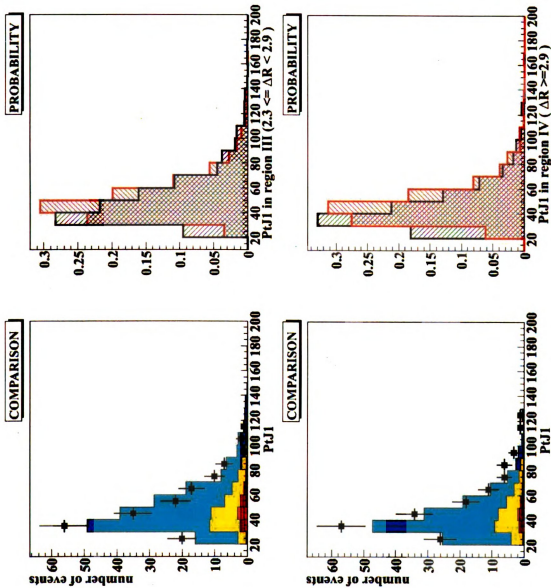


Figure 5.20: The distributions for leading jet  $p_T$  for electron channel in third and fourth regions.

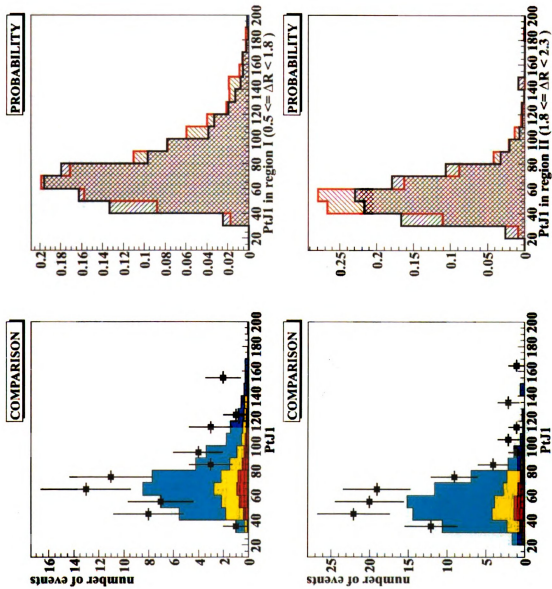


Figure 5.21: The distributions for leading jet  $p_T$  for muon channel in first and second regions.

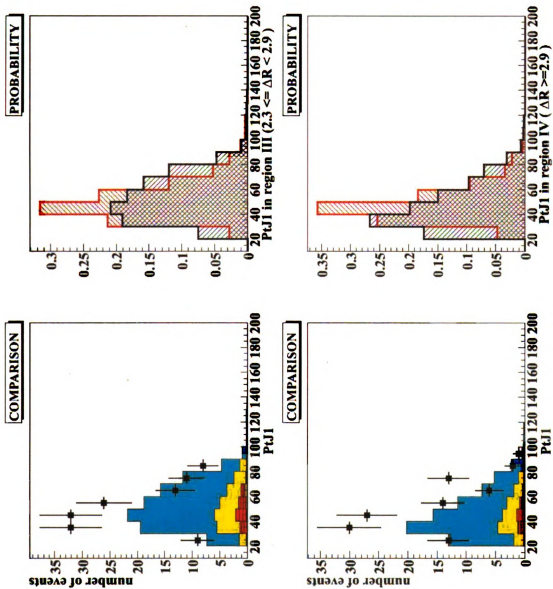


Figure 5.22: The distributions for leading jet  $p_T$  for muon channel in third and fourth regions.

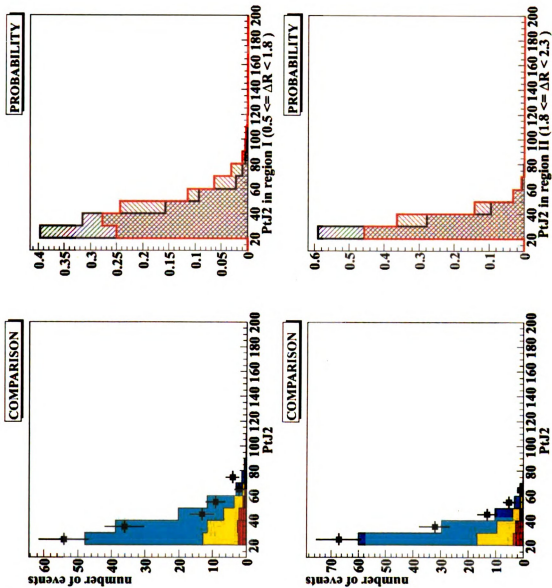


Figure 5.23: The distributions for second jet  $p_T$  for electron channel in first and second regions.

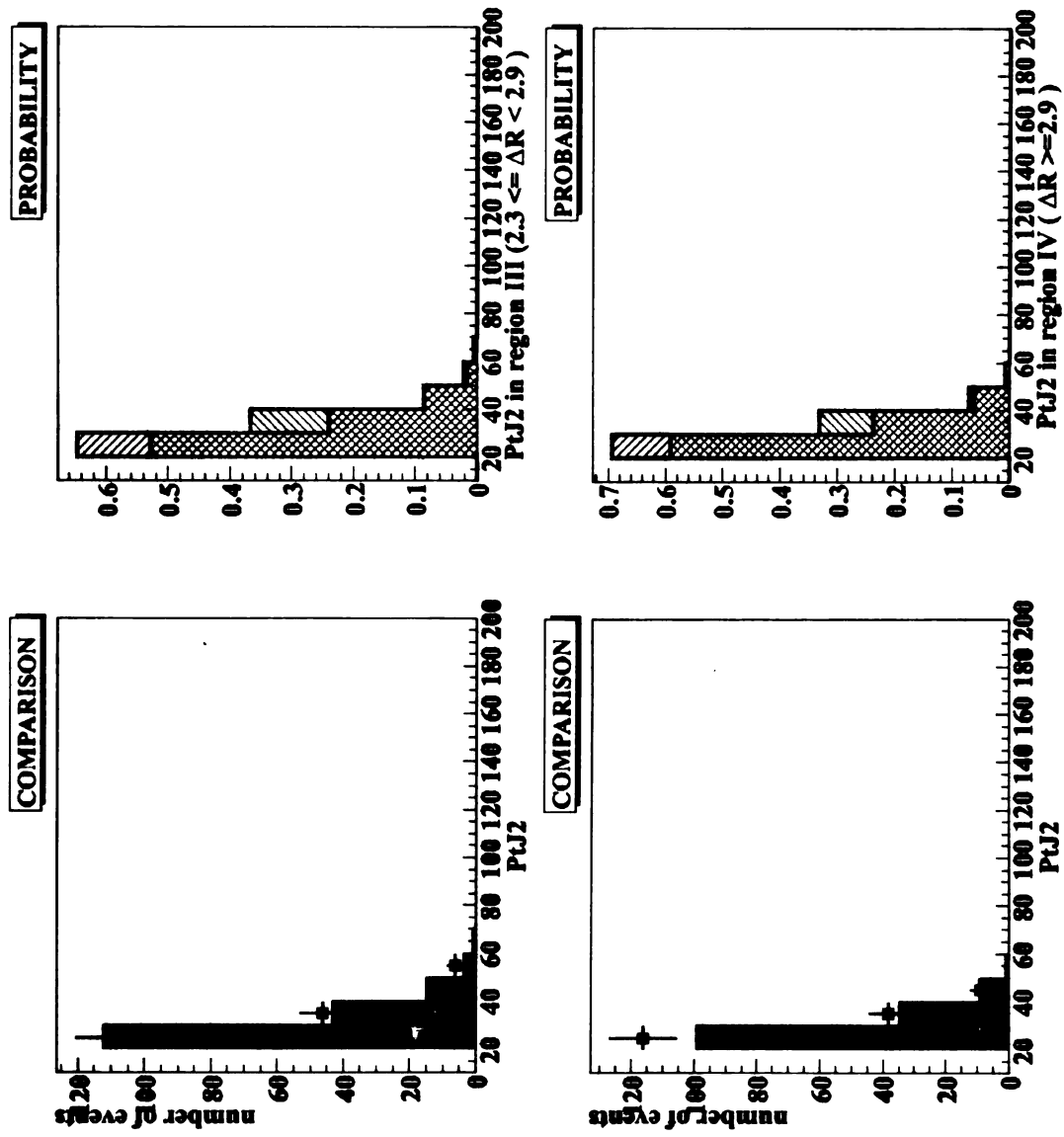


Figure 5.24: The distributions for second jet  $p_T$  for electron channel in third and fourth regions.



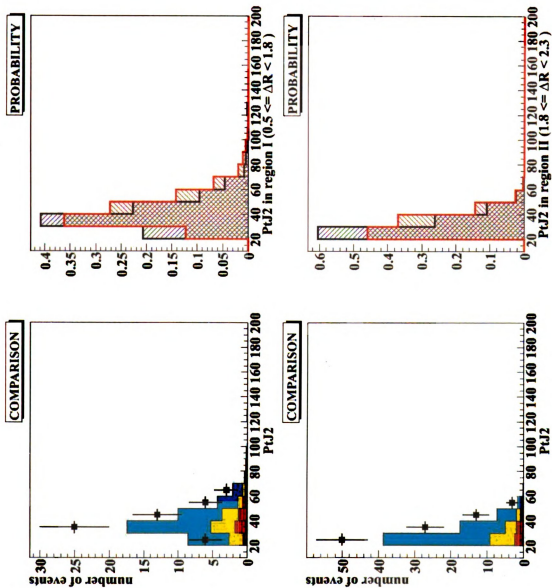


Figure 5.25: The distributions for second jet  $p_T$  for muon channel in first and second regions.

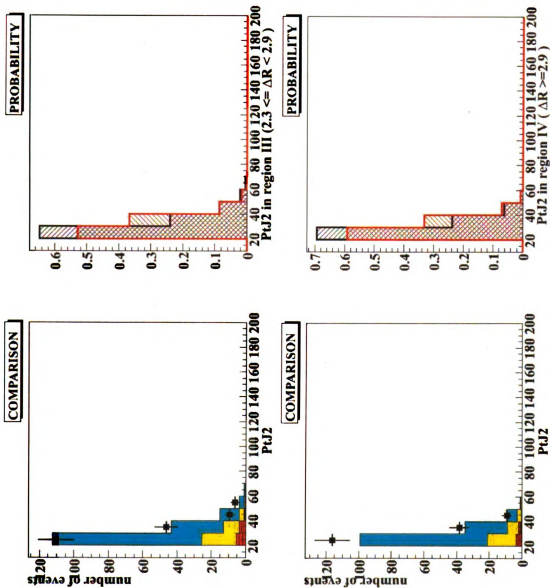


Figure 5.26: The distributions for second jet  $p_T$  for muon channel in third and fourth regions.

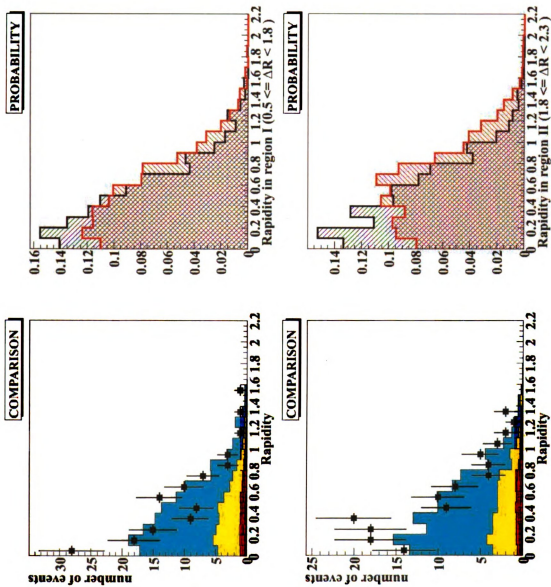


Figure 5.27: The distributions for Z rapidity in the center of mass frame of W/Z (di-jet) and Z (di-lepton) frame for electron channel in first and second regions.

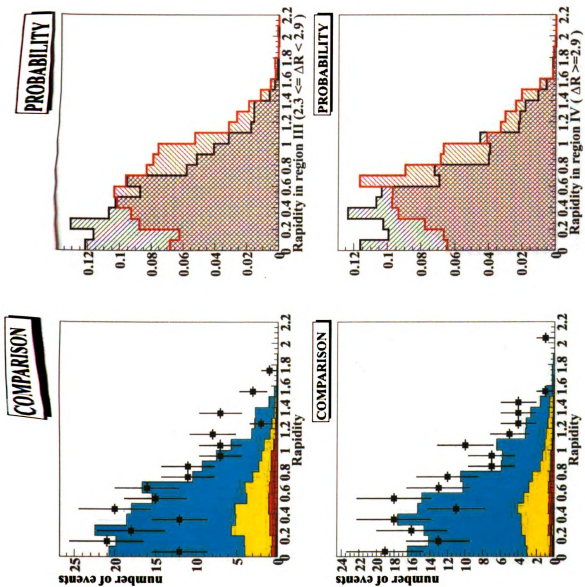


Figure 5.28: The distributions for Z rapidity in the center of mass frame of W/Z (di-jet) and Z (di-lepton) frame for electron channel in third and fourth regions.

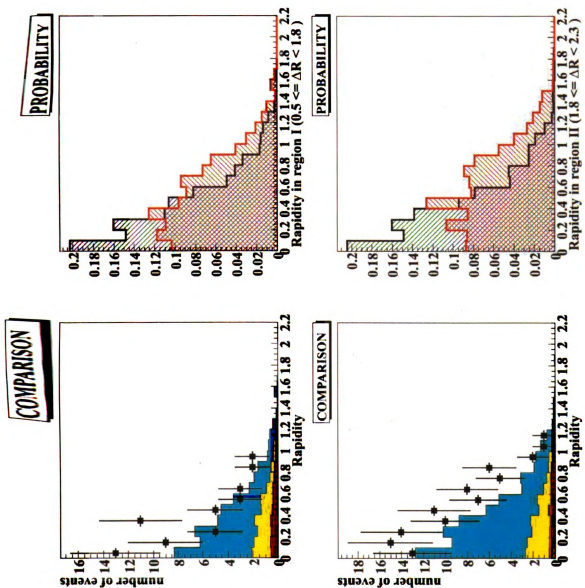
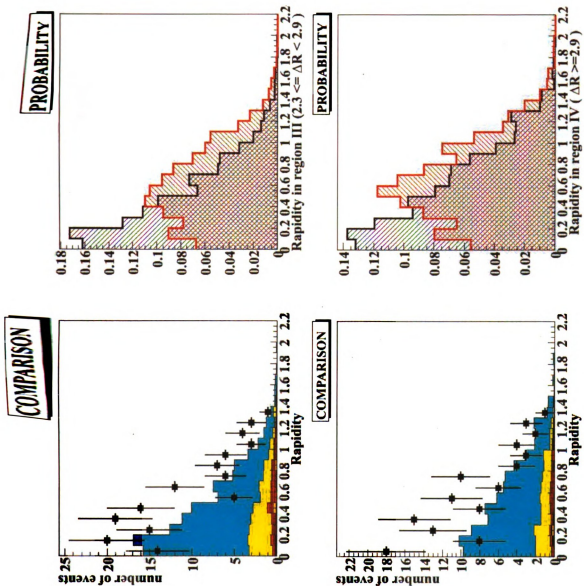
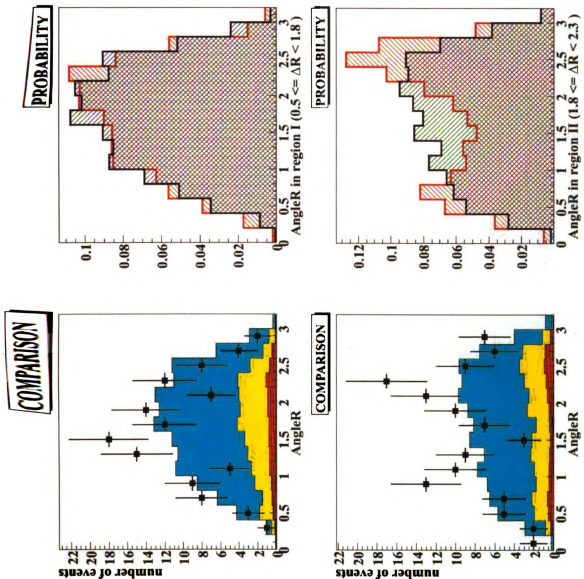


Figure 5.29: The distributions for Z rapidity in the center of mass frame of W/Z (di-jet) and Z (di-lepton) frame for muon channel in first and second regions.



**Figure 5.30:** The distributions for Z rapidity in the center of mass frame of W/Z (di-jet) and Z (di-lepton) frame for muon channel in third and fourth regions.



**Figure 5.31:** The distributions of the angle between reconstructed Z object and the center of mass frame of W/Z (di-jet) and Z (di-lepton) objects for electron channel in the first and second regions.

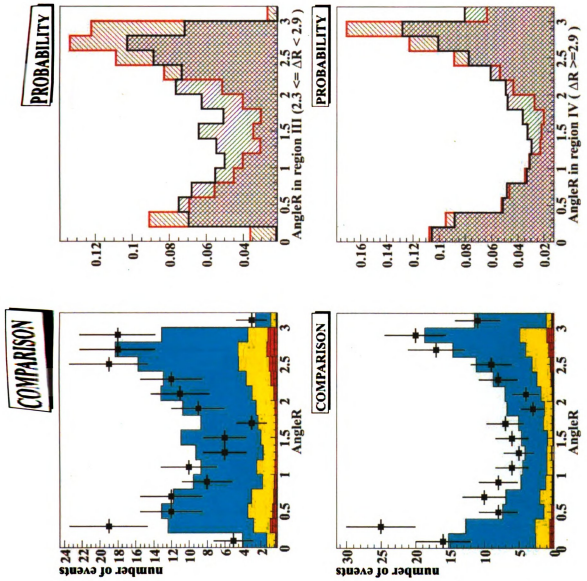


Figure 5.32: The distributions of the angle between reconstructed Z object and the center of mass frame of W/Z (di-jet) and Z (di-lepton) objects for electron channel in the third and fourth regions.



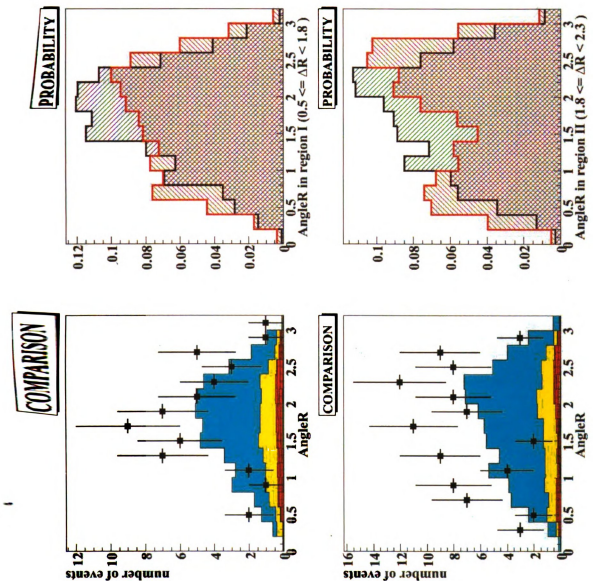


Figure 5.33: The distributions of the angle between reconstructed Z object and the center of mass frame of W/Z (di-jet) and Z (di-lepton) objects for muon channel in the first and second regions.

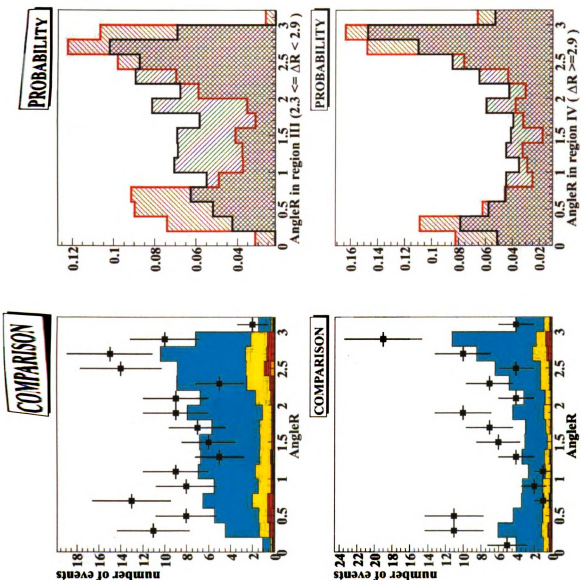


Figure 5.34: The distributions of the angle between reconstructed Z object and the center of mass frame of W/Z (di-jet) and Z (di-lepton) objects for muon channel in the third and fourth regions.

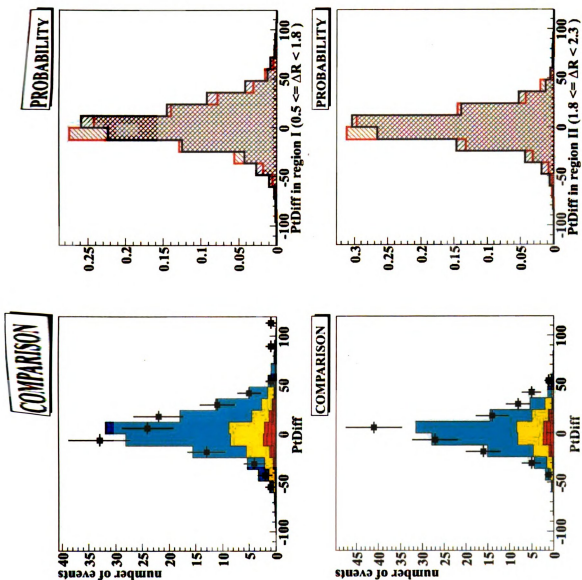


Figure 5.35: The distributions for  $p_T$  difference of W/Z (di-jet) and Z (di-lepton) for electron channel in first and second regions.

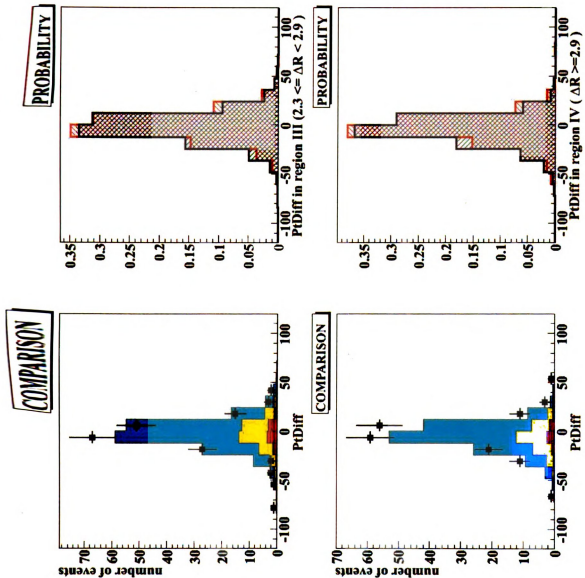


Figure 5.36: The distributions for  $p_T$  difference of W/Z (di-jet) and Z (di-lepton) for electron channel in third and fourth regions.

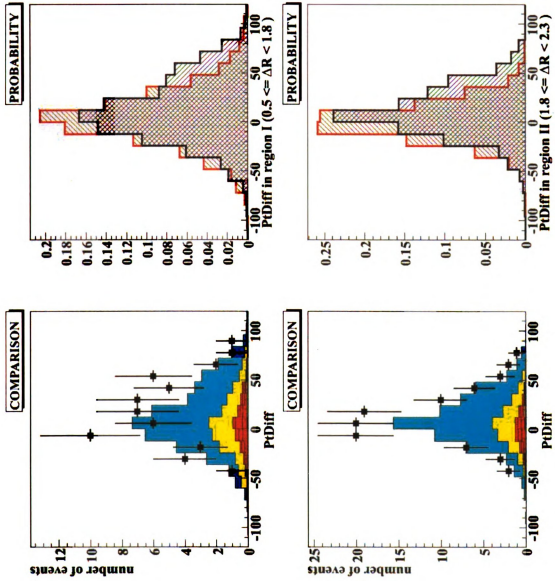


Figure 5.37: The distributions for  $p_T$  difference of W/Z (di-jet) and Z (di-lepton) for muon channel in first and second regions.

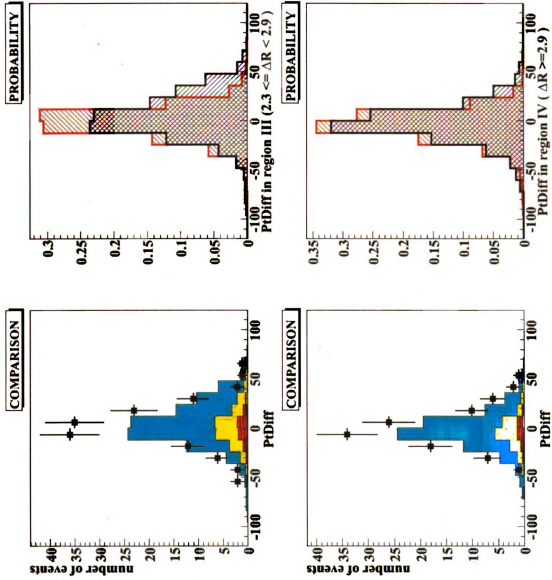


Figure 5.38: The distributions for  $p_T$  difference of W/Z (di-jet) and Z (di-lepton) for muon channel in third and fourth regions.

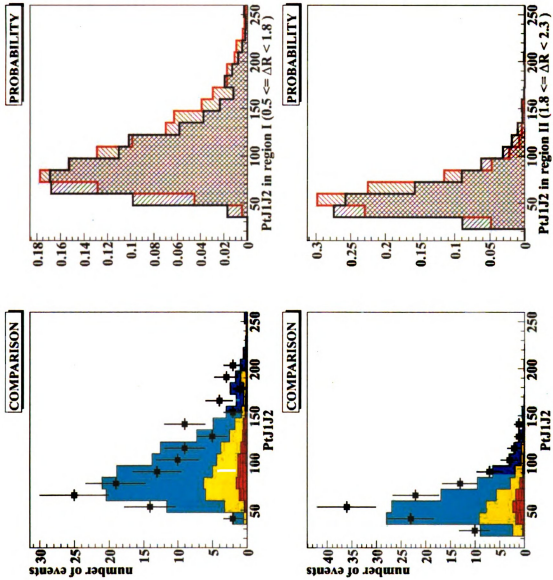


Figure 5.39: The distributions for di-jet  $p_T$  for electron channel in first and second regions of likelihood.

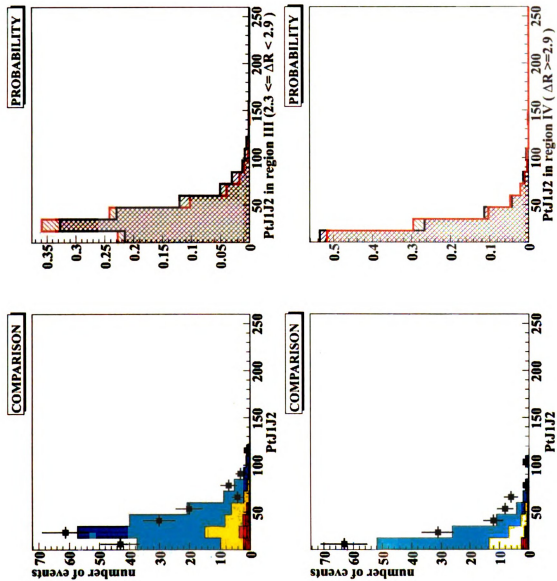


Figure 5.40: The distributions for di-jet  $p_T$  for electron channel in third and fourth regions of likelihood.



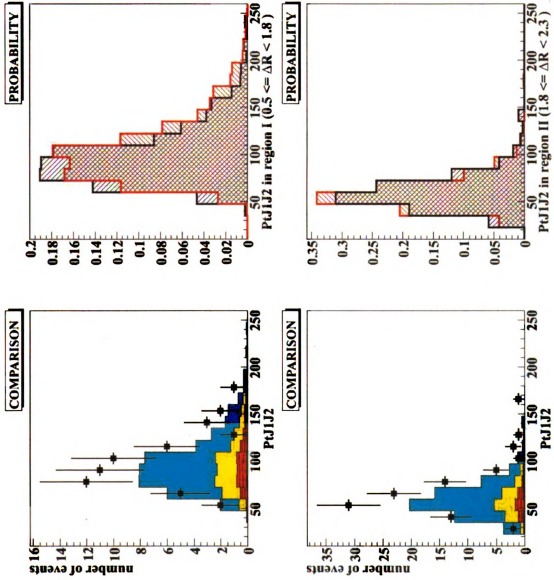


Figure 5.41: The distributions for di-jet  $p_T$  for muon channel in first and second regions of likelihood.

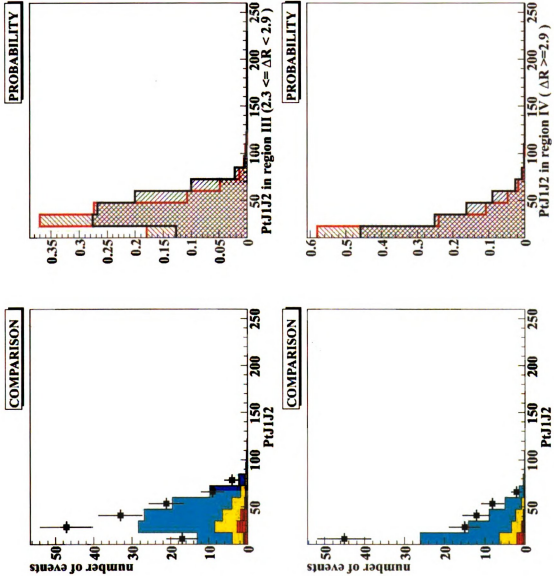


Figure 5.42: The distributions for di-jet  $p_T$  for muon channel in third and fourth regions of likelihood.

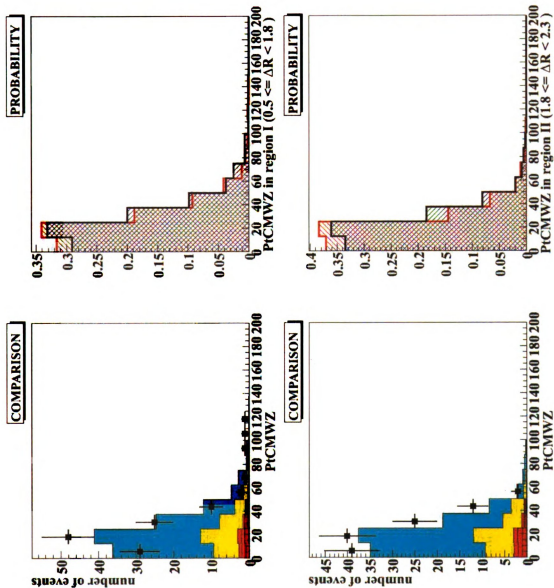


Figure 5.43: The distributions for the  $p_T$  of the center of mass system for di-jet and di-lepton objects for electron channel in first and second regions.

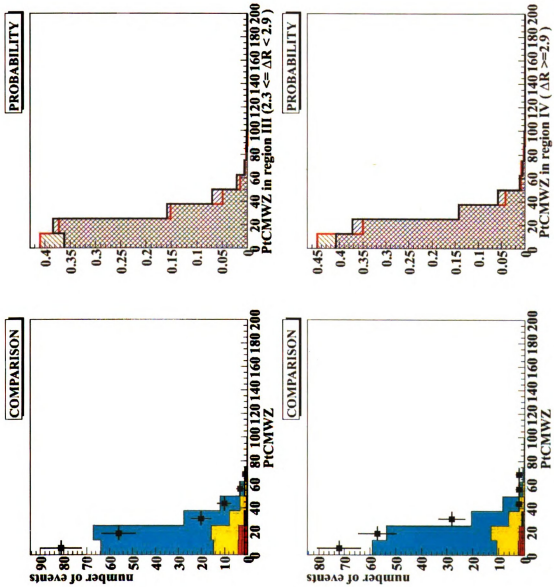


Figure 5.44: The distributions for the  $p_T$  of the center of mass system for di-jet and di-lepton objects for electron channel in third and fourth regions.

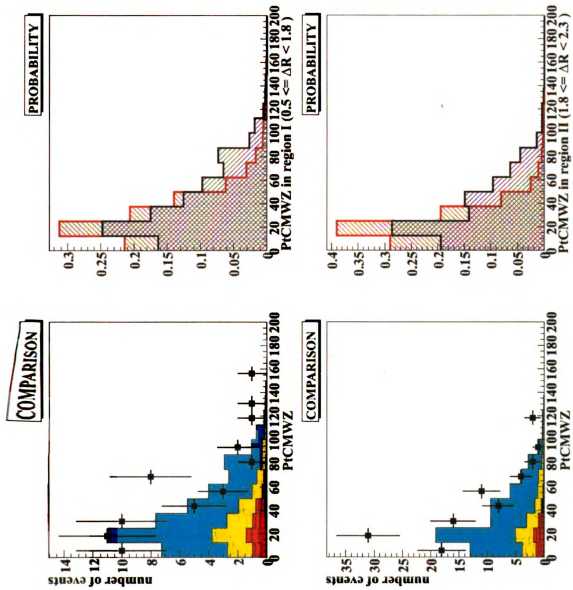


Figure 5.45: The distributions for the  $p_T$  of the center of mass system for di-jet and di-lepton objects for muon channel in first and second regions.

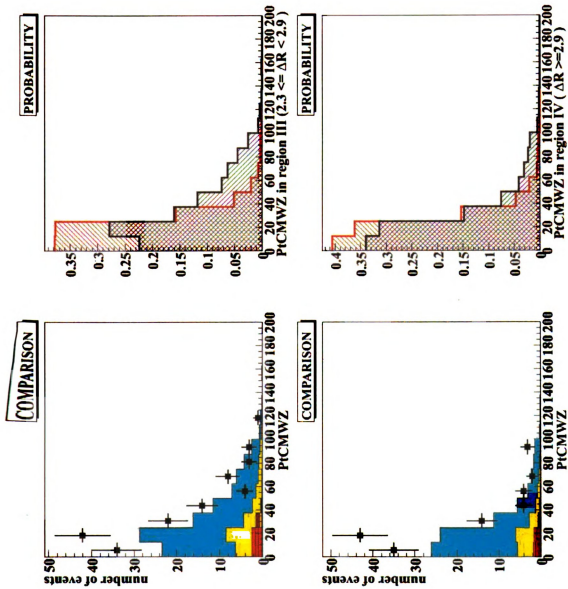
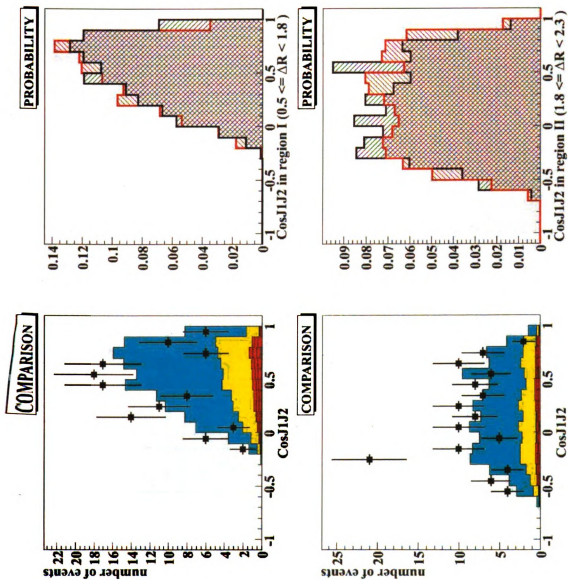


Figure 5.46: The distributions for the  $p_T$  of the center of mass system for di-jet and di-lepton objects for muon channel in third and fourth regions.



**Figure 5.47:** The distributions for the cosine of the angle between highest  $p_T$  jet and second highest  $p_T$  jet for electron channel in first and second regions.

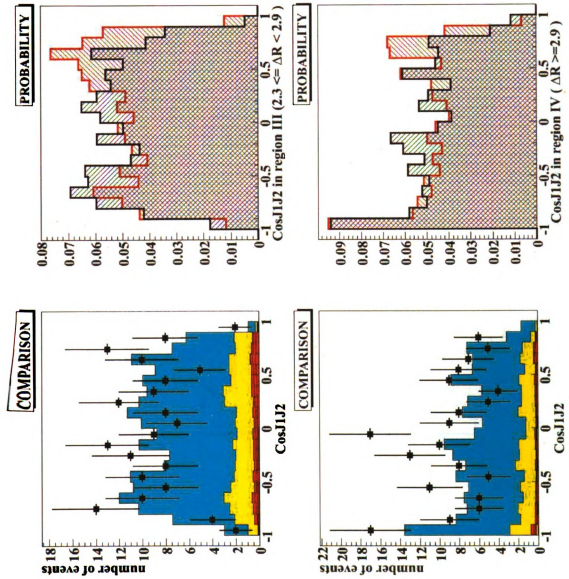


Figure 5.48: The distributions for the cosine of the angle between highest  $p_T$  jet and second highest  $p_T$  jet for electron channel in first and second regions.



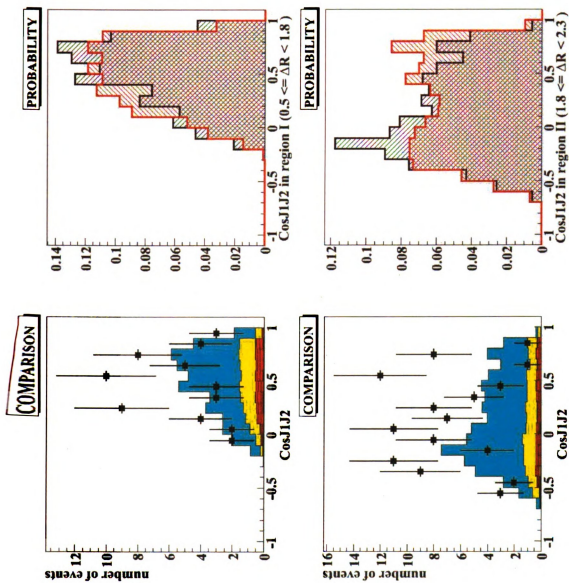


Figure 5.49: The distributions for the cosine of the angle between highest  $p_T$  jet and second highest  $p_T$  jet for muon channel in first and second regions.

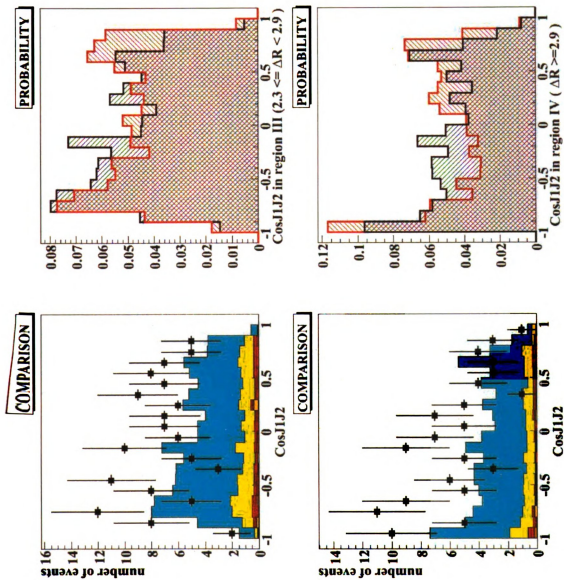


Figure 5.50: The distributions for the cosine of the angle between highest  $p_T$  jet and second highest  $p_T$  jet for muon channel in third and fourth regions.

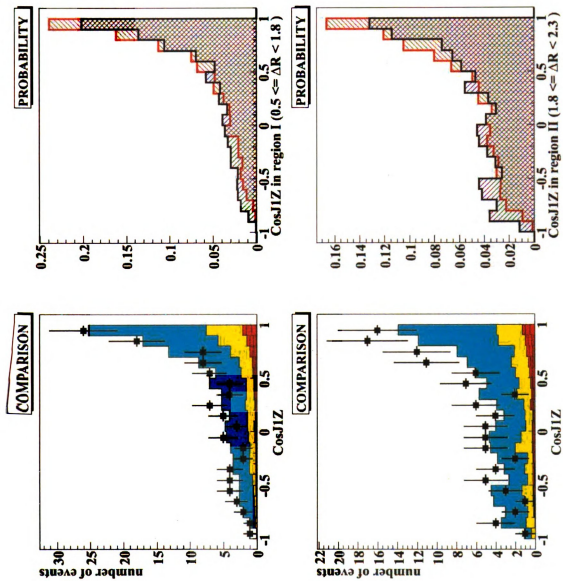


Figure 5.51: The distributions for the cosine of the angle between the highest  $p_T$  jet and the Z (di-lepton) object for electron in first and second regions.

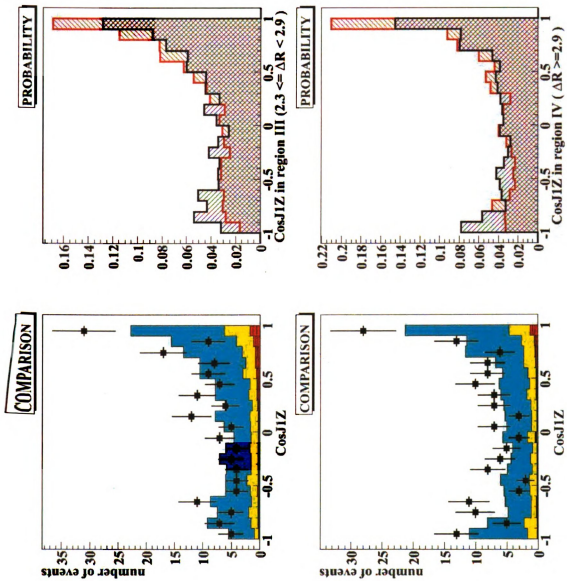


Figure 5.52: The distributions for the cosine of the angle between the highest  $p_T$   $\text{jet}$  and the Z (di-lepton) object for electron in third and fourth regions.

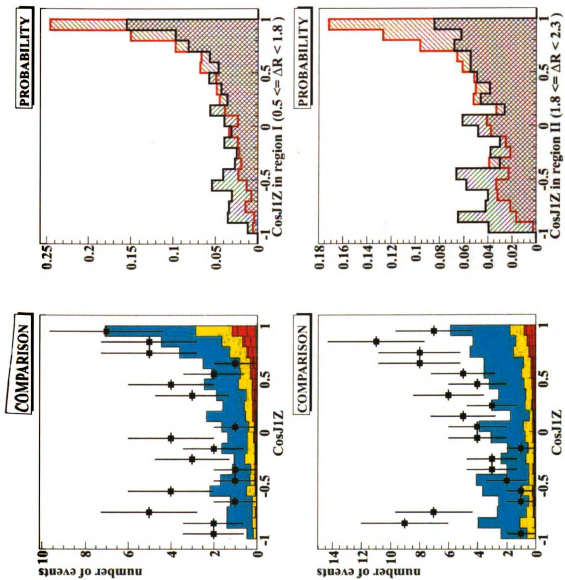


Figure 5.53: The distributions for the cosine of the angle between the highest  $p_T$  jet and the Z (di-lepton) object for muon in first and second regions.

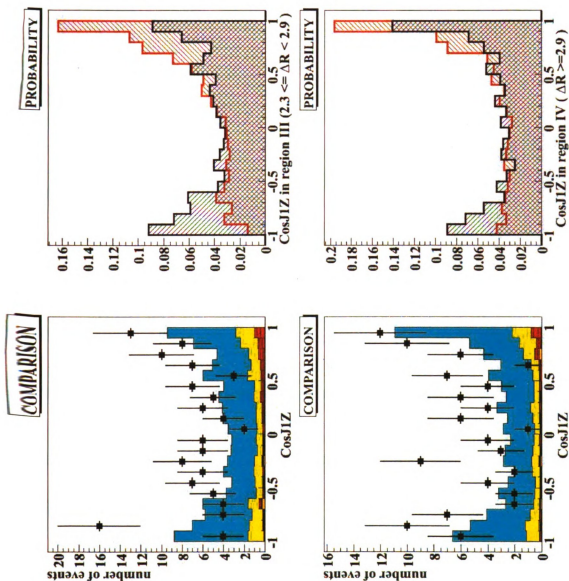


Figure 5.54: The distributions for the cosine of the angle between the highest  $p_T$  jet and the Z (di-lepton) object for muon in third and fourth regions.

# Chapter 6

## Results

**Yağız At**

*“İşaret bekliyorum, yağız atım eğerli;  
Yanarım sorarlarsa ‘ne getirdin değerli?’ ”  
Necip Fazıl Kısakürek<sup>1</sup>*

This chapter mentions the result of the measurement explained in the previous chapter.

### 6.1 Likelihood Results

For the calculation of the cross section measurement we have used a modified likelihood method which enabled us to pick differences between the signal and background events. At this point it is necessary to re-mention the definition of our likelihood:

$$L(x) = \frac{P_{sig}(x)}{P_{sig}(x) + P_{bkg}(x)} \quad (6.1)$$

---

<sup>1</sup>**Swart Stallion**

Waiting for a sign, my swart stallion saddled;  
Damned if they ask ‘what did you bring esteemed?’

where  $P_{sig}$  is the probability for an event to be signal and  $P_{bkg}$  is the probability for an event to be background. The value of the likelihood for a signal event is 1 and 0 for a background event.

By simply dividing the phase space into four regions and using different components for the vector  $\vec{x}$ , we were able to build a likelihood powerful discriminant. The discriminant histograms obtained by above method can be seen in Figures 6.1, 6.2. In these figures the number of events in both signal and background Monte Carlo events are normalized to one so that the discriminant for the background events doesn't overwhelm.

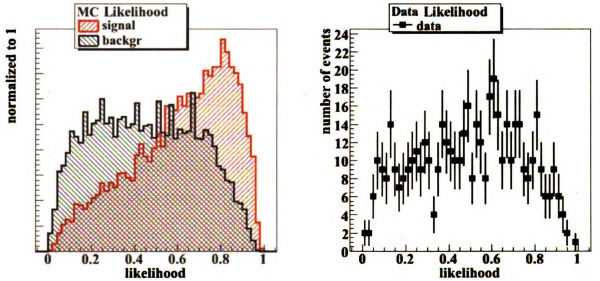


Figure 6.1: The distributions of likelihood discriminant for em channel. The left hand side shows signal and background Monte Carlo events discriminant distribution. These distributions are normalized to 1, so that their shape could be seen easily. The right hand side shows the discriminant for RunIIa events passing all the cuts previously mentioned. Total number of RunIIa data shown in this figure (right hand side) is 475 events.



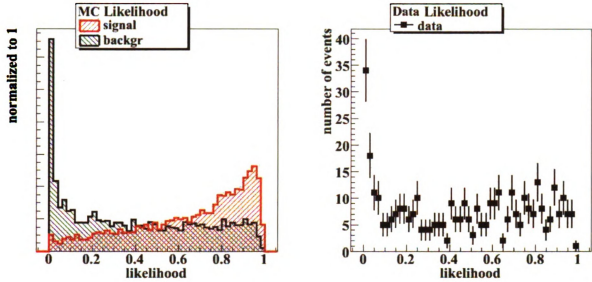


Figure 6.2: The distributions of likelihood discriminant for muon channel. The left hand side shows signal and background Monte Carlo events discriminant distribution. These distributions are normalized to 1, so that their shape could be seen easily. The right hand side shows the discriminant for RunIIa events passing all the cuts previously mentioned. Total number of RunIIa data shown in this figure (left hand side) is 381 events.

The total number of RunIIa data surviving all the cuts mentioned until here; namely object selection cuts for leptons (electron and muon), and jets, dilepton mass, MET, dijet mass, eta-eta and  $pt_{jet1}-pt_{jet2}$  cuts, are 475 events for the electron channel and 381 events for the muon channel.

The calculation of the cross section is done by the following method. To determine the cross section, we need to separate signal and background events in the data. We assume that the data is a linear combination of signal events ( $F$ ) and background events ( $F'$ ). Then the total number of data events and their likelihood distribution is given by

$$D = F \times S + F' \times B \quad (6.2)$$

where  $D$  is the absolute likelihood distribution for data and  $S$  and  $B$  are the normalized likelihood distributions for signal and background. We perform a fit using 6.2 in order to determine signal and background in the data.

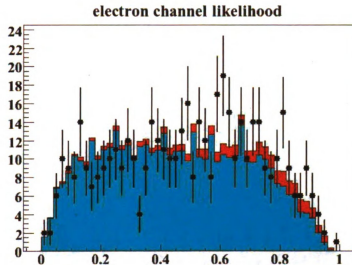


Figure 6.3: Likelihood discriminants and their fits to data for electron channel. The points are for RunIIa data, the fit result is overlayed on them represents data as signal (red) and background (blue) contributions.

Channel	Signal	Background
electron	$39.1 \pm 10.4$	$436.1 \pm 43.1$
muon	$32.7 \pm 8.7$	$346.4 \pm 35.5$

Table 6.1: Number of estimated events in the RunIIa data using the MC discriminant distributions as templates.

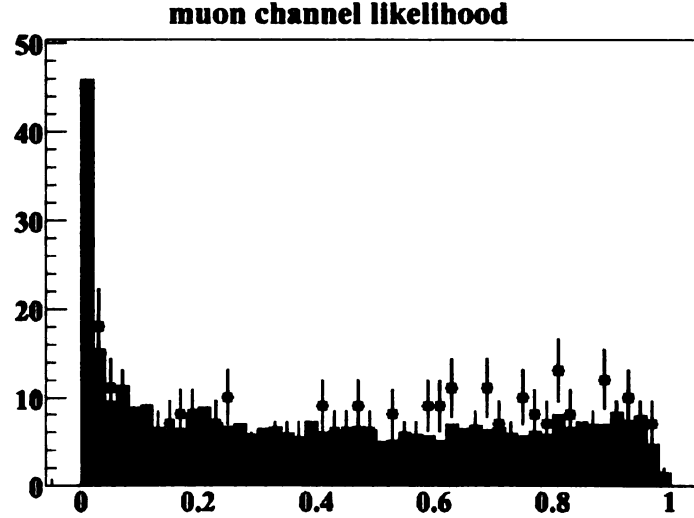


Figure 6.4: Likelihood discriminants and their fits to data for muon channel. The points are for RunIIa data, the fit result is overlaid on them represents data as signal (red) and background (blue) contributions.

To obtain these histograms, the equation 6.2 is solved for  $F$  and  $F'$  by fitting the unit normalized signal and background likelihood distributions to the data plot. By scaling up these distributions by their relative ratios ( $F$ ,  $F'$ ) and overlaying the monte carlo distributions on data we got Figures 6.3 and 6.4. From this we obtain the number of signal and background events as shown in the Table 6.1

For the cross section measurement we used

$$\sigma = \frac{N}{\epsilon \times \mathcal{L}} \quad (6.3)$$

where  $N$  is the number of events seen (or more truly expected from the fit,  $\epsilon$  is the

Channel	RunIIa Luminosity
electron	$1044 \pm 72 \text{ pb}^{-1}$
muon	$948 \pm 66 \text{ pb}^{-1}$

Table 6.2: Table of luminosity values for RunIIa run period.

Channel	Combined Efficiency
electron	$0.014 \pm 0.003$
muon	$0.010 \pm 0.004$

Table 6.3: Table of overall efficiencies for WZ/ZZ event selection.

combination of all of the efficiencies and acceptances (which includes geometric and physics acceptances as well as object identification and reconstruction efficiencies) and  $\mathcal{L}$  is the luminosity. Please refer to the Table 6.2 for luminosity values for RunIIa data taking period. The source of the errors in the measurement of the luminosity come from the uncertainties in the measurement of the total proton-antiproton cross section. The Table 6.3 shows the combined efficiencies for the two processes. In this table what is referred as combined efficiencies includes the following:

- The branching ratio's of the final products ( two charged leptons and two jets). The Monte Carlo generated files include all the decay channels. For WZ / ZZ process to decay to  $eejj$  or  $\mu\mu jj$ , the branching fraction is 2.3%
- The object reconstruction efficiencies
- The inefficiencies related with the structure of the detector like uninstrumented regions of the detector etc

Essentially, the probability of observing an WZ/ZZ event (including all the possible final states) in the DØdetector is given by this efficiency. for

At this point we are ready to calculate cross section of the processes by using the quantities given in the tables above. For the values of the cross sections of the processes please see the Table 6.4.

Process	Channel	Cross Section
$\sigma_{WZ/ZZ}$	em	$2.67 \pm 1.90 \text{ pb}$
$\sigma_{WZ/ZZ}$	mu	$3.45 \pm 3.51 \text{ pb}$

Table 6.4: Table of measured cross sections for electron and muon channels for both WZ and ZZ processes. The measurement uses almost  $1 \text{ fb}^{-1}$  of data collected by DØdetector in both channels.

Luminosity	6.1%
Jet Energy Scale	6.0%
JSSR	4.2%
Jet ID	2.1%
Electron ID	5.9%
Muon ID	4.0%
Triggers	6.3%
Jet $\eta$ and $\Delta R$ r.w.	1.6%
$Z + \text{jets}$ cross section	20%

Table 6.5: Table showing the systematic uncertainties of the different sources.

Before continuing on to the next section we should point out that the errors on the cross sections are calculated by propagating the errors in the cross section formula; namely statistical error on the number of events, error on the efficiency and error on the luminosity. In the electron channel the biggest contribution comes from the error in the number of events from the fit. Whereas in the muon channel the biggest contribution comes from the uncertainty in the total efficiencies.

As is evident from the Table 6.1 the uncertainty in the number of background events is on the order of the number of observed signal events. So there is room for improvement in this analysis in the future.

### 6.1.1 Systematic Errors

This analysis suffers from many sources of uncertainties which are listed in the Table 6.5.

As can be seen from the table the most important uncertainty comes from the  $Z + \text{jets}$  cross section measurement. Uncertainties on triggers and luminosity

measurements follow it.

The luminosity uncertainty is provided by the luminosity group to the whole experiment. It comes from the discrepancies in the measurement of the luminosity by DØ and accelerator division. The uncertainties on the object identifications are provided by the respective object identification group. They reflect systematic and statistical uncertainties on the measurement of object identification measurements. The error on efficiencies used in the cross section measurement includes errors on JES, JSSR, jet-id, lepton-id, trigger and jet-eta errors.  $Z + jets$  uncertainty results from the lack of our knowledge of expressing this process in our monte carlo programs. Except the last of these errors, all of the others are included in the calculation of the uncertainty of cross sections.

For the calculation of these uncertainties, one changes object identification efficiencies by their uncertainties redo the whole analysis and calculates the differences. Instead of following these steps, we used uncertainty numbers from a very similar, having the same object definitions, analysis (WZ/WW cross section measurement).

The trigger group at DØ provided uncertainty on “Super-OR”ed triggers which means that all the single lepton triggers are combined with lepton + jets triggers in order to increase acceptance for the process.

Then for  $WZ/ZZ$  process the total systematic error for the electron channel is 1.29 pb and for the muon channel it is 2.31 pb.

## 6.2 Conclusion

Being a very challenging physics analysis, it was possible to measure the combined cross section of  $WZ/ZZ$  processes.

$$\sigma_{WZ/ZZ} = 2.67 \pm 0.71 \text{ (stat)} \pm 1.29 \text{ (syst)} \text{ pb}$$

, and

$$\sigma_{WZ/ZZ} = 3.45 \pm 0.92 \text{ (stat)} \pm 2.31 \text{ (syst)} \text{ pb}$$

The theoretical values for the WZ and ZZ processes are given below:

$$\sigma_{WZ} = 3.68 \text{ pb}$$

and

$$\sigma_{ZZ} = 1.46 \text{ pb}$$

. Therefore for the WZ/ZZ process the theoretical cross section is 5.14 pb. Although the theoretical values for the cross section lies within the uncertainty of the measurement, it is obvious that we have still many improvements to make.

# Bibliography

- [1] J.D. Salinger, *Catcher In The Rye*, Bantam, 1966
- [2] Bediüzzaman Said Nursî, *Sozler*, Tenvir Nesriyat, 1956
- [3] Joseph J. Thomson, *Carriers of Negative Electricity*, Nobel Lecture, December 11, 1906
- [4] Willis E. Lamb Jr., *Fine Structure of the Hydrogen Atom*, Nobel Lecture, December 12, 1955
- [5] Louis De Broglie, *Wave Nature of Electron*, Nobel Lecture, December 12, 1929
- [6] Martinus Veltman, *Facts and Mysteries in Elementary Particle Physics*, World Scientific Publishing Company, April 2003
- [7] Francis Halzen, Alan D. Martin, *Quarks and Leptons*, Wiley, January 1984
- [8] Michael E. Peskin, Daniel V. Schroeder, *An Introduction to Quantum Field Theory*, Westview Press, October 1995
- [9] Michio Kaku, *Quantum Field Theory*, Oxford University Press, March 1993
- [10] B. R. R. Martin, G. Shaw, *Particle Physics*, John Wiley & Sons Ltd, March 1992
- [11] M. Herrero, *The Standard Model*, arXiv:hep-ph/9812242v1
- [12] E. Eichten, et.al. *Supercollider Physics*, Reviews of Modern Physocs, Vol 56, October 1984
- [13] Private chat with Chris Quigg
- [14] J. M. Campbell, R. K. Ellis, *An Update on Vector Boson Pair Production at Hadron Colliders*, arXiv:hep-ph/9905386
- [15] W. B. Rolnick, *The Fundamental Particles and Their Interactions*, Addison Wesley Publishing Company, January 1994



- [16] Ibn Tufayl, Translated by Lenn Evan Goodman, *Hayy Ibn Yaqzan*, Gee Tee Bee, January 1996
- [17] [http://www.choosechicago.com/see\\_and\\_do.html](http://www.choosechicago.com/see_and_do.html)
- [18] <http://www.fnal.gov/pub/about/whatis/history.html>
- [19] <http://www.fnal.gov/pub/about/whatis/mission.html>
- [20] <http://www.fnal.gov/pub/inquiring/physics/discoveries/index.html>
- [21] Concepts Rookie Book  
[http://www-bdnew.fnal.gov/operations/rookie\\_books/Concepts.v3.5.pdf](http://www-bdnew.fnal.gov/operations/rookie_books/Concepts.v3.5.pdf)
- [22] Main Injector Rookie Book  
[http://www-bdnew.fnal.gov/operations/rookie\\_books/Main\\_Injector.v1.pdf](http://www-bdnew.fnal.gov/operations/rookie_books/Main_Injector.v1.pdf)
- [23] Tevatron Rookie Book  
[http://www-bdnew.fnal.gov/operations/rookie\\_books/Tevatron.v1.pdf](http://www-bdnew.fnal.gov/operations/rookie_books/Tevatron.v1.pdf)
- [24] Recycler Rookie Book  
[http://www-bdnew.fnal.gov/operations/rookie\\_books/Recycler.v1.3.pdf](http://www-bdnew.fnal.gov/operations/rookie_books/Recycler.v1.3.pdf)
- [25] Ed Catmull, *How Pixar Fosters Collective Creativity*, Harvard Business Review September 2008
- [26] Ashish Kumar et.al., *Electron Likelihood Study*, DØ Note 4769
- [27] Philippe Calfayan et.al., *Muon Identification Certification for P17 Data*, DØ Note 5157
- [28] S. Beauceron, G. Bernardi, *Missign  $E_T$  Studies on Zero and Minimum Bias Events*, DØ Note 4119
- [29] A. Schwartzman, M. Narain, *Probabilistic Primary Vertex Selection*, DØ Note 4042
- [30] A. Harel, *Jet-ID Optimiztion*, DØ Note 4919
- [31] J.L. Agram, *Jet Energy Scale at DØ RunII*, DØ Note 4720
- [32] JES GROUP, *JetEnergy Scale Determinationat DØ* , DØ Note 5382
- [33] [http://www-d0.fnal.gov/phys\\_id/jes/public/plots.v7.1/index.html](http://www-d0.fnal.gov/phys_id/jes/public/plots.v7.1/index.html)
- [34] C. Ochando, J-F. Grivaz, *SSR for p17*, DØ note 5609
- [35] N. Makovec, J-F. Grivaz, *Shifting, Smearing and Removing Simulated Jets*, DØ Note 4914
- [36] J. Hays, J. Mitrewski, C. Schwanenberger, T. Toole, *Single Electron Efficiencies in p17 Data and Monte Carlo*, DØ Note 5025

- [37] John Gardner, *Single EM Trigger Efficiency Using a Diem Tag and Probe Method*, DØ Note 4338
- [38] Bernard Andrieu et.al, *Measuring Reconstruction\*Jet-ID efficiencies using the tag and probe method in p17*, DØ Note 5250
- [39] Bernard Andrieu et.al, *Jet-ID Certification for RunIIa Data in p17*, DØ Note 5170
- [40] <http://www.dictionary.com>
- [41] Sir Arthur Conan Doyle, *The Adventures of Sherlock Holmes, The Speckled Band*, Books of Wonder William Morrow & Company, Inc
- [42] William Shakespear, *Measure For Measure*, Complete Works, CC Publishing
- [43] The DØ Collaboration, *Top Quark Mass Measurement with the Matrix Element Method in the Lepton+Jets Final State at DØ Run II*, DØ Note 5053
- [44] K. Kröninger, A. Magerkurth, A. Quadt, P. Scheferdecker, *Top Mass Measurement in the Lepton+Jets Channel using the Matrix-Element Method in Run-II*, DØ Note 4427
- [45] [http://www.stat.berkeley.edu/~breiman/RandomForests/cc\\_home.htm](http://www.stat.berkeley.edu/~breiman/RandomForests/cc_home.htm)
- [46] L. Breiman, *Random Forests*, Machine Learning, 2001 , SpringerLink
- [47] I. Narsky, *StatPatternRecognition: A C++ Package for Statistical Analysis of High Energy Physics Data*,